

HENRYK NIEWODNICZAŃSKI INSTITUTE OF NUCLEAR PHYSICS POLISH ACADEMY OF SCIENCES

Simulations and Measurements of the Galactic Dark Matter Halo with the WArP Detector

PhD Dissertation

Author: Andrzej M. SZELC Supervisor: prof. dr hab. Agnieszka ZALEWSKA

Kraków, April 2009



Contents

1	Intr	roduct	ion	5
2	Dar	k Mat	ter as a Part of the Standard Cosmological Model	9
	2.1	The S	Standard Cosmological Model	10
		2.1.1	Dark Energy	14
		2.1.2	Dark Matter	16
	2.2	Evide	ence for Dark Matter	17
		2.2.1	First astronomical observations	18
		2.2.2	Cold Dark Matter	18
		2.2.3	WIMPs as Dark Matter	20
		2.2.4	Numerical simulations	21
		2.2.5	Weak lensing	23
		2.2.6	The Bullet Cluster	24
	2.3	Alter	native explanations to the Dark Matter phenomena	25
		2.3.1	Standard Cosmological Model vs galaxies	26
		2.3.2	Alternative theories of gravity	27
3	Sea	rches i	for Dark Matter Particles	29
	3.1	What	is Dark Matter - a review of the hypotheses	29
	3.2	What	the collider experiments can tell us	32
	3.3	Indire	ect searches	34
		3.3.1	EGRET	34
		3.3.2	PAMELA	35
	3.4	Direc	et detection experiments	36
		3.4.1	DAMA	39
		3.4.2	Cryogenic crystal detectors	40
		3.4.3	Cryogenic noble liquid detectors	42
	3.5	Summ	nary of the current experimental situation	44

4	The	WAr	P Experiment	47		
	4.1	Liquid	l argon as a medium for Dark Matter detection.	. 47		
	4.2	The WArP detector				
	4.3	The 2.3 liter prototype detector				
	4.4	Electr	onics in the WArP experiment	. 54		
	4.5		etection method			
		4.5.1	The electron background suppression	. 57		
		4.5.2	3-D event localization	. 57		
		4.5.3	Neutron background suppression	. 58		
	4.6	Datas	ets used in the analysis	. 61		
		4.6.1	Dark Matter searches datasets			
		4.6.2	Other datasets	. 63		
5	Rese	earch :	and Development in the WArP Experiment	65		
•	5.1		electron response calibration			
	0.1	5.1.1	The Single Electron Response (SER)			
		5.1.2	The 2.3 liter prototype ongoing calibration			
		5.1.3				
	5.2		ffect of nitrogen and oxygen contamination on the light yield	. 00		
	J.2		id argon	. 71		
		5.2.1	The light quenching effect			
		5.2.2	The $ au_{long}$ quenching effect			
	5.3		shape discrimination methods			
	0.0	5.3.1	The third Gaussian population			
		5.3.2	The pulse shape discrimination with the dedicated neutron			
			dataset	. 91		
	5.4	Prelim	ninary neutron quenching measurement			
		5.4.1	Lindhard model and Birks's saturation law			
6	Ana	lvsis c	of the Data Collected with the 2.3 liter Detector	103		
Ü		•	P limits obtained with the WArP 2.3 l chamber result			
	0.1		The chamber setup			
		6.1.2	Data analysis using the SCANWARP software package			
		6.1.3	The published results			
		6.1.4	Results from the subsequent wimp_003 and wimp_004 data	. 100		
		0.2.2	runs	. 109		
	6.2	The i	NEWSCAN software package.			
		6.2.1	Reanalysis of the WArP data using NEWSCAN			
	6.3		ground studies			
		6.3.1	The Baffo region			
			Double neutron events			

7	Anr	nual Modulation Effects Observable in an Argon Detector	127
	7.1	Dark Matter Detection	. 128
		7.1.1 Cross-section	. 129
	7.2	Annual modulation used to determine the WIMP mass	. 129
		7.2.1 The influence of the Sagittarius Stream on the annual mod-	
		ulation expected in an argon detector	. 133
	7.3	Mirror Matter	. 138
8	Con	nclusions	143
A	Glo	ssary	145
В	Erra	ata	147

Chapter 1

Introduction

Dark Matter is one of the greatest puzzles baffling astrophysicists today. It is believed to be responsible for about a fifth of the mass-energy of the Universe, and yet we have never detected even a single direct signature of this substance. A multitude of hypotheses exist, as to what is the nature of Dark Matter. It most probably exists in the form of some unknown, weakly interacting particle. Discovering such a particle, would not only lead to a breakthrough in astrophysics and cosmology, but also in particle physics, since it would surely require an expansion of the Standard Model of particle physics. Because of this, the race to discover the elusive Dark Matter particle is a very close and fascinating one. This PhD thesis is a summary of my work done in the course of developing and operating one of the experiments trying to directly detect Dark Matter - the WArP experiment.

Astrophysics experiments tend to have a much smaller number of participants than particle physics collaborations, especially in the LHC era. One may argue whether this is a good or bad thing, but I personally believe that the small size of the collaboration and of the experiment itself leads to a much better overall understanding of the detector by each of the physicists involved. However, the small number of people requires using the same manpower wherever possible, which in turn forces one to work in a broad range of fields. It is largely because of this, that this thesis is a summary of different tasks which I happened to undertake during the course of my work in the WArP collaboration. This work mainly revolved around the 2.3 liter WArP prototype, but it also was a significant contribution to the preparation of the main, 100 liter, WArP detector, which is now in the final phase of its commissioning in the Gran Sasso laboratory. I personally believe, that this has helped me develop a wider range of skills and gave me a more thorough understanding of the challenges associated with Dark Matter detection.

The fact that the thesis includes so many different aspects of the Dark Matter search makes it difficult to describe everything in sufficient detail. Therefore, for the sake of brevity, some parts of this thesis do not describe the experimental background as profoundly as I would like. Keeping that in mind, the thesis is organized as follows. In the second chapter the evidence for the existence of Dark Matter is described as well as some alternative explanations to the phenomena normally ascribed to Dark Matter. Chapter 3 recounts the current experimental effort geared towards the detection of Dark Matter be it directly, indirectly or via collider experiments. A description of the WArP Dark Matter detector follows in Chapter 4. The last three chapters describe the experimental and theoretical work done in the framework of this thesis. Chapter 5 reports on some of the research and development activity undertaken in the course of preparing the 100 l detector. Chapter 6 describes the results of using a 2.3 liter prototype detector in an actual Dark Matter search run. Finally Chapter 7 is a study of some effects of the galactic Dark Matter halo that might be observed in the 100 liter WArP detector. An Appendix follows, where the acronyms used in this thesis are collected and explained.

As said before, it is impossible to present the specific work done by the author, without the broader context of the actual measurements done by the collaboration. For this reason I have chosen to describe measurements performed as a whole, specifically mentioning if and where a task was actually done by me, keeping in mind that the description of the experimental setup gives sometimes only a rough idea. For easier reference, these tasks will be first mentioned here. In Chapter 5 my specific input involves creating and maintaining a software package and a database used for the ongoing calibration of photomultipliers in the 2.3 liter WArP prototype. This code was later modified and used for tests of photomultipliers for the WArP 100 liter detector. For these tests, a series of graphical user interfaces were written, the first one in collaboration with B. Rossi, all the subsequent ones just by me. In the tests of the effect of contamination with nitrogen and oxygen on the light yield of liquid argon, my work revolved around creating a preanalysis code that read in the rawdata and performed a simple first order analysis. I also devised and performed a parallel analysis using the data from the WArP 2.3 liter detector to test the effect of oxygen at different contamination levels. I also created an alternative to the standard analysis method for the measurement of the quenching of light due to contaminations and created a simulation of the single photon counting technique to allow the comparison of our results with other experiments. I have performed a study on the pulse shape discrimination methods using the data from a dedicated chamber irradiated with an Am-Be neutron source, as described in Chapter 5. I also prepared the whole electronic and data acquisition setup for a preliminary measurement of the neutron quenching effect.

Chapter 6 describes the software used to analyze the data from the WArP 2.3 liter chamber as a Dark Matter detector. I have been responsible for maintaining and upgrading the main analysis code used in the collaboration. I also rewrote this

code in an object oriented manner to facilitate its further usage and upgraded some of the algorithms used. This new version of the code has been used to reanalyze the already published data. I have been a part of the studies of the background in the 2.3 liter chamber - the analysis of the so called "baffo" region and of double neutron events is recounted. I have also participated in estimating the radioactive background of the new 2.3 liter chamber and wrote a graphical monitor for the data acquisition of the detector, but these are not described in this thesis.

Chapter 7 recounts a study that I made on the effects of some parameters of the Galactic Dark Matter halo on the potential annual modulation observable in the 100 l WArP detector, as well as the prospects of detecting Mirror Dark Matter in an argon detector.

I have also spent hundreds of hours in the underground laboratory in Gran Sasso on data taking shifts and during the assembly or modifications of the WArP 2.3 liter chamber. This time has provided me with invaluable experimental experience.

Chapter 2

Dark Matter as a Part of the Standard Cosmological Model

In the last twenty years or so, our view of the Universe has changed dramatically. Before, we had a model of the evolution of the Cosmos, but it was practically an unproven hypothesis. Since then, extreme progress in experimental cosmology and astrophysics has been made. Not only did it confirm the main points of the cosmological models. What is even more amazing is that the current experiments allow us to measure cosmological parameters with an accuracy of the order of 1 percent. This might lead to a conclusion that all has been explained and measured and there is nothing more to look for. Fortunately this is not the case. In glaring opposition to the precise measurements of the cosmological parameters is the fact, that we still do not know what ninety-five percent of the Universe is made of. We have hypotheses about what it is that fills the gap, we can measure a great deal of the properties of these objects or substances indirectly, but Dark Matter and Dark Energy still evade our instruments remaining the most massive (in mass-energy), if not the most intriguing riddle of contemporary physics.

To describe this riddle, one must go back to the Standard Cosmological Model and its description of our Universe, because it is through this description that we can see the amazing consequences of today's astrophysical and cosmological measurements. A brief review of the experimental evidence that leads us to believe in the existence of Dark Matter will follow, as well as a look into alternative models that try to explain the results of cosmological observations without using Dark Matter.

2.1 The Standard Cosmological Model

The Universe described by the Standard Cosmological Model is an ever expanding entity, that started with a state of infinitely hot and infinitely dense matter. This explosion has been named the Big Bang, and is one of the most famous concepts of science. The Universe in the Standard Cosmological Model is governed by the laws of General Relativity, as described by Alfred Einstein in 1915. A detailed decryption of this model can be found in most cosmological textbooks, i.e. [1], [2]. Here a short summary will be presented. Practically, the most commonly used description of the Big-Bang is the Friedman-Lemaitre-Robertson-Walker (FLRW) model. This description assumes spherical symmetry and homogeneity in spacetime, and to obtain the proper equations describing the evolution of the Universe one must solve the Einstein equation:

$$R_{\mu\nu} - \frac{1}{2}g_{\mu\nu}R = 8\pi G_N T_{\mu\nu} + g_{\mu\nu}\Lambda. \tag{2.1}$$

In this tensor equation the indices $\mu\nu$ run from 0 to 3, $R_{\mu\nu}$ and R are the Ricci tensor and scalar respectively, objects derived from the Riemann tensor which describes the curvature of space-time. $g_{\mu\nu}$ is the space-time metric, G_N is Newton's gravitational constant, $T_{\mu\nu}$ is the energy-momentum tensor, which describes the distribution of energy in the Universe, and Λ is a numerical constant, that will be explained further on. In the equation and later on in this chapter a convention is used where the speed of light c=1. The solution of this equation is often obtained by making the einsatz for the metric, in the form of a Robertson-Walker metric for an empty Universe, and then adding matter (for a sample derivation see [1]). As a result, one ends up with the Friedmann equations:

$$\left(\frac{\dot{a}}{a}\right)^2 + \frac{k}{a^2} = \frac{8\pi G_N}{3}\rho_{tot},\tag{2.2}$$

$$2\frac{\ddot{a}}{a} + \left(\frac{\dot{a}}{a}\right)^2 + \frac{k}{a^2} = -8\pi G_N p_{tot},\tag{2.3}$$

$$\partial_t \rho_{tot} = -3 \frac{\dot{a}}{a} (p_{tot} + \rho_{tot}). \tag{2.4}$$

The first two equations are the 00 and 11 components of the Einstein equation, while the third one is actually its geometrical property (called the Bianchi identity) and plays the role of the continuity equation. In these equations a(t) is the scale factor, a quantity that describes the evolution of the size of space. k is the curvature factor and can be equal to -1,0,1 for a Universe that is open, flat or closed, respectively. ρ_{tot} and p_{tot} are the total energy density and the total pressure in the Universe. The components, that are commonly considered are matter,

radiation (i.e. energy density of photons) and the cosmological constant Λ . They are summed up in the following fashion:

$$\rho_{tot} = \rho_m + \rho_{rad} + \rho_{\Lambda}, \tag{2.5}$$

$$p_{tot} = p_m + p_{rad} + p_{\Lambda}, \tag{2.6}$$

noting that $\rho_{\Lambda} = \frac{\Lambda}{8\pi G_N}$ and $p_{\Lambda} = -\frac{\Lambda}{8\pi G_N}$. It is interesting to explore the consequences of Equation (2.2) which, if we substitute $\frac{a}{a} = H$ (H is the Hubble constant), becomes:

$$1 + \frac{k}{a^2 H^2} = \frac{\rho_{tot}}{\frac{3H^2}{8\pi G_N}} = \frac{\rho_{tot}}{\rho_{crit}},\tag{2.7}$$

where we have defined the critical density $\rho_{crit} = \frac{3H^2}{8\pi G_N}$. This is a very important quantity, because, as it turns out, it determines the geometry of the Universe. If we define the ratio of mass-energy density present in the Universe to the critical density as $\Omega = \frac{\rho_{tot}}{\rho_{crit}}$ and insert it into Eq. (2.7) we obtain

$$\frac{k}{a^2H^2} = \Omega - 1. \tag{2.8}$$

It can be seen that the curvature factor k is zero if the amount of mass-energy of all the components is equal to the critical density. If the sum of the mass and energy components is less than ρ_{crit} , then k < 0 and the geometry is hyperbolic and if more, then k > 0 and the geometry is closed. If the cosmological constant was nonexistent, i.e. $\rho_{\Lambda} = 0$ then the value of Ω would also determine the fate of the Universe, but since this is not the case, as will be shown later, we will not discuss this here.

The most preferred option from the aesthetical point of view is if $\rho_{tot} = \rho_{crit}$, which would result in a Universe with a flat geometry. There are other arguments that lead us to this conclusion. An example is the flatness-oldness problem, which basically claims that with the evolution of the Universe the value of Ω_{tot} would quickly diverge from the boundary value of one if it was not exactly equal to one to begin with. But to measure the non-zero Ω_{tot} that we see now, even at the level of 0.3, the total density at the beginning of the evolution of the Universe would have to be equal to one with a precision of the level of 10^{-59} at the so called Planck Time - 10^{-44} s after the Big Bang [3], which would be a remarkable fine tuning of the parameters. Arguments such as this were repeated many times, but could not be taken as sound evidence and so the question of the geometry of the Universe remained an open one. This has recently changed, thanks to the new precision experiments. Today, a large part of the riddles, that were thought to be unsolvable can be measured and quantified. There are, however, new riddles that still pose a challenge to experimental astrophysics.

In order to understand the details of the cosmological measurements it is a good idea to shortly review how the Big-Bang model sees the evolution of the Universe. In sum, what the mathematical model predicts is an ever expanding Universe, that started 13.7 billion years ago in an infinitely hot and dense fireball. Our current theories do not allow us to predict what happened before Planck Time - 10^{-44} s, as this is where a quantum theory of gravity is needed and so far none exists. After this time however, we can say quite a lot. Whether or not an inflationary phase followed by reheating occurred, the Universe continued to expand and was filled with a hot plasma, where all particles were in thermal equilibrium with the electromagnetic radiation which in turn was the dominant energy component. This is known as the radiation-domination era and it lasted to about $t \sim 10^4$ years. Due to the expansion two processes occurred - first, the temperature kept on dropping, so for a given particle at a certain time the photons no longer had the energy needed to create new particle-antiparticle pairs, second, the density of radiation and matter dropped and so the particles could not annihilate efficiently due to their lower density and their abundances became frozen out. We can estimate the times that this happened for all known particles and so, for nucleons this is around 10^{-4} s after the Big Bang, for light nuclei like deuterium, helium, and lithium it is about three minutes. Another important moment in the evolution of the Universe is the so called Recombination, when the energy of photons became so small, that they could not dissolve the hydrogen atoms forming from free protons and electrons found in the plasma. It is at this point that the Universe became transparent to electromagnetic radiation. Starting at this time, the baryons, no longer disrupted by the energetic electromagnetic radiation, could begin to form structures by collapsing into gravitational potential wells. These structures are what should then evolve into the stars and galaxies we see today.

In 2003, the first data release from the WMAP satellite made it possible to precisely measure the position of the first peak of the Cosmic Microwave Background power spectrum. The CMB is what remains of the photons that escaped from the hot plasma at the time of Recombination so, in a way, by measuring it we are taking a cooled down snapshot of the Universe as it was 376000 years [4] after the Big Bang. The CMB spectrum is calculated by plotting the map of the Cosmic Microwave Background seen in Fig. 2.1 a and expanding it into spherical harmonical functions. The coefficients of this expansion are plotted as the power spectrum in Fig. 2.1 (b) [6]. The position of the first peak is important because it gives us the insight into the preferred length of the path that sound waves traveled at the time of Recombination. It can be calculated that for a flat Universe this distance should be visible with a size of about 1° radial [6]. This

corresponds to the multipole coefficient l of about 200, and this is exactly where it has been measured by the WMAP probe and earlier, though less precise, CMB experiments, proving that we do, in fact, live in a flat Universe. From this information, using the correlation between curvature and the mass-energy density described before, it was possible to determine the amount of mass-energy in the Universe as $\Omega_{tot} = 1.0052 \pm 0.0064$ [4], which means that $\rho_{tot} = \rho_{crit}$.

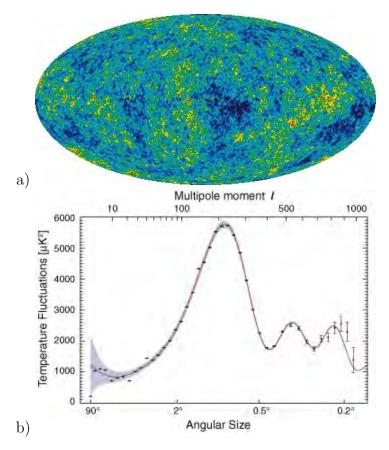


Figure 2.1: a) The map of the Cosmic Microwave Background Radiation as observed by the WMAP satellite. The colors represent relative changes in the temperature with respect to the measured 2.7K of the CMB black body spectrum $\frac{\Delta T}{T}$. Red spots indicate warmer regions, while the blue one indicate colder regions. b) The power spectrum obtained from the map plotted against the multipole moment and the corresponding angular size of the fluctuation observed in the sky [5].

Knowing how much mass-energy exists in the Cosmos, it is quite natural to assume that it is made of matter that is known to us, and not to invent exotic entities just for the sake of it. Unfortunately using this simplest approach is not possible in this case. Already when trying to quantify the amount of visible matter,

i.e. stars and galaxies it has been realized many years before the measurements of WMAP, that they cannot be responsible for more than $0.5\%\rho_{crit}$. The natural explanation is that not all matter has condensed into stars - it did not have the possibility to partake in thermonuclear fusion, or other highly energetic events or objects that emit light in the sky. It is simply dark, and so we cannot see it. However, if we assume that it is baryonic matter, which is the natural thing to do, then even though we cannot see it, we can still put a limit on its amount in the Universe.

Our knowledge of this quantity comes from the model of nucleosynthesis [7, 8], which describes how the light nuclei formed in the first minutes after the Big Bang. At this time, the protons and neutrons detach themselves from the expansion, as described before. When they do, they can begin forming simple light nuclei like ${}^{2}D$, ${}^{3}T$, ${}^{3}He$, ${}^{4}He$, ${}^{6}Li$, ${}^{7}Li$. These nuclear processes are well known, due to our knowledge of nuclear physics, as well as our understanding of solar physics. The important thing is that most of these light elements are still observed today. Their relative abundance is dependent only on the ratio of the density of γ radiation and that of baryonic matter. Since the photons are still visible today as CMB radiation, by measuring the abundances of Deuterium, Lithium and Helium-3 we can infer the amount of baryonic matter in the Universe. The most recent result is, that baryonic matter is responsible for no more than 4.3% of the ρ_{crit} [8]. Where, then, is the remaining 96 percent hidden? Since we cannot attribute it to astronomical objects or baryonic gas, we must take the route of more exotic explanations.

2.1.1 Dark Energy

The Friedmann equations are paramount to understanding the Cosmological Model. In fact, when solving them, Friedmann predicted that the Universe would be expanding. Einstein himself had foreseen this and to be in accordance with the view accepted by all at the time, that the Universe was static, introduced a cosmological constant Λ to make it so. Hubble's subsequent discovery, that practically all the galaxies are moving away from the Milky Way, caused Einstein to utter the well known phrase about the cosmological constant being the greatest mistake of his life. It seems, however, that Einstein had the right intuition and an insight, that he had denied himself. The current Cosmological Model has an implicit part, called Dark Energy, that acts like a cosmological constant, that is responsible for 0.721 ± 0.0015 of the mass-energy of the Universe [4].

The evidence for the cosmological constant comes primarily from the observations of the Supernovae type Ia. These rare cosmic, cataclysmic events act as normal Supernovae, except that a correlation has been found between their brightness curve and total luminosity [9]. The brightness curve is how the light seen from the Supernova changes with time, and for all SN Ia they can be normalized us-

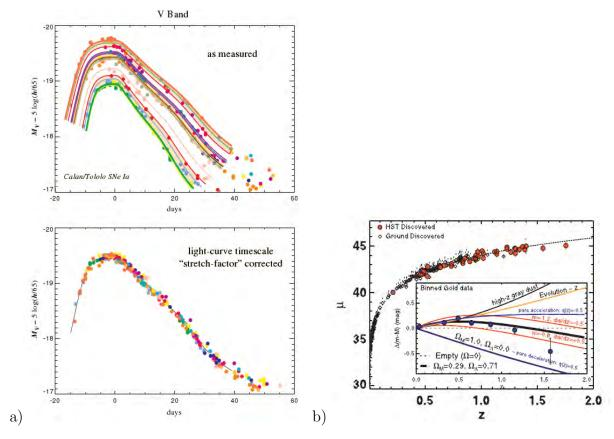


Figure 2.2: a) The brightness curves for a sample of SN Ia, as well as the total curve normalized using the stretch factor [10]. b) The change in acceleration of the Universe observed thanks to the collected observations of the Hubble Space Telescope and the ground observations [12].

ing a "stretch" factor and after this operation their total luminosity is practically identical as in Fig.2.2 a. This means that they can be treated as standard candles - objects with a known, standard brightness that is the same for all objects of a given class. This feature allows us to reliably estimate their distance from the Earth. Since these objects, due to gravitational collapse, in a matter of seconds emit energy of the order of 10^{51} ergs, which is billions of times brighter than the Sun, they allow us to determine the distance to galaxies that are a lot further than any others measured using less luminous standard candles. This also means that we can probe further back in time.

The observations of these Supernovae were actually performed to measure how much the expansion of the Universe decelerates due to the gravitational pull of the mass-energy of matter and radiation. The surprising result of these measurements, published barely a decade ago [11], was that it did not decelerate at all. Quite the opposite. The observations favoured the option in which the expansion of the Universe was actually accelerating, see Fig. 2.2 b. The only way to make this work in the Friedmann/Einstein equations was to reintroduce the cosmological constant, a force that seems to blow up space-time. It is not clear, whether this cosmological constant changes with time, or what is its nature, but it is becoming possible to probe at least some of its properties. Most measurements, like those of the CMB seem to favour a non-changing cosmological constant, that is 72.1% of the mass-energy of the Universe [4].

2.1.2 Dark Matter

Since Dark Energy and baryonic matter can be responsible for only as much as 72.1% + 4.3% = 76.4% of the critical density, and we know that the total amount of mass-energy is equal to that quantity, then an ingredient of the cosmic recipe is still missing. This last ingredient was actually suspected to exist already a long time before the cosmological constant re-entered the scene and it is that of Dark Matter. This substance is something that interacts gravitationally, and generally behaves like matter, but is not baryonic and is hard to detect since we have not seen it yet. This entity counts for 23.6% of the critical density. So one can say, that it poses a riddle that is of the order of a fifth part of the Cosmos.

It is important to realize that the current Cosmological Model is called the concordance model, because it is a result of the observations of several independent cosmological experiments. For example, the most stringent cosmological parameter values come from combining the results of WMAP together with the Supernova Ia results and several other experiments of which the Large Scale Sky Surveys play one of the larger roles. The Sky Surveys will be mentioned again in this work, so it is sensible to describe them here.

The largest Sky Surveys, whose data is frequently used when determining cosmological parameters, are the 2dF Galaxy Redshift Survey (2dFGRS)[14] and the Sloan Digital Sky Survey (SDSS)[15]. Both experiments observed the sky and tried to catalogue all luminous objects, whether they be galaxies or quasars. All objects were analyzed with a spectrograph, so one of the goals was to provide a database of spectra of luminous objects. Their arguably larger achievement in cosmology came from the fact, that having the spectra of these objects it was possible to determine their redshift and so construct a three dimensional map of the placement of matter in the surrounding Universe up to cosmological redshifts z^1 of 0.5. These maps allow the calculation of the so called matter power spec-

¹Cosmological redshift z is defined as $z(t) = \frac{a(t_o)}{a(t)} - 1$, where a is the scale factor of the Universe at present time t_o and at the time of emission of the observed light t.

trum P(k) seen in Fig. 2.3, which describes the difference between the local and mean densities of matter as a function of the scale factor k. The power spectrum is a prediction of the Cosmological Model and the Large Scale Surveys can and have tested it for large values of k up to the order of 0.3 Mpc⁻¹, unreachable for previous experiments. The agreement of the measured spectrum with the values predicted by the model of how structure should have formed in the framework of the Cosmological Model added strong support to whole model.

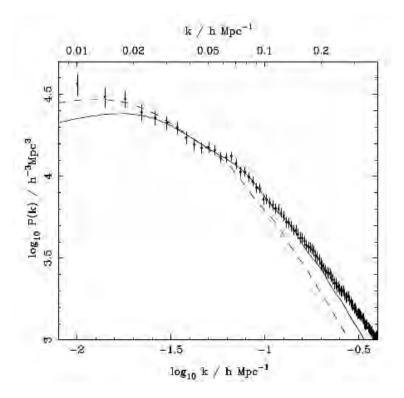


Figure 2.3: The matter power spectrum measured by the SDSS survey. Larger values of the scale factor, k, may be probed by Lyman- α forest observations, while the smaller values by the CMB observations. The lines are two fits of the Cosmological Model [16].

2.2 Evidence for Dark Matter

As has been mentioned in the previous section, Dark Matter is a concept that is older than Dark Energy. There is numerous evidence suggesting its existence, and the idea is definitely less exotic than that of something with negative pressure like the cosmological constant.

2.2.1 First astronomical observations

The first mention of extra, invisible mass comes from the 1930's when F. Zwicky was observing the Coma Cluster. The velocity dispersion of the galaxies obtained using the redshift of their spectra together with the virial theorem allowed the Swiss astronomer to determine the mass of the cluster [17]. It turned out to be ten times more than what was expected observing only the luminous matter. Similar results were obtained by Smith for the Virgo cluster in 1936 [18] and from observations of M31, also known as the Andromeda galaxy, both as a part of a two-body system with the Milky-Way |19| and on the level of the kinematics of stars inside the galaxy [20]. The second measurement is particularly important since it was the first that looked at the speeds of objects inside a galaxy and far away from the galactic center. Although this particular measurement could be explained with a high absorption of light by interstellar dust, the measurement done for NGC 3115 performed by Oort [21] could not. More thorough observations have since been performed, using the Doppler effect to gauge the speeds of stars in the galactic disks of many spiral galaxies. Especially the measurements performed by Vera Rubin's group in the 1970s laid a foundation in the field [22]. The result of these measurements are the so-called rotation curves, as the one observed in Fig. 2.4 for the Milky Way, where the average star velocities are plotted with respect to the distance from galactic center. If the matter was distributed only in the galactic disc, the rotation curve would fall with 1/r, while all measurements result in a rotation curve that is practically flat. Such a dependence would suggest extra matter that has a spherical distribution. It has been therefore hypothesised [24, 25] that the extra matter resides in the so called galactic halo, a sphere of non-visible matter that engulfs the galactic disk and usually carries more than ten times as much weight as the galactic disk.

2.2.2 Cold Dark Matter

The observations of the Coma Cluster, and galaxy rotation curves are considered to be one of the most important evidence for the existence of Dark Matter, but it is important to realize, that at the time it was thought that this extra matter was baryonic or at least composed of a known entity. At first, in the 1970's neutrinos seemed to be a good candidate for Dark Matter [26]. At the same time, the idea, that something new might be hiding in the Universe began to surface. In 1981 it was shown [27] that Cold Dark Matter could solve the problem of the, at the time, missing fluctuations of the Cosmic Microwave Background. Cold in this context means that Dark Matter, whatever its nature, would cool down earlier than standard baryonic matter. The attractiveness of this scenario lies in the fact, that baryonic matter could not form structures while it was in thermal equilib-

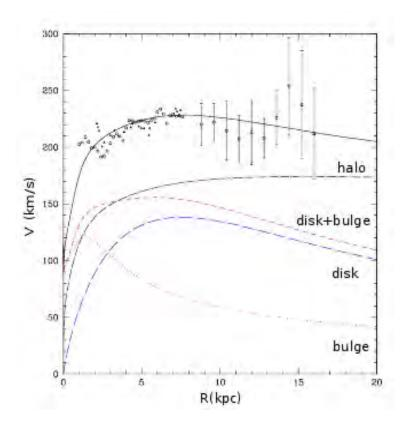


Figure 2.4: The rotation curve for the Milky Way, apart from the measurements of the rotational velocity, the mass distribution components (bulge, disk) of the galaxy are shown as well. Image taken from [23]

rium with the photons present in the Universe, and this was true all the way until Recombination, which happened at a redshift $z \simeq 1000$, so when the Universe was about 1000 times smaller than it is now. It is known that the Universe is currently inhomogeneous, with the fluctuation rate approaching one, as determined with the so called σ_8 parameter which measures the scale of inhomogeneity in an 8Mpc cube. The most recent measurements give $\sigma_8 = 0.812 \pm 0.026$ [4]. Incidentally, another obvious proof that the fluctuations do exist is the fact, that we, the Earth, stars and galaxies all exist. To evolve into what we see today the fluctuations at the time of Recombination would have had to have been of the order of at least 10^{-3} , as they grow linearly with a(t) (defined in Equations (2.2)-(2.4)). Already in the late 1970s it was realized that this is not the case, since the measurements of the CMB observed no fluctuations at this level [28]. A possible solution was that something, would begin to form these structures earlier, i.e. was already "cold" at the time of Recombination and the baryons, once detached from thermal equi-

librium, could fall into the gravitational potential wells of these proto-structures. With this mechanism the formation of the visible structures could be sufficiently accelerated to compensate the smaller than expected fluctuations in the CMB.

The fluctuations in the CMB were actually observed only in 1992 by the COBE satellite [13] and were found to be at the level of $10^{-5} \frac{\Delta K}{K}$, thus confirming the Big-Bang model but emphasizing the need for an extra component in the scenario. The measurements of COBE have been confirmed by the WMAP probe providing a lot more insight, especially since the 7° resolution of COBE allowed to observe only such fluctuations that evolved into scales larger than the current visible Universe. The much better resolution of WMAP allows us to see CMB fluctuations on a scale that corresponds to the structures we see today. This was seen as further proof of the Cold Dark Matter scenario and so, the Cosmological Model is sometimes called the Λ Cold Dark Matter (or Λ CDM) model [29].

2.2.3 WIMPs as Dark Matter

Since Dark Matter needs to be cold at Recombination, the most natural hypothesis is that it is in the form of particles that are heavier and so would detach from thermal equilibrium earlier than baryons and could begin the process of forming the structures we see today. There are caveats though. These particles should not be able to interact with ordinary matter, except gravitationally or weakly, and should not be too light, else we would have seen them either in the observations of the sky, or in the accelerator experiments. These hypothetical particles have been dubbed Weakly Interacting Massive Particles or WIMPs. There are numerous different ideas about the nature of Dark Matter, but the WIMP model is by far the most popular, and the one we will concentrate on in this thesis.

One of the reasons that the WIMP scenario is so compelling, is the following reasoning. Let's assume we have a hypothetical particle w. As mentioned before, at the beginning of the evolution of the Universe w is in thermal equilibrium with radiation. This means that particle-antiparticle pair creation and annihilation are equally fast. During this period the number density (number of particles per unit volume) of these particles $n_w \propto T^3$, with T as temperature. However, when the temperature falls below the mass m_w the density of the particles begins to behave like:

$$n_w \propto (m_w T)^{-3/2} \exp(-m_w/kT).$$
 (2.9)

The number of the creation and annihilation interactions dramatically falls, just as the number of the particles. At a certain point the energy of the photons becomes too small to create new particles, later the density n_w becomes too small to sustain any further annihilation reactions and the amount of w particles becomes frozen out at a certain level. The smaller the average reaction rate $\langle \sigma v \rangle$ (σ is

the interaction cross-section, v is the relative velocity of the particles), the more particles survive the detachment from radiation. It is actually possible to calculate the energy density coming from the particles surviving freeze-out [2]:

$$\Omega_w h^2 \simeq \frac{3 \times 10^{-27} \text{cm}^3 \text{s}^{-1}}{\langle \sigma_{ann} v \rangle},$$
(2.10)

where we define $\Omega_w = \rho_w/\rho_{crit}$ and h is the so called Hubble parameter that is defined via the Hubble constant: $H = h \times 100 \text{ km s}^{-1}\text{Mpc}^{-1}$, and its latest measured value is $h = 0.701 \pm 0.013$ [4]. It just so happens, that if we introduce a particle with a mass of around 100 GeV/c^2 and a cross-section of the order of the weak interaction, which is very probable from the point of view of extensions of the elementary particle Standard Model like Supersymmetry, we obtain an abundance of the w particles that is very close to the needed abundance of Dark Matter.

2.2.4 Numerical simulations

In recent years, thanks to the rapid increase in available computing power, it became possible to simulate the formation of structures in the Universe to test the Λ CDM model. It is worth noting, that the collapse of fluctuations, like those of the CMB, and the subsequent build-up of structures is a highly nonlinear process and so, can be probed only by numerical simulations [30]. The simulations are usually performed by creating a block of space and filling it with particles. The term particle may be misleading, since the objects in question are currently of the order of 10⁹ solar masses - the size of a small galaxy. In most simulations these particles interact only gravitationally, since simulating gas interactions and hydrodynamics is much more demanding in terms of computing power. So, in a way, these simulations only take into account the evolution of Dark Matter. To have an idea of how the baryonic component behaves, which is important mainly on the scale of galaxies, semi-analytical models are used during the post-processing of the simulations. The largest simulation of this type so far has been the Millennium simulation [31], which simulated 2160³ particles with a mass of $8.6 \times 10^8 h^{-1} M_{\odot}$, where M_{\odot} is the Solar mass, in a box with a side of 500 h^{-1} Mpc. The particles' initial position was perturbed using software imitating Boltzmann fluctuations. The Λ CDM model parameters - Ω_m , Ω_b , h, Ω_Λ , n and σ_8^2 were used as input of the simulation. A quick glance at Fig. 2.5, where the results of the Millennium Simulation are compared with the results of the Large Scale Surveys shows an astounding resemblance between the 2dFGRS [14], SDSS [15] and CfA2 [32] measurements and the corresponding simulation. Qualitatively it is plain to see that

 $^{^2\}Omega_x = \rho_x/\rho_{crit}$, the index m signifies total mass, b - baryonic mass, Λ - the cosmological constant, n is the so called scalar spectral index.

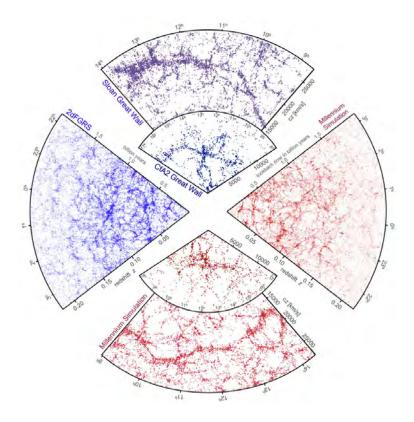


Figure 2.5: A comparison of the 2dFGRS, SDSS and CfA2 sky surveys (left, top and top cut-in) with mock catalogues created from the Millennium simulation (right, bottom, bottom cut-in respectively). The dots in the graph represent single galaxies. The results of the simulation have been chosen to reflect the parameters of the surveys. Figure taken from [33].

the simulations can model the known Universe, even using the rough approximations specified before. But also on a quantitative level, the simulations reproduce the known Universe quite well and make predictions about parameters that can be measured to provide further confirmation of the ΛCDM model, such as the baryonic acoustic oscillation peaks, which are an effect of the sound waves traveling in the baryonic matter just before Recombination that should be imprinted in the distribution of matter in the Universe [31] - the same imprint in the CMB has been observed as the WMAP result.

The main point in which the simulations could be improved is how the structure formation affects smaller scales. For this, two approaches can be taken, one is to increase the number of particles and make them smaller to see how this affects halos on the galaxy scale. Although on this level the baryon component may begin playing a significant role, so the other approach is to begin introducing baryons. Such a simulation has recently been performed, and is called the MareNostrum simulation [34]. This simulation had less particles - 2×1024^3 and they were heavier than in the Millennium simulation - $m_{DM} = 8.3 \times 10^9 h^{-1} M_{\odot}$, but half of the particles behaved like a baryon gas, even though the particle masses were of the order of $m_{gas}1.5 \times 10^9 h^{-1} M_{\odot}$. This allowed for a more realistic simulation than the application of semi-analytical models, although next stages with smaller particles, following improvements in computing power and parallel software techniques, are definitely needed. Anyhow, the MareNostrum simulation gives the same view of the Universe as that of the Millennium simulation, the matter in the Universe, be it dark or baryonic bands together into clusters and filaments, sometimes called the "cosmic web" [35]. It is amazing to see, that even a simulation consisting only of Dark Matter particles, like the Millennium Simulation, visually reproduces this "cosmic web" almost perfectly.

The success of these simulations in reproducing observational data gives strong support to the Λ CDM model, and what is more, confirms the main role that Dark Matter played in the structure formation of the Universe. Therefore giving strong, if indirect, evidence of its existence.

2.2.5 Weak lensing

The filaments in the "cosmic web" have been observed by other means, not only by direct observation by Large Scale Surveys. Other surveys have been performed to search for the gravitational effects of the invisible Dark Matter structures, via the so-called weak lensing [36]. The method uses the gravitational lensing effect, predicted by Einstein and observed by Eddington in 1919, which became one of the first confirmations of General Relativity. The effect is based on the fact that photons, just like particles with a mass, are affected by gravitational fields and can be deflected when passing next to massive objects thereby distorting the optical images that arrive to the observer.

Actually, it is sometimes possible to observe objects found directly behind massive clusters that, if not for gravitational lensing, would be obscured from our view. Instead, the light coming from them is deflected and arrives to Earth. Unfortunately most objects in the Universe do not act as strong lenses, that produce arcs or multiple images - typical signatures of gravitational lensing. Even so, they still affect the visible shape and size of objects behind them causing deformations that break down into two components called convergence - the magnifying of the background objects and sheer - their elongation tangential to the lens. For weak lensing objects the changes in the images are small and it is usually not possible to tell looking at a single galaxy whether its image has been deformed. Especially because most galaxies already have elliptical, elongated shapes.

It is possible to invert the problem and study the foreground objects, the lenses themselves, to see what is the mass distribution inside them. It requires performing a large scale statistical analysis of the galaxies and luminous objects of the background and then using the result of this as a template, when searching for deformations caused by weak lensing. This method is often applied to clusters and galaxy-galaxy lenses. The weak lensing coming from large scale structure is even weaker, but the idea of its observation has been proposed as early as 1967 [37]. Only recently the observation and computing technology have become good enough to actually succeed in this task. These measurements make it possible to independently measure the amount of matter in the large scale structures. One of the surveys, the CFHTLS recently published results of their observations [38] and when their results are combined with WMAP to reduce the degeneracy in the, previously introduced, coefficient σ_8 with Ω_m , the combined datasets yield an $\Omega_m = 0.248 \pm 0.019$, perfectly consistent with the Dark Matter scenario. There are several other surveys searching for the same effects, and more information can be found in [39].

2.2.6 The Bullet Cluster

Possibly the most spectacular evidence for the existence of Dark Matter is the observation of the galaxy cluster merger 1E0657-558, also known as the Bullet Cluster [40]. The observations pertain to two galaxy clusters, colliding practically in the plane of the sky. The cores of the clusters passed through each other $\sim 100 Myr$ ago. When observing the clusters, optical instruments were used to observe the stars and luminous objects, while X-ray telescopes were used to detect the hot baryon plasma present in galaxy clusters. The optical observations were also used to estimate the mass distribution in the clusters via the weak lensing method described before. These observations made it possible to see if the mass distribution follows that of baryonic matter. During a cluster merger the stars and galaxies, which sparsely populate the cluster (luminous matter is 0.5% of critical density, and 10% of baryonic matter) pass through without any hindrance. The hot intracluster plasma which behaves almost fluid-like experiences ram pressure during the collision, and stays behind. This is shown on Fig. 2.6 where the hot plasma is colored red and the galaxies, i.e. luminous matter are colored blue. The lines represent the matter distribution obtained from weak lensing. It can be seen from the contours, that the mass distribution follows the galaxies, which act like collisionless particles. What is important to understand is that the hot plasma accounts for most of the baryonic mass in galaxy clusters. If Dark Matter did not exist, the mass distribution should trail the intracluster plasma, which would be the leading matter component of the cluster. If, on the other hand, Dark Matter exists, then it would behave like the galaxies and pass through the collision zone unhindered. In this case the mass distribution would trail the luminous galaxies. As can be seen in Fig. 2.6 the second case is true. The observations allowed to set an 8σ spacial offset of the center of total mass and the center of the baryonic mass, and is considered the strongest evidence against modified gravity theories explaining the mass-energy of the universe without Dark Matter. These will be discussed in the next section.

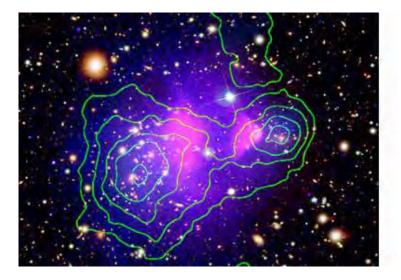


Figure 2.6: A photo of the merger in the Bullet Cluster. The blue color denotes the luminous matter - galaxies and stars, the red color denotes the X-ray emitting baryon plasma. The contours show the mass distribution in the cluster determined via weak lensing [40].

2.3 Alternative explanations to the Dark Matter phenomena.

The Standard Cosmological Model, though widely accepted by cosmologists and astrophysicists, is not the only possible explanation of the cosmological observations, nor is the model without problems. First we will focus on the problems and observations that are not explained well in the model to later turn to alternative theories and models.

2.3.1 Standard Cosmological Model vs galaxies

It is widely agreed that the ΛCDM paradigm does exceptionally well in explaining the Universe on cosmological and large scales. On the galaxy scale however, there are some unresolved problems. In fact, some believe that the predictions about the galactic halos might even become the proverbial "Achilles heel" by which the Cosmological Model will be falsified. The parameters of the galactic Dark Matter halos can be estimated using more and more precise galaxy scale numerical simulations. The results of these differ, sometimes significantly, from observations especially for low surface brightness and dwarf galaxies that have rotation curves that are not as steep as those predicted from the simulations [42]. Another problem is that the simulations predict a large number of surviving satellites, that should orbit the galaxy, but which are not observed. This is known as the missing satellite problem. There are suggestions that the surviving haloes are invisible either due to astrophysical processes or because they are made up of only Dark Matter [43, 44]. In both cases the confirmation should come from lensing experiments [45].

In defense of the Λ CDM model it is argued that the process of galaxy creation is not yet well understood and so it is possible that the discrepancy between the predicted halo profiles and the observed ones is not a result of the Λ CDM model, but of the false assumptions and input that are inserted into the simulations. There are, however, specific cases where it seems that it is impossible to reconcile a spherical Dark Matter halo with the observations of the rotation curves. One such galaxy is the NGC 4736 [46], where by using a precise method to fit the data it is possible to recreate the rotation curve using only matter found in the galactic disc.

Recently a new measurement has been published where a large sample of galaxies has been compared in search of correlations between their parameters [47]. The surprising result was that most of the parameters attributed to the galaxies are correlated and in the end the galaxy distribution could be described with only one, undetermined as of yet, parameter. This finding is also a difficulty for the Λ CDM model since, if the galaxies were formed as it predicts, then they should depend on five different parameters, namely mass, angular-momentum, baryon-fraction, age and size, as well as on the accidents of its recent haphazard merger history. The discovered high degree of organization in the structure of galaxies is very hard to obtain in the framework of Λ CDM.

There are also works, that suggest that the Cosmological Model could do quite well without the Dark Energy component. Such suggestions arise from the idea that the Supernovae Ia measurements are not so thoroughly understood, for example the metallicity component might introduce a change in the calculated brightness and hence distance from these stars. So, if on this assumption, one discards the SN Ia measurements, most of the cosmological data can be fitted with a De Sitter, flat, expanding Universe where the critical density is filled with only the baryonic component. The caveat is that this model requires the value of the Hubble constant $H \sim 40 \text{ km/(s Mpc)}$ which is much lower than the currently established value of 70 km/(s Mpc) [48].

2.3.2 Alternative theories of gravity

The problems of the Λ CDM model, especially the galaxy scale discrepancies, have spurred a number of alternative models and theories that try to explain the visible data better. A whole class of these models are the so called Modified Gravity Theories, of which MOND and its relativistic successor, TeVeS play a major part.

MOdified Newtonian Dynamics was first suggested in 1983 by Milgrom [49]. The idea behind it is rather simple - Newton's law of gravity does not work in all of space as was previously thought, only in regions where the acceleration is sufficiently large. However, when the acceleration passes below a certain threshold, called a_o , which is a parameter of the model, gravity begins to work differently, obeying the equation

$$a_N = \mu(\frac{a}{a_o})a\tag{2.11}$$

where a_N is the standard Newtonian acceleration, a is the MOND acceleration, $\mu(x)$ is a function that returns 1 for x >> 1 and x for x << 1. When applied to the galaxy rotation curves and the cluster dynamics MOND was able to explain the observations using only baryonic matter and the single free parameter $a_o =$ $10^{-8}cms^{-2}$, which is at the very least a remarkable coincidence. MOND is also able to explain the so called Tully-Fisher relation in galaxies which ties the surface brightness of a spiral galaxy with its rotation speed. There are, however, misgivings about accepting MOND as a serious theory. First of all, it is not really a theory, more of a phenomenological approximation. For instance, if MOND is used as is, energy and momentum would not be conserved. There was a lot skepticism regarding the possibility of including MOND in the theory of General Relativity, which up to now has been extremely successful in passing all observational tests. One of the main problems with the lack of a relativistic MOND theory is that it does not reproduce the effects of gravitational lensing, which was one of the first successful tests of General Relativity. Another problem for MOND was its behaviour on the scale of Galaxy clusters. Inside the clusters, there is an enormous amount of ionized gas which is assumed to be in thermal equilibrium. To achieve this state enough gravitational pressure must be exerted on the gas to hold it in place and balance the thermodynamical pressure resulting from the high gas temperature. The location of the gas and its abundance can be deduced from the X-ray radiation, that is emitted thermally. The profiles of the intracluster gas are in very good agreement with Λ CDM predictions of the cluster Dark Matter halo, while for MOND it seems that an extra amount of Dark Matter is needed to stabilize the system [50]. The need for Dark Matter in a model that was conceived precisely to get rid of it, is a serious problem. The only possibility to circumvent this problem is if neutrinos could play the part of this missing Dark Matter. For this to happen they would have to have a mass that is not smaller than 2eV, which should be probed by the next generation neutrino mass experiments like KATRIN.

Since the main reason, why MOND was discarded was the lack of correspondence with General Relativity, attempts were made to create a theory that would combine it with Einstein's theory [52]. None of them were fully successful in the task, until Bekenstein published a theory called TeVeS - Tensor-Vector-Scalar [53] which scales down to General Relativity, Newtonian physics or MOND depending on the choice of its intrinsic parameters. The parameters can be chosen in such a way, that during the early evolution of the Universe it reduces to General Relativity thereby duplicating the success of its description of the evolution of the Universe. Some attempts have been made to gauge the agreement of TeVeS with the Big Bang scenario and CMB measurements more precisely [51] and it looks as if it is in fact capable of reproducing the results of the observations. There are also claims that the analysis of the Merger in the Bullet Cluster has been misinterpreted and hence does not disprove the MOND/TeVeS scenario [54]. So it is in fact possible that an alternative theory like TeVeS is a probable alternative to the Dark Matter observations. One should observe, however, that MOND and TeVeS do not explain the Dark Energy or Cosmological constant part of the equations so a new entity is still needed. TeVeS is a new theory and the discussion of its validity is ongoing. Resolving this argument lies far beyond the competence of the author and the scope of this thesis.

There are other ideas being developed in the field of alternative gravitation theories, like conformal gravity [55] or STVG (Scalar Tensor Vector Gravity) [56] some of which make an attempt to explain Dark Energy component as well as that of Dark Matter, but the MOND and, consequently, TeVeS are the most recognized.

Chapter 3

Searches for Dark Matter Particles

The fact that 95% of the mass of the Cosmos is unknown has been a strong incentive for astrophysicists to devise experiments that could shed some light on the unknown components of the Universe. Dark Matter seems to be the more mundane and predictable than Dark Energy, so much more effort has been put into its detection and the determination of its properties. A very large and growing experimental effort is devoted to searching for the possible components of Dark Matter, especially with the means of direct detection.

3.1 What is Dark Matter - a review of the hypotheses

As mentioned before, the most popular hypothesis explaining the nature of Dark Matter is the WIMP scenario. This model requires the introduction of new particles beyond the particle Standard Model, but since particle physicists think that the Standard Model should be expanded anyway for reasons like the existence of neutrino masses, insufficient CP symmetry violation and the unification of the electro-weak and strong interactions into one, this is not considered to be that much of a problem.

Currently, the most popular expansion of the Standard Model is called Supersymmetry. This theory assumes that for each known particle a supersymmetric partner particle, called a sparticle, exists. Sparticles would have a spin different by 1/2 with respect to the spin of their partners so sfermions would act as bosons and sbosons would be fermions. The most enticing property of Supersymmetry is probably the fact, that if the supersymmetric particles were not much heavier than a few hundred GeV/c^2 it would allow the coupling constants of strong, weak

and electro-magnetic interactions to intersect in one point on the coupling-energy plot (see Fig. 3.1) making the unification of the three interactions possible.

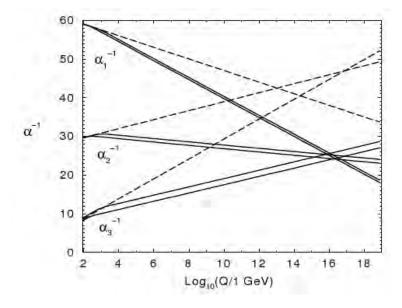


Figure 3.1: The running of the inverse coupling constants with energy, assuming that only Standard Model physics exist (dashed lines) and adding Supersymmetry (solid lines) [57].

As a sort of unexpected bonus for cosmology is that Supersymmetry can provide a very good candidate for the WIMP. There is a large number of supersymmetric models, but most of them agree that the lightest particle should have a mass around a hundred GeV/c^2 . In order to prevent the proton decaying faster than the current experimental limits, depending on the decay channel [58], Supersymmetry requires the introduction of a discrete symmetry called R-parity. As a result a supersymmetric particle cannot decay into only nonsupersymmetric particles, which leads to the lightest supersymmetric particle being stable. It is usually called the LSP - Lightest Supersymmetric Particle. In many Supersymmetric models, like the CMSSM (Constrained Minimal SuperSymmetric Model) [66] the LSP is usually a particle with no electric charge, which is a superposition of the Zino, Photino, Higgsino (partners of the Z, photon and Higgs bosons, respectively) called the neutralino (χ) which would be a perfect candidate for the Dark Matter WIMP.

The WIMP is not limited to Supersymmetry though. Other extensions of the Standard Model can also produce a heavy particle, that interacts weakly with standard matter. A prime example is the Kaluza-Klein extra dimensions model,

where the lightest Kaluza-Klein particle (LKP) can act as the WIMP, although it is predicted that it would be rather heavier than the LSP - between 400 and 1200 GeV/c^2 [59, 60].

Another rather popular hypothesis is that of axions. These particles, if they exist, would be a solution to the so called strong CP problem in Quantum Chromodynamics (QCD). The problem lies in the fact, that there are no theoretical constraints to introducing a CP breaking term into the strong interaction Lagrangian. However, CP violation has not been observed in strong interactions, which means that if such a CP breaking term were introduced it would have to be scaled by a factor θ of at least 10^{-9} . Again, there is no theoretical motivation for the existence of such precise fine-tuning. It is much more prudent to introduce a scalar field, that would cancel the CP violating term from the Lagrangian in the following manner [61]:

$$\theta_{eff} = \theta + \frac{a(x)}{f_a},\tag{3.1}$$

where a(x) is a scalar field that will be called the axion and f_a is the axion decay constant. If the QCD Lagrangian would be invariant with regards to the Peccei-Quinn symmetry:

$$\frac{a(x)}{f_a} \to \frac{a(x)}{f_a} + \delta,\tag{3.2}$$

then it would be possible to gauge it in such a way, that $\theta = 0$ which restores the C and CP invariance of the whole Lagrangian, while the θ_{eff} remains small because of its dependence only on the scalar field.

The axion, a new particle resulting from the scalar field, could have a mass in the range of 10^{-6} to $3 \cdot 10^{-2}$ eV/c² [62] and for a mass around 10^{-5} eV/c² it could have an abundance corresponding to that expected of Dark Matter. One should note, that these particles would not be created thermally, so their small mass does not exclude them from acting as Cold Dark Matter at the time of Recombination. The axion might be detected by its conversion into two photons in a strong magnetic field via the Primakoff Effect. Fig. 3.2 presents the current exclusion limits in the axion searches.

There are numerous other hypotheses like WIMPzillas or self interacting Dark Matter, but their discussion is beyond the scope of this thesis. However, I would like to mention one other model, which is Mirror Dark Matter. This model requires that for each elementary particle a mirror partner exists which has exactly the same quantum numbers except for parity. This idea first emerged as an attempt to preserve parity as a symmetry of nature, since it is maximally broken in weak interactions. If Mirror Matter existed, then parity on the whole would be conserved. Much later it has been noted that Mirror Matter could play the role of Dark Matter, since its interactions with ordinary matter are very rare and occur

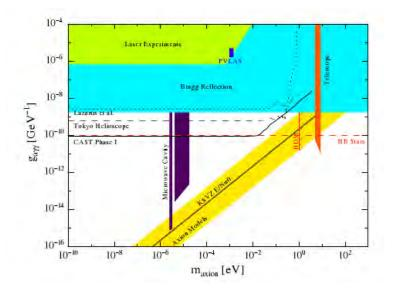


Figure 3.2: The current limits in the axion searches. The yellow line represents the properties of the axion predicted by theoretical models. It can be seen, that most experiments have not yet probed the region of the expected parameters. [63]

mainly through photon-mirror photon oscillations. It is possible that through some asymmetry in the evolution of the Universe Mirror Matter could be more abundant and differently distributed than standard matter [64], therefore satisfying the conditions for Cold Dark Matter.

3.2 What the collider experiments can tell us

So far, no particles beyond the Standard Model have been found. Even so, the accelerator experiments usually combined with theoretical results, can still tell us something about the WIMP. Most of the predictions are, unfortunately, dependent on the theoretical model, so it is impossible to cite absolute limits on the WIMP mass, even if we constrain ourselves to the Supersymmetric framework. One of the reasons is the fact, that the Minimal Supersymmetric Model (MSSM) [65, 57], has over 100 free parameters. A large number of theorists seem to believe, that the solution to this multi-parameter conundrum lies in the Constrained MSSM (CMSSM) [66] which is a special case of the MSSM, where many of the parameters are degenerate or the minimal Super-Gravity Model (mSUGRA) [67] which is an implementation of CMSSM. These models are dependent on only 5 free parameters, which is a number by far more manageable than that of the MSSM. Even so, there are numerous articles showing allowed parameter spaces or predicted properties

of the LSP neutralino. Most analyses are based on an algorithm that fixes one or more of the free parameters and by varying some of the others, results in acceptable ranges for the remaining parameters. From these, it is possible to extract the allowed regions of neutralino mass or cross-section if needed. One innovative attempt is that of [68], where the CMSSM parameters are varied based on Bayesian probability in a Markov Chain Monte Carlo simulation. This results in different prediction plots, where a probability density is shown for the expected parameters. One such plot can be found in Fig. 3.3, where the predictions for the neutralino as a Dark Matter particle are shown. It can be observed, that the χ mass is of the order of 200 GeV/c² and the most probable cross-section is of the order of 10^{-8} pb. This is an enticing possibility, since this is perfectly in the reach of the next generation experiments for the direct detection of WIMPs.

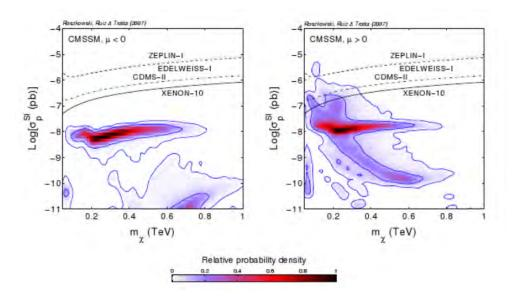


Figure 3.3: The probability density for the WIMP interaction cross-section and the χ mass for the supersymmetric parameter $\mu < 0$ (left panel) and $\mu > 0$ (right panel). The contours represent confidence levels of 68% and 95%. Current sensitivities of direct detection experiments are also plotted. Fig. taken from [68].

It is important to note, however, that if the assumptions that are the basis of the CMSSM are not correct, then the above result need not be true. For example it is possible to construct Supersymmetric models where the LSP is as light as 7 GeV/c^2 [69], [70] or indeed much heavier than 100 GeV/c^2 . The accelerator experiments, if they do not see new particles, can at least continue to exclude regions in the supersymmetric parameter space. The allowed supersymmetric parameter region can be narrowed down further by other results. Especially the results of WMAP

can give strong constraints if we assume that the LSP is in fact responsible for Dark Matter. The measurements of the anomalous magnetic dipole moment of the muon $a_{\mu} = (g-2)_{\mu}/2$ [72] can suppress the neutralino mass from above preferring models where its mass is in the few hundred GeV/c² region, while experiments observing the branching ratio BR($b \to s\gamma$) [68] can probe the regions of a light neutralino.

The optimistic scenario, however, is that we will see Supersymmetry in the LHC. There are of course many predictions, how it might be observed, but these are also model dependent. It seems that in most reasonable cases the LHC should see at least a few of the lightest sparticles: [73], [74] and references therein.

3.3 Indirect searches

Even though the WIMP mass and other properties are unknown it is still possible to look for effects of its presence in the galactic halo. This is where the indirect methods of detection concentrate on searching for the effects of the decay or annihilation of WIMPs. Especially in the vicinity of massive objects like the galactic center or the centers of the Sun and of the Earth. The processes in question can produce remnants like high energy photons, a surplus of positons or antiprotons (or antimatter in general) or extremely energetic neutrinos. Experiments observing γ rays and antimatter look for a surplus of particles over the predicted background, hopefully in the form of a narrow peak in the energy spectrum. Such a peak, if well defined, would allow a precise determination of the WIMP mass. The neutrino telescopes look for single energetic events coming from annihilations of WIMPs trapped in the gravitational potentials of the Sun and Earth. In this case a precise determination of the mass would be much harder, due to the small number of predicted events, as well as the challenges of neutrino detection.

At the time of the writing, at least two experiments have made claims of observing signals, that could be attributed to Dark Matter. One observation pertains to γ 's and the other one to a surplus of positons in the cosmic radiation. However, these results are still inconclusive and more precise measurements or longer data taking times are needed.

3.3.1 EGRET

The Energetic Gamma Ray Experiment Telescope, or EGRET was a satellite that detected gamma rays in the 20 MeV to 30 GeV energy range. Its large field of view allowed it to explore large parts of the sky. The main objective of the mission was to find and explore gamma ray point like emitting sources, but the observatory was also able to create a rather detailed map of the diffuse gamma ray background in the Milky Way galaxy.

Already after the mission has been closed, the data from EGRET were reanalyzed in order to search for WIMP signatures in the observed gamma rays [75]. The observed spectra were compared with the galactic background predicted from known sources by the GALPROP code [76]. A surplus of gamma rays was observed mainly in the direction of the galactic center, suggesting an unknown source of gamma rays, which could be attributed to WIMP annihilation in the denser parts of the galaxy. The EGRET satellite was not tailored for this kind of measurement, so the result needs to be confirmed by a more precise measurement like that of the GLAST satellite, which has been launched in June 2008. However, it is possible to speculate on the nature of the WIMP that could have caused the EGRET surplus. A WIMP preferred by these observations would have a mass of the order of 60 GeV/c^2 [75]. It has also been argued that to explain the observations two overdense caustic rings should be present in the galactic halo at distances of 4 and 14 kpc from the galactic center, causing more gamma rays to be observed from these regions.

3.3.2 **PAMELA**

Payload for Antimatter Matter Exploration and Light-nuclei Astrophysics or PAMELA is a satellite observatory, which observes the cosmic ray fluxes of matter as well as antimatter coming towards the Earth. Its other goals include observing the flux of particles coming from the Sun and high energetic particles in the Earth's magnetosphere. In the search for Dark Matter the feature of most interest is its capability to detect antimatter. If a surplus of antimatter, over the background expected from known sources was found, this may be a sign of WIMP annihilation, since in this process particle-antiparticle pairs would be produced. At the time of the writing of this thesis the PAMELA collaboration reported a surplus in positrons (namely in the $e^+/(e^+ + e^-)$ ratio) observed in the (10-100) GeV energy range [77], which could in fact be attributed to WIMP annihilation. There are already tens, if not hundreds of works based on this data release, trying to explain the surplus in terms of particle models. However, some works based on preliminary releases of this data [78] suggest that at this point is not possible to extract any significant parameters of the hypothetical WIMP, based solely on this data. It seems that more data taking is required to be able to confirm or reject the WIMP annihilation hypothesis.

Only a month later the surplus in antimatter observed by PAMELA has been confirmed by the balloon experiment ATIC [79], which analyzed the results of its flights in 2000 and 2003. This apparatus also sees a surplus, this time in electrons at an energy scale of (300 - 800) GeV. However, the ATIC results show

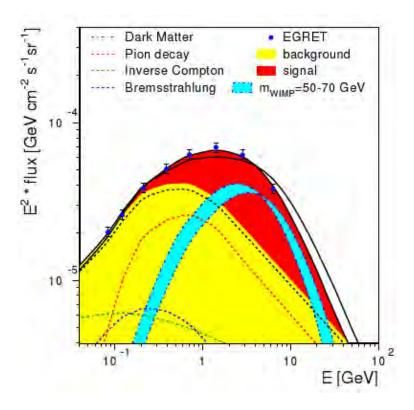


Figure 3.4: The analysis of the EGRET data compared with the background (yellow) and a hypothetical WIMP signal (red) [75].

a surprising structure in the data, see Fig. 3.5. Just like that of PAMELA it is hard to call the ATIC result conclusive. Also in this case, some more data remains to be analyzed, from the balloon flights in 2007-2008. In 2009 the PAMELA collaboration published the results of their proton/anti-proton observations, and these seem to dampen the claims of the Dark Matter origin of the previous data [80].

Even if the results of the PAMELA and ATIC experiments are confirmed, it will still be difficult to use them as a clear constraint on the WIMP parameters, since there are already at least 50 preprints claiming to explain these effects via different particle models.

3.4 Direct detection experiments

The most sound proof of the existence of Dark Matter will no doubt be provided by direct detection experiments. The accelerator data, even though it may measure

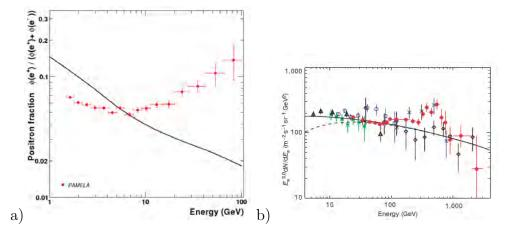


Figure 3.5: a) The recent results (red points) of the PAMELA satellite observatory [77] compared with theoretical predictions (line) and b) the ATIC balloon experiment measurement (red points) [79] compared with theoretical predictions (line) and previous experiments (other symbols). Both plots show a disagreement of the registered data and the predicted background suggesting a possible WIMP annihilation effect.

properties of new particles precisely, can at best provide a candidate for the Dark Matter particle. The indirect searches, on the other hand, rely strongly on a good model of the expected background and it can be argued that the models of the galactic gamma ray and antimatter fluxes are not well understood. It is the direct detection experiments that are conducted in the laboratory so the background can be controlled and, if a signal is registered, it will be the signature of the very particles found in the galactic halo. So, one could argue that the ultimate proof of Dark Matter will come from a direct detection experiment.

Direct detection experiments rely on the hypothesis that the Dark Matter particle will react with the nuclei of atoms in the detector via elastic scattering. The WIMP can transfer some of its kinetic energy to a nucleus. The recoiling nuclei can then be seen in the detector. This task is, however, extremely difficult. First of all it is supposed that the WIMPs have a speed of the order of 220 km/s with respect to the Earth so the energy transfer governed by the following equation:

$$E_R = \frac{4M_W/M_T}{(1 + M_W/M_T)^2} E_W, (3.3)$$

will be very small. Here E_R is the recoil energy and E_W is the WIMP kinetic energy and M_W and M_T are the WIMP and target atom masses respectively. The energy transfer generally amounts to about (10 - 100) keV depending on the detector nuclei and the WIMP mass. It is also important to remember that the WIMPs

interact weakly - current experimental limits place the cross-section for interaction as low as 10^{-43} cm² per nucleon, which will result in event rates of the order of 10^{-2} evts/(kg days). For these reasons direct Dark Matter detection experiments are an experimental challenge completely different than building detectors for accelerator experiments. First of all, the background must be understood and reduced to a level much lower than for the majority of physics experiments. Practically all detectors are placed deep underground in order to shield the active volume from cosmic rays. Additional shields are also placed around the detectors to minimize the gamma rays and neutrons coming from the environment. Care is also taken to construct the detectors from low background materials.

Currently, most detectors, that I will call second phase, have a method of differentiating events caused by energetic photons and electrons from events caused by the recoils of neutrons or WIMPs. Thanks to this, it is possible to focus on lowering mainly the neutron background, since only these interactions can mimic the WIMP signature, while the electron-like events can be rejected. If a suppression of the events coming from neutron recoils can be achieved as well, then any recoil-like event observed within the detector will have to be a WIMP and hence be the "smoking gun" of discovery.

Another possibility for discovery is to search for the so called annual modulation effect. If we assume that the WIMP galactic halo is a cloud of gas with a Maxwellian distribution then the average speed of the WIMPs with respect to the Solar System is the rotational speed of the Sun orbiting the galactic center. If we remember that the Earth also orbits the Sun, then its speed may at some point of the year add itself to the speed of the Sun and half a year later it would be subtracted. The times when these phenomena should occur are known and happen around the beginning of June and December, for the parallel and antiparallel speed alignment, respectively. If one notes, that a higher average WIMP speed results in a higher average recoil energy transfer and so a higher number of WIMPs that could survive the energy threshold in a detector, then if a surplus of events would be seen in June and a deficit in December this could be considered proof of Dark Matter interactions. There is also the possibility of observing a diurnal effect, but to register it a directional detector is needed.

The recoil energy coming from the WIMP collisions can manifest itself as scintillations, ionization or phonons - vibrations of the lattice in crystals. If a detector is able to register more than one of the forms of the deposited energy it usually obtains a strong background suppression method. There are, however, detectors which register only one of these signals. A sum up of the experiments based on their detection methods can be found in Fig. 3.6. The DAMA, CDMS, XENON detectors will be described with more detail and experiments using argon will be mentioned as well.

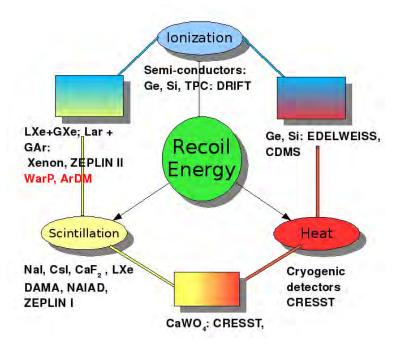


Figure 3.6: The direct detection experiments divided by the means by which they detect the WIMP recoil energy.

3.4.1 DAMA

The abbreviation DAMA comes from the words DArk MAtter. It is possibly the best known experiment searching for Dark Matter and definitely the one with the most acquired data. DAMA began operation in 1996 with the DAMA/NaI detector using 100 kg of NaI(Tl) scintillation crystals. The apparatus was in continuous operation until 2002, when the next phase of the experiment DAMA/LIBRA began to be constructed. Data taking with the new detector was initiated in 2003. 2008 saw the first data release of the DAMA/LIBRA setup [81] which is the result of a total exposition of 0.82 ton×days.

The new detector uses the same principle as the DAMA/NaI setup and consists of 250 kg of crystals. Both detectors were placed in the underground laboratory in Gran Sasso, Italy. Two photomultipliers (PMTs) viewing each of the crystals are capable of detecting scintillation signals caused by the recoils. A strong point of DAMA is the fact that the technology is very well understood. Even so, the physicists working in DAMA have been able to achieve a great experimental task in lowering the residue radioactive background and perfecting the technology.

The experiment does not use any active background rejection methods, choosing to accept all counts in the crystal and focusing on observing the temporal

signature of the annual modulation effect. The DAMA experiment has reported observing the annual modulation and hence claimed to discover Dark Matter. Fig. 3.7 presents the plots of this signature from the combined results of the two DAMA detectors [81]. The registered counts can be seen in three energy ranges 2-4, 2-5 and 2-6 keV_{ee} , where the symbol ee denotes the so called electron equivalent. This signifies, that the energy is presented as if it were the result of electron interactions. This differentiation is due to the so called quenching effect, which causes nuclear recoils to generate less light than electron or photon interactions for the same energy transfer by a quenching factor q. The quenching effect will be discussed with more detail later in Chapter 5. The modulation observed by DAMA peaks around the 2nd of June and has a minimum in December as would be expected. The quoted period of oscillation is 1 year. The first publications suggested that this result would prefer a WIMP with a mass between 30 GeV/c^2 and 200 GeV/c^2 and a cross-section, normalized to nucleon, between 10^{-41} cm² and 10^{-42} cm² [82]. However, when other experiments capable of rejecting electron-like events began to exclude the region preferred by the DAMA result, the prediction of the WIMP parameters has been abandoned in the collaboration publications. It is currently claimed by the DAMA collaboration, that the new experiments cannot disprove their result, because of model inconsistencies. The DAMA result remains unconfirmed, except for the result of the DAMA/LIBRA.

3.4.2 Cryogenic crystal detectors

A whole class of detectors are the so called cryogenic detectors which try to detect the vibrations of the crystal lattice induced by a WIMP-atom collision. These phonons are very hard to detect since, because of the minuscule recoil energies involved, they correspond to a very small change in the detector temperature. To make detection possible the detectors must be kept in an environment with a temperature of the order of tens of mK, which is an extremely challenging task. These detectors are therefore very hard to operate, and so far their development in terms of mass has not been very fast. Still, one of the best limits on the WIMP parameters comes from one of such detectors - CDMS II [83].

This detector is a second phase of the CDMS project which concentrates on creating a detector using germanium and silicon crystals as the detector medium. These crystals are stacked in towers and the detector at the current stage consists of a total of 19 Ge and 11 Si detectors totaling an active mass of 4.75 kg Ge and 1.1 kg Si. The detector is placed in the Soudan underground mine and kept at a constant temperature of 40 mK using a dedicated cryogenic system. A powerful background rejection technique is used to eliminate all events coming from gamma and electron interactions. This is achieved thanks to the fact that the CDMS detector registers the phonons and ionization. The ratio of ionization to total deposited energy,

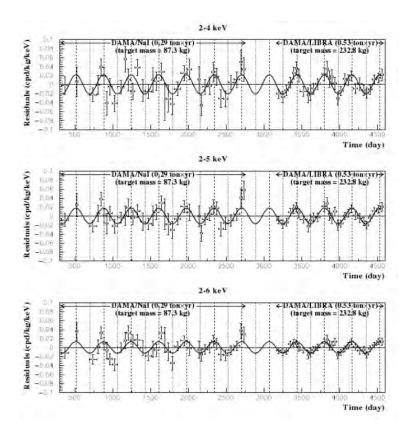


Figure 3.7: The observation of the annual modulation signal by the DAMA/NaI and DAMA/LIBRA detectors. The three plots show three energy windows in which the oscillation has been observed, notably 2-4, 2-5 and 2-6 keV_{ee} [81].

measured via the temperature change is different for electrons and gammas and for neutrons. It is expected that a WIMP signature should closely resemble that of the neutron since it is also a neutral particle and could interact only with the nuclei of target atoms. The power of the CDMS rejection technique can be seen in Fig. 3.8, where the results from the most recent data run are shown. Additional care is also taken to eliminate surface electron events, which might imitate nuclear recoils.

These results, for 123.1 kg×days of data taking, published in 2007, allowed the CDMS collaboration place a limit on the WIMP-nucleon scattering cross-section, which is much lower than the values preferred by DAMA [82], see Fig. 3.9.

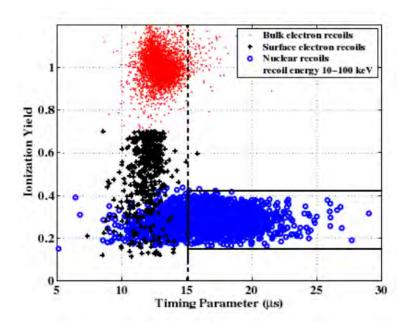


Figure 3.8: The CDMS II background exclusion technique. The timing parameter is based on the registered phonon pulse and its delay with respect to the ionization pulse. Red dots are electron-gamma like events, blue circles are the recoil like events, while the black points represent the surface electron-gamma events. The timing cut used in the data analysis is shown [83].

3.4.3 Cryogenic noble liquid detectors

The field of cryogenic noble gas detectors is growing very rapidly. In the field of Dark Matter detection especially xenon is being used in several experiments [85],[86]. The research and development is not limited to xenon, since argon is also a strong candidate [87], [88] and there is some activity regarding neon as well [89]. The main strong point of the noble liquid detectors is their chemical inertness and therefore easiness to achieve chemical purity. Another strong point is their scalability with regard to cryogenic crystal detectors - even though they had a late start, the masses of the noble liquid detectors already exceed those of the competition (i.e. 15 kg in XENON 10, 12 kg in ZEPLIN III and 3.2 kg in WArP) and the nearest future should bring an even larger difference, since 100 kg XENON, 144 kg WArP and 1 ton ArDM detectors are planned to operate in the nearest few years, as compared to the ~ 6 kg of CMDS II (and proposed 25 kg of SuperCDMS). The noble liquids also have very interesting scintillation properties that allow for strong background reduction; these will be described with more

detail in the next chapter of this thesis.

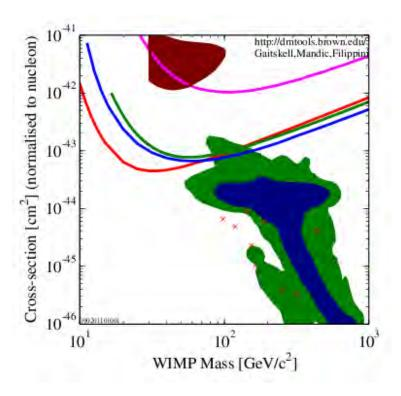


Figure 3.9: The current experimental situation for direct detection experiments. The brown area is the WIMP preferred by the DAMA result, the lines present exclusion plots for the CDMS (blue), XENON (red), ZEPLIN(green) and WArP (pink) experiments. The blue and green areas are theoretical predictions. Plot from [84].

XENON

XENON is currently the most advanced direct Dark Matter search experiment with a detector using a noble liquid. As the name implies the detector uses xenon as the detector medium. The detector operates using the so called two-phase technology, so both gaseous and liquid xenon are present in the chamber. The 15 kg of liquid are used as the actual target. The ionization is recorded indirectly, by registering secondary scintillations in the gaseous phase caused by electrons extracted from the liquid using an electric field present in the chamber. The double phase detection technique will be described with more detail in the next chapter, since it is the same principle on which the WArP detector operates. Suffice to say

that both the primary and secondary scintillation light resulting from a particle interaction are collected in the 89 PMTs observing the active volume from the top and bottom. The separation of electron-like events from neutron-like events is obtained with the ratio of scintillation to ionization. Even though the detector has a mass of 15 kg, a part of it was used as an active shield thanks to the good stopping power of xenon. Because of this, the published results used an exposition of only 58.6 kg×days. Even so, the XENON collaboration was able to achieve an extremely low detection threshold of 5 keV, which in turn allowed them to set a limit that, for a time was the best in the field [85], see Fig. 3.9.

The next phase of the project, the XENON 100 should compete strongly with the WArP 100 l detector.

Argon detectors

An ambitious program is being pursued also in the field of argon detectors. Apart from WArP which will be described with more detail in the next chapter, other experiments are being constructed to take advantage of the benefits offered by liquid argon technology. One notable project is ArDM which is pursuing an extremely ambitious project of setting up a 1 ton two-phase argon detector, where the scintillation light would be registered by photomultipliers, while the ionization will be measured directly via GEM detectors [88]. The ArDM detector, when constructed will no doubt play an important part in the field of direct Dark Matter searches.

The CLEAN collaboration is also pursuing the path of an argon detector, although it will be a single phase detector, where only the scintillation light will be registered. Even so, the detector should be capable of suppressing the electron background thanks to the pulse shape discrimination method described in the next chapter.

3.5 Summary of the current experimental situation

The situation at the time of the writing is still unclear. It is generally agreed that DAMA has observed an annual modulation signal with great precision. It is a matter of dispute, however, whether this is proof of Dark Matter, especially since the DAMA result is as of yet unconfirmed by an independent experiment. The DAMA collaboration refuses to acknowledge the correspondence of second phase experiments to their results, and different experiments searching for the same effect as DAMA - ANAIS [90], NAIAD [91], KIMS [92] are not yet sensitive enough to contradict the DAMA result. There are attempts at accommodating

the seemingly contradicting results of DAMA, CDMS, XENON and others ([69], [70]), but it is becoming increasingly harder, with the larger sensitivity of the null experiments. One thing worth noting is that the possibility of concordance is achieved thanks to a new effect called channeling claimed recently and studied by the DAMA collaboration [93], which suggests that in some crystals the quenching can be suppressed, so the (2-6) keV_{ee} range would become proper keV. In fact, in the recent papers the DAMA collaboration omits this index when publishing their results.

A large problem is that, depending on the halo models, the annual modulation can be strongly suppressed or even have a different phase [94]; this will be described with more detail in Chapter 7.

All in all, it would seem that there is more and more evidence for Dark Matter, but they have yet to converge in one model, or provide indisputable proof. One could say, that the search for the Dark Matter particle is entering its most interesting phase and it seems that the prize is just around the corner.

Chapter 4

The WArP Experiment

The WArP experiment runs in the underground laboratory at Gran Sasso in Italy. The detector is a two-phase, liquid and gaseous, argon detector designed to search for Dark Matter in the form of heavy particles, most probably in the form of WIMPs. The main detector has a volume of 100 liters and is, at the time of writing, being commissioned at Gran Sasso. A large part of this work though, is based on the results of a 2.3 liter prototype detector that has been running since May 2004. Both detectors operate on the same principle, except that the large detector is surrounded by a veto made of 8 tons of liquid argon. In this chapter, the detectors and their principle of operation are presented, followed by a list of all the datasets used in the current work.

4.1 Liquid argon as a medium for Dark Matter detection.

As was discussed earlier the field of cryogenic noble detectors is growing very rapidly. There is a number of qualities of noble gases that make them a very interesting detector material. For instance, their scintillation properties - all gases emit light in the VUV range, at 77 nm, 128 nm and 176 nm for neon, argon and xenon, respectively. They are chemically inert which greatly facilitates their storage, which is important when one has in mind the duration of Dark Matter experiments (for example WArP should run for at least 5 years). There are, however, differences between the liquids, which diversify their strengths and limitations as detector media.

The first thing to take into account when designing a Dark Matter detector are the possible interaction properties. In direct detection experiments, and all noble liquid experiments are such, the energy transfer is governed by two-body kinematics. Through simple considerations one can determine that the maximum

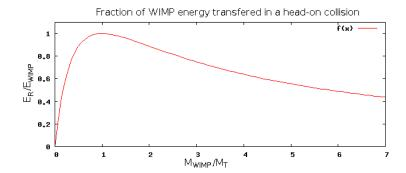


Figure 4.1: The kinetic energy transfer, i.e. fraction of WIMP energy E_{WIMP} transformed into recoil energy E_R as a function of the ratio of the WIMP M_{WIMP} and target atom M_T masses.

energy transfer from WIMP to target particle happens, when their masses are equal or at least close to each other, which can be seen in Fig. 4.1 which presents the energy transfer function:

$$\frac{E_R}{E_{WIMP}} = \frac{4M_{WIMP}/M_T}{(1 + M_{WIMP}/M_T)^2}. (4.1)$$

Where E_R is the recoil energy and E_{WIMP} the incident WIMP energy, M_T is the mass of the target atom. As discussed in the previous chapter, it is expected that the WIMP mass should fall in the region between 50 GeV/c² and few hundred GeV/c², with most predictions pointing to around 100 GeV/c². If this were the case, the first choice for a detector medium would be xenon with a mass around 131 GeV/c². There are, however, other things to take into account. First of all, the actual rate of events observed in a detector depends on the nuclear form factor F(q) [95]:

$$\frac{dR}{dE}|_{observed} \sim F^2(q).$$
 (4.2)

The form factor is a function of the momentum transfer $q = (2M_T E_R)^{1/2}$ and hence of the recoil energy. The thing to note is that the form factor can suppress the interaction rate strongly - a common approximation used is:

$$F(q) = e^{-\alpha(qr_n)^2},\tag{4.3}$$

where r_n is the effective nuclear radius and $\alpha = 1/3$, which is the exact form factor for a Gaussian scatterer, one of the basic models of nuclear density, or $\alpha = 1/5$ which is a better approximation for scalar interactions ([95] and references therein). If this is the case, as it is assumed in Fig. 4.2, then at 50 keV of recoil energy the

events in xenon are highly suppressed, while quite a large fraction still remains in argon. It has been presented by the XENON collaboration that in xenon one can go down with the threshold to 5 keV [85]. Even for a much worse case of a 20 keV threshold with argon, the event rate would still be comparable if not higher. It cannot be excluded that the WIMP is in fact lighter than 100 GeV and in this case argon (and also neon) would gain a lot in detection capability with regard to xenon.

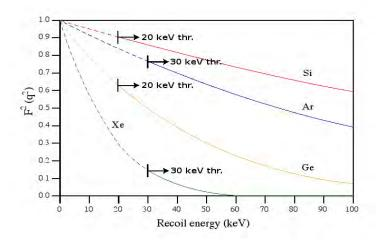


Figure 4.2: Nuclear form factors for silicium, argon, germanium and xenon vs the deposited recoil energy. For each element an arbitrary detection threshold is marked [87].

The next important quality of liquid noble gases is their mechanism of scintillation. The VUV light is emitted by de-exciting dimolecules, i.e. R_2^* . These are created when an excited atom attaches a non-excited one:

$$R^* + R \to R_2^*. \tag{4.4}$$

An alternative situation is when an ionized atom first attaches a non-ionized one, then recombines with a free electron, and then de-excites, as in the following process:

$$R^+ + R \to R_2^+, \tag{4.5}$$

$$R_2^+ + e \to R^{**} + R,$$
 (4.6)
 $R^{**} \to R^*,$ (4.7)

$$R^{**} \to R^*,$$
 (4.7)

$$R^* + R \to R_2^*. \tag{4.8}$$

Excited noble dimolecules come in two different molecular states, singlet - $^{1}\Sigma_{u}^{+}$ and triplet - $^{3}\Sigma_{u}^{+}$. It has been found experimentally [96] that the ratio of these two states depends on the density of the deposited energy, and is therefore different for high Linear Energy Transfer¹ particles, i.e. recoiling nuclei, resulting from WIMP and neutron interactions, and for minimum ionizing particles - genuine electrons and those coming from photon conversions. This can be a powerful background discrimination tool if the detector is capable of determining the time dependence of the scintillation pulses and the half-lives of these molecular states are sufficiently separated. This is the case for both argon and even more so neon - $\tau_1 \simeq 7$ ns, $\tau_3 \simeq 1.2 \ \mu s$ and $\tau_1 \simeq 18.6 \ ns$, $\tau_3 \simeq 15.4 \mu s$, respectively [98]. In the case of xenon the de-excitation times are so close to each other - $\tau_1 \simeq 4.3 \ ns$, $\tau_3 \simeq 22.0 \ ns$ - that it makes it practically impossible to use this property in a real detector.

Another important quality of noble gases is the dependence of the scintillation yields and so the ratio of scintillation to ionization on the Linear Energy Transfer [97]. For minimum ionizing particles, and electrons are such at their almost total paths, the LET is low, and the ionized electrons have a hard time finding an ionized atom to recombine, therefore the recombination times are very long. In addition, if an electric field is applied, these electrons are easily extracted from the interaction region. α -particles and heavier recoiling nuclei that may result from WIMP and neutron interactions have a much higher ionization density and so electrons recombine much easier, and a much larger part of the energy is deposited in scintillation. A more detailed description of this process can be found in [97].

Another thing to take into account when designing an experiment, is the cost of materials. As it turns out argon is the cheapest of the noble gases. All noble gases are obtained as by-products of oxygen or nitrogen liquefaction plants. But since argon is the most abundant - it is about 1% of the Earth's atmosphere, it is the easiest to obtain and purify from contaminations. Other noble gases are obtained as by-products of argon, and since they are less abundant, their cost is higher and purification more difficult. Argon on the other hand can and has been used in large scale physics experiments, the ICARUS experiment [99] being a prime example of a very large vessel (6000 times the volume of the main WArP detector) filled with liquid argon. This would suggest, that if one was to consider building a large detector, on the scale of 1 ton or more, argon would be the most feasible candidate.

There is a caveat, however, in terms of price and it is a result of the presence of the radioactive isotope of 39 Ar in natural argon. The cosmogenically produced isotope is a β -emitter with a half-life of 269 years, the end-point of the β spectrum at 565 keV and a mean energy at 220 keV. This shows that the low energy electrons will have an energy in the range interesting from the point of view of a WIMP

¹Following [97] LET is understood here as average energy loss rate along the particle path.



Figure 4.3: The external dewar of the 100 l WArP detector surrounded by the shielding structure on site in the underground laboratory at Gran Sasso.

search. As mentioned before the WArP experiment has the means to distinguish minimum ionizing particles from the recoil types, but the sheer amount of ³⁹Ar $((1.01 \pm 0.08) \text{ Bg/kg in natural argon } [100])$ can become a problem for larger detectors. For example, in a 100 liter detector, one would expect about 140 Hz of ³⁹Ar events. There are two solutions of this problem - either the background suppression is good enough to exclude the signals coming from the contamination or the detector should use isotopically depleted argon which can be very costly. The WArP collaboration is pursuing both options. As far as isotopic depletion goes there are two possibilities: depletion using centrifuges and using isotopically depleted argon from underground reservoirs. The WArP collaboration has performed test runs using argon depleted on centrifuges in Russia. The contamination level of this sample was measured by the Looslie group in Switzerland and the activity was below instrumental sensitivity, i.e. at most 1/30 of the standard abundance [102]. Preliminary test runs have been performed in preparation for the depleted argon run, but a proper run with the special grade argon has not, as of yet, been performed. Argon from underground reservoirs has been studied as well [103]. Argon obtained by this method is desirable, because ³⁹Ar is produced via cosmic ray interactions, so if the argon were to be shielded from cosmic radiation for a sufficiently long time (thousands of years), a large fraction of the radioactive isotope would decay. It just so happens, that Helium and, as a by-product, argon can be found in underground pockets of methane. In the U.S. the Helium from these pockets is extracted and then stored in the National Helium Reserve in Texas. The WArP collaboration is conducting a research programme to organize an extraction of argon from these reservoirs. First tests have already proven, that argon obtained in this way is at least as good, as a centrifuge depleted sample [103].

4.2 The WArP detector

The WArP 100 l detector, at the time of writing, is being commissioned in the underground laboratory in Gran Sasso, see Fig. 4.3. It is the first double phase, gaseous and liquid, argon detector. The main (inner) detector (see Fig. 4.4) comprises of a 100 l liquid argon phase, observed by 36 Phototubes (6 2" and 31 3") specially constructed to work in liquid argon temperatures - the argon boiling temperature is 86.7 K at atmospheric pressure. The detector is surrounded by a liquid argon veto detector with 300 3" phototubes to minimize the influence of the neutron background. At the bottom of the main detector chamber is the cathode, and above it, each spaced by 1cm in the vertical direction, are the racetracks, separated from the cathode by a voltage divider. Together, they will generate an electric field of 1kV/cm and ensure its uniformity all the way to the liquid-gas interface, 60 cm from the cathode at the bottom. The first of the three grids is just below the surface of the liquid phase and together with the second grid creates a field of 4.4 kV/cm which is sufficient to extract all of the ionization electrons from the liquid into the gaseous phase and accelerate them to ensure secondary scintillation [87]. The field between the second and third grids, usually 1 kV/cm, is set in such a way as to ensure the complete collection of electrons on the third grid. The detector structure is constructed from low-background copper. The walls are covered with a dielectric UV reflector², which in turn is covered with an evaporated layer of (450 - 600) $\mu g/cm^2$ of Tetra-Phenyl-Buthadiene (TPB), which is a wavelength shifter emitting light in the blue region, transmittable by the glass photomultiplier windows. The PMTs³, like the one shown in Fig. 4.5 have their windows covered with a transparent solution of Polyethylene and TPB, to allow blue light to pass and UV light to be shifted to blue. The data is read out from each phototube by an 8bit FPGA ADC board with 1GHz sampling.

 $^{^{2}}$ (VM 2000 TM) manufactured by 3M

³ manufactured by ElectronTubes Ltd, England



Figure 4.4: A schematic view of the WArP 100 liter detector layout. The inner detector, the outer active veto and the passive shielding can be seen [87].

4.3 The 2.3 liter prototype detector

An important part of the work performed by the WArP collaboration are the tests done with the 2.3 liter prototype of the WArP detector, that has been operational in the underground laboratory in Gran Sasso since May 2004. This detector has been used to test most of the solutions used in the 100 liter main detector, but has also performed well enough to provide significant physics results.

The principle of operation is the same as that of the main detector, only the liquid phase has a volume of 2.3 liters, and a height of 8 cm, which corresponds to a total drift time of about 35 μ s from cathode to surface (for comparison, the total drift time in the 100 l detector is $\sim 280~\mu$ s). The chamber was observed by either 4x3" or 7x2" PMTs depending on the setup. The chamber is housed in an external argon bath that provides cooling, and then surrounded by shields of lead and polyethylene. A scheme of the small chamber can be seen in Fig. 4.6.



Figure 4.5: One of the 3" photomultipliers used in the WArP 2.3 liter prototype. The multiplying dynodes are visible on the right, as well as the light collecting window.

The 2.3 l prototype has been used to estimate the abundance of cosmogenically produced ³⁹Ar in commercial grade argon [100] and then to set the first limit on the WIMP parameters by a liquid argon detector [101].

4.4 Electronics in the WArP experiment

The electronics used in the 2.3 liter chamber have evolved with time in order to find the best solution to be used in the 100 l detector. The general scheme, shown in Fig. 4.7 stays pretty much the same, but the details have varied strongly in the course of the measurements. The signal registered by the PMTs is sent to a preamplifier, which can be a standalone board or a part of the next stage element. In the first phases of the 2.3 l chamber measurements the preamplifier also integrated the signal. The difference between non-integrated and integrated waveforms can be seen in Fig. 4.8. If a signal was integrated the preamplifier usually introduced a decay constant, coming from the RC unit present in the filter, into the data. The preamplified signal was then led into a majority trigger board⁴. The trigger and the resulting signals were then sent to a flash ADC board that was connected to the data taking computer. In the first runs, to take the whole signal range into account, the signal was split into two waveforms and both were saved for each

⁴manufactured by CAEN





Figure 4.6: The WArP 2.3 liter detector layout and a picture of the chamber being dismounted.

event and PMT. These were the high-gain and the low-gain waveforms, where the low gain was a version of the raw signal with the amplification smaller by a factor of 10 as compared to the high-gain, saved in order to analyze the events that would otherwise saturate the ADC converter.

In the last runs of the 2.3 liter chamber, namely those in preparation for the ³⁹Ar depleted argon runs, a new setup was used, where the signal was not hardware integrated but went straight to dedicated FPGA boards⁵, which took care of the trigger and the digitization of the data. Boards of this type will also be used in the 100 l detector.

The parameters that changed during different data taking runs, are the majority trigger level, the preamplifier RC decay constant, the ADC sampling time and the ADC range.

During all data taking runs a second data taking line existed, used to calibrate the photomultipliers. Most often it was exclusive, i.e. the data stream, could be plugged to the standard data acquisition (DAQ) or the calibration setup. The calibration line consisted of a preamplifier (with different parameters than the one

⁵manufactured by ACQUIRIS

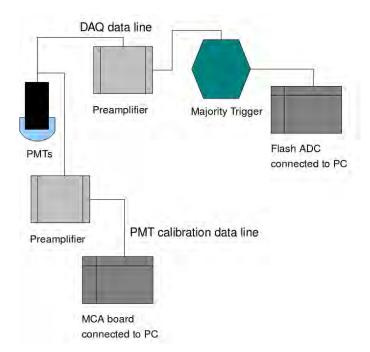


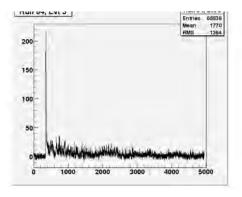
Figure 4.7: The WArP 2.3 liter electronics setup. In the last runs of the chamber, in the DAQ data line the Flash ADC board was replaced by an FPGA board.

used for the DAQ) and then a multichannel board connected to a PC.

4.5 The detection method.

When a particle interacts in the liquid phase, the deposited energy manifests itself as scintillation and ionization with a ratio depending on the LET. The scintillation light is registered by the PMTs in the form of the primary pulse (S1) as in Fig. 4.8, while the electrons coming from ionization are drifted in the electric field up to the surface. There, they are extracted to the gas phase and accelerated to such an extent that secondary scintillation light is emitted and registered by the phototubes as the secondary pulse (S2).

There are two types of events in the WArP detector, those caused by interactions of β and γ particles, which we will call electron-like or gamma-like and those caused by the interactions of neutrons or WIMPS, which we will call neutron-like or recoil-like. All electron-like events (indistinguishable from gamma-like events) are background as are all events caused by neutron interactions.



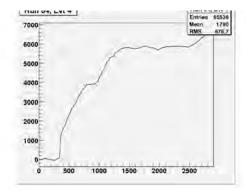


Figure 4.8: The primary signal from the WArP detector. a) A raw form, b) an integrated waveform.

4.5.1 The electron background suppression

As mentioned before, the ratio between scintillation and ionization differs for different particles and this translates into the difference between the ratios of the S1 and S2 signals seen by the PMTs. Typical signals of electron and neutron interactions are presented in Fig 4.9 - top. Since the ratio of the fast and slow component of the primary scintillation light is different for both types of particles, this can be registered by the PMTs as well, as is demonstrated in Fig. 4.9 - bottom. This allows, based on a parameter called F-prompt, that will be defined in the next chapter, to differentiate between the two types of particles. These two separation methods together give a very powerful tool of electron background rejection that has been calculated to be better than 3×10^{-7} [101]. This is sufficient to suppress the background arising from electrons emitted by ³⁹Ar in the 100 liter detector, but puts into question larger argon detectors, unless depleted argon is used.

4.5.2 3-D event localization

The time between the onset of the pulses, is the time that is needed for the electrons to drift to the surface from the point of interaction. Therefore it can be treated as the Z-component in the three dimensional location of the event. The X-Y coordinates will be determined by calculating the centroid of the secondary pulse. So, with a sufficient number of PMTs, a full 3-D event localization will be possible. In the 2.3 liter detector, only a very rough X-Y positioning was possible, and only in the 7 PMT setups. A more precise localization of the events in the small detector is not possible since a signal is made up of single waveforms, each comprising of several to tens of photoelectrons for the primary pulse and hundreds for the secondary pulse. Since most of the light in the chamber is reflected it

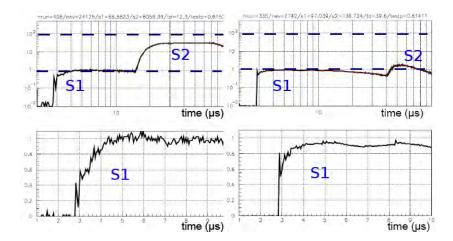


Figure 4.9: The discrimination methods in WArP. Top: Signal to primary pulse ratio for electron (top-left) and neutron (top-right) induced signals. Bottom: Same, but only for the primary pulse for electron (bottom-left) and neutron (bottom-right). The pulse shape discrimination is done based on how fast the primary pulse grows. Note that these are integrated signals, as obtained in the 2.3 liters chamber.

arrives at several PMTS at a time and the X-Y coordinate can be determined only by ascertaining the density of the light in PMTs, and for this analysis a larger number of PMTs is needed.

4.5.3 Neutron background suppression

The background reduction methods described in Section 4.5.1 are intended to diminish the number of events coming from electrons and gammas, which interact mainly with the electron clouds of the detector atoms. Neutron interactions, on the other hand, are indistinguishable from WIMP interactions as far as the S2/S1 ratio and primary pulse shape discrimination methods are concerned, because they have no electric charge and interact with the nuclei. This is why the neutron background is the most dangerous for Dark Matter detection and additional measures must be put in place to eliminate these events. The one quantity that differentiates the neutrons from WIMPs, from the detection point of view, is the interaction cross-section. Since the neutron has a probability of interaction that is 18 orders of magnitude larger than the current WIMP limits from CDMS II [83] ($\sim 10^{-24}$ cm² to $< 10^{-42}$ cm²), it is highly more probable that the neutron will interact more than once in the detector, if the detector is sufficiently large.

In order to fulfill this condition the main WArP detector will be surrounded

by an outer veto detector filled with eight tons of liquid argon viewed by 300 3" photomultipliers. These PMTs will register only the primary scintillation signals, as there is no significant electric field in the outer detector. In these signals a discrimination of gamma and neutron events based solely on the shape of the primary pulse will be implemented. The registered recoil-like events will then serve as a discrimination tool for neutrons in the inner detector. The principle is that a neutron will differentiate itself from WIMPs by interacting more than once.

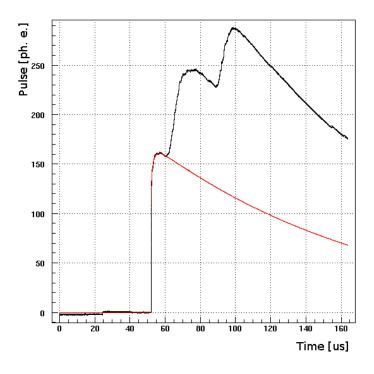


Figure 4.10: A double interaction inside the WArP 2.3 liter chamber. The red line is the average primary signal used in the analysis and which denotes the primary signal. Two secondary pulses are visible. Note that the signal is hardware integrated.

This can be observed in two ways. The first, corresponding to multiple interactions inside the detector volume - an event of this type can be seen in Fig. 4.10. Here the primary signal is a convolution of two or more signals, that are indistinguishable from one another because of the short time a neutron needs to traverse the chamber, while the secondary signals can be discerned if the Z-axis coordinate of the interactions is separated by at least 5 μ s. It is suspected that it will be also possible to separate these signals based on their X-Y positions. A

study of these signals will be presented in Chapter 6.

The second possibility is that the neutron will interact inside the chamber only once. Then, if we consider the elastic cross-section for neutrons in argon, taken from the ENDF database [104] and calculate the mean free path applying the formula:

$$l = \frac{1}{n\sigma} \tag{4.9}$$

where n is the atom number density and σ is the cross-section in cm², one can see in Fig. 4.11 that the mean free path, for energies from 100 keV to 8.5 MeV generally stays below 60 cm which is the smallest possible length of LAr between the inner and outer walls of the veto detector. The energy range used represents neutrons that have an energy high enough to imitate a WIMP signal but with an upper energy bound expected from natural radioactivity in the Gran Sasso laboratory [105]. Inside this energy range there are resonances where the mean free path is indeed longer than 60 cm but they constitute only a fraction of the whole energy spectrum - note the log scale in the X axis. To calculate this fraction, the results can be weighed by the measured fluxes of environmental neutrons, normalized to 1, which were taken from [105]. Two most extreme of the four spectra were used, here called "Gran Sasso 1", which is the spectrum measured for hall A with dry concrete and "Gran Sasso 2" which is in the same conditions but using only fission reactions. The results are presented in Table 4.1. The "Gran Sasso 2" spectrum does not take into account all the possible sources of neutrons, and so weighs more on the lower energy end of the spectrum where the neutron can travel longer - hence the larger percentage of escaping neutrons. Even with this spectrum, however, it can be noted that not more than 4.5% neutrons would survive traveling through the shortest possible path in the detector. For a more realistic spectrum this number is closer to 3.7% and for a flat spectrum 0.9%. Another thing to note is that these numbers are the most conservative estimates of surviving neutrons. In reality even less neutrons should survive since, due to geometrical considerations, only a fraction of the neutrons interacting in the WArP chamber could travel a path as short as 60 cm. Most neutrons will not interact so close to the walls of the inner chamber and will not travel at an angle perpendicular to the wall. For example, the spherical angle where the path would be shorter than 90 cm is only 17% of the total 4π angle. And at 90 cm only 2% of neutrons do not interact. For particles interacting closer to the center of the chamber, this ratio will be even smaller. It must be said though, that it is not feasible to catch all of the neutrons in this way, because even for a veto detector with a minimum width of 120 cm more than 1\% of the neutrons would still escape (in the conservative estimate), while the cost in volume would be eight-fold.

As it has been shown, most neutrons will interact in the veto detector. The scintillation signal, same as a primary in the inner chamber, will be registered

LAr track	Not Weighed	Gran Sasso 1	Gran Sasso 2
60 cm	0.009	0.037	0.045
$90~\mathrm{cm}$	0.0041	0.019	0.023
$120~\mathrm{cm}$	0.0027	0.012	0.015

Table 4.1: Fraction of neutrons traversing 60, 90 or 120 cm in LAr without interaction. Columns are: a flat neutron spectrum, the spectrum measured for hall A in the Gran Sasso laboratory with dry concrete floors, the same but the simulation takes into account fission reactions only.

and a flag sent to the main data acquisition if the signal is identified as a fast (dominated by the 7 ns component of the scintillation light) signal, i.e. a neutron recoil. Events flagged this way will not be taken into account in the WIMP search.

Another source of background are cosmic muons, that can interact with atoms of the detector structure and create neutrons. To minimize this effect, the WArP detector is housed in the underground laboratory in Gran Sasso, where the average depth of 1400 m under the rock is equivalent on average to about 3600 meters of the so called water equivalent.

4.6 Datasets used in the analysis

The WArP 2.3 liter prototype has been taking data since May 2004. Due to technical problems and the realization of the R&D program for the 100 l detector the equipment was modified and data taking has not been a constant process. The data has been divided into datasets. For each set of acquired data, only selected runs are usable for a full fledged analysis. The selected data runs are as follows:

4.6.1 Dark Matter searches datasets

Below are the datasets that will be used throughout the physics analyses reported in the following chapters of this thesis. The wimp_002 and ncal_003 datasets have been used to obtain the first published result of the WArP Dark Matter search [101]. One of the objectives of the other analysis presented in this thesis is to see, whether using the new analysis software created by the author of this thesis, could improve the already published result. The dataset names defined here will be used throughout the further chapters. During these runs the detector operated either with 7x2" or 4x3" PMTs.

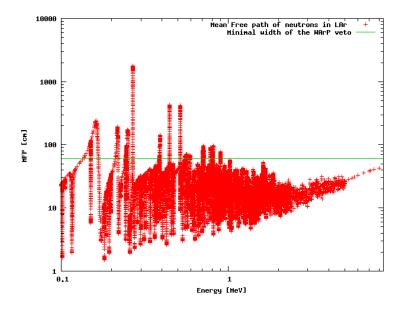


Figure 4.11: The mean free path of neutrons in liquid argon in the energy range between 0.1 and 8.5 MeV. Neutron-argon cross-section data are taken from the ENDF database [104].

wimp_001 and ncal_002

This dataset was the first long data run taken by the WArP collaboration, after closing the 2.3 liter chamber in lead and polyethylene shielding in order to lower the gamma and neutron backgrounds respectively. The chamber was equipped with seven 2" phototubes and the PMT signal was integrated with a Canberra preamplifier with a RC time constant of 40μ s. The sampling time of the electronics was 50 ns. The dataset called wimp_001 is the WIMP search run, starting from run number 991 up to run number 1185. The light yield during this run was estimated to be 0.54 phe/keV. The ncal_002 was a calibration run with neutrons at the beginning of the data taking, and consists of runs 984 up to 990.

wimp_002 and ncal_003

The second long data run taken by the WArP collaboration. The chamber and electronics were the same as for the previous data runs. The wimp_002 dataset starts from run number 2052 up to run number 2358, for a total of 45 live days. The light yield during this run was estimated to be 1.26 phe/keV, due to better coating of the chamber and improved phototubes. The ncal_003 was a neutron calibration from run 2044 up to 2051.

wimp_003, wimp_004, nofield_001 and ncal_006

Before these runs the electronics was upgraded. The signal was integrated by a new dedicated charge preamplifier and read out by a new CAEN board with an ADC with a range of 14bits, which allowed to use only one waveform per event, instead of the old division into high gain and low gain data. The new board also had a sampling of 10ns, which greatly improved the event separation capabilities. The difference between the wimp_003 and wimp_004 datasets is in the trigger constraints, the second set having a more lenient condition. The nofield_001 is a set of data with the extraction field turned off. This kind of data is characterized by a lack of the secondary signal and a larger light yield resulting from the fact that the electrons are not pulled away by the electric field and can recombine more easily. The run numbers for for wimp_003, wimp_004, nofield_001 and ncal_006 datasets are: 3006-3223, 3224-3479, 3230-3236 and 3155-3163, respectively. The number of PMTs was changed to 4 3" phototubes to increase the photocathode coverage.

wimp_005, nofield_002

Prior to these runs the detector chamber was changed. The new chamber was constructed out of low background materials. A new preamplifier was used, this time with an RC decay constant of 120μ s. The nofield_002 was the first test of the new setup, with the extraction fields turned off. It spanned runs 4003-4043. After refurbishing the chamber, because of a leak, and its refilling the wimp_005 set was taken with runs from 4100 to 4306.

4.6.2 Other datasets

This data was taken with a small dedicated chamber with a volume of 0.7 l LAr corresponding to about 1kg of active mass. The chamber was single phase, with no external electric field and was observed by a single 2" phototube mounted on the top of the cell. The steel chamber, encasing the detector, was immersed in a liquid argon bath to keep a stable temperature. A detailed description of the chamber can be found in [106]. All of the datasets mentioned below have been taken above ground in the so called Mounting Hall of the Gran Sasso laboratories.

Neutron quenching

The electronics from the 2.3 liter prototype was used to determine the neutron quenching factor in liquid argon. The data was collected using radioactive cesium and americium-beryllium sources. Since they were taken with the same electronics

as for the 2.3 liter detector the run numbers follow the same pattern and start from run 5001 to 5157.

Liquid Argon contamination with nitrogen and oxygen

The setup used different electronics, mainly the FPGA ACQUIRIS board, and no preamplifier. There were two dedicated runs, one for argon contaminated with nitrogen and one with oxygen. The numbers of these runs start with 1 and are correlated to the number of ppm of contaminant used.

Pulse shape discrimination data

The data was taken with the same electronic setup as the N_2 and O_2 contamination data. It is a series of runs with an americium-beryllium source spanning numbers 1-37.

Chapter 5

Research and Development in the WArP Experiment

This chapter aims to present some of the work done by the author of this thesis on the various elements of the WArP research and development program as well as some of his contributions to the data analysis. The work on the calibration of the photomultipliers will be presented, both for routine calibrations during the data taking of the 2.3 liter chamber as well as the input into the tests of the PMTs for the 100 liter detector. Later, the work on testing the effects of nitrogen and oxygen contamination on the light yield of liquid argon will be described as well as a study of pulse-shape discrimination methods. Last, a preliminary measurement of the neutron quenching factor will be discussed.

It must be noted that the activities presented here are only a cut out of the whole WArP R&D program, which included a broad spectrum of tests on the hardware, software and liquid argon itself. Presenting this entire program is by far beyond the scope of this thesis, but one should keep in mind, that the activities presented here are a part of a larger research that ultimately led to the construction and commissioning of the WArP 100 l detector.

5.1 Single electron response calibration

As mentioned before, the WArP experiment uses photomultipliers to register the scintillation light. Photomultipliers are a delicate tool, that is able to register single photons. The PMTs used in the WArP detectors are specially designed to function in liquid argon temperatures. Their general principle of operation is quite simple: a signal photon hits the PMT window and, if it deposits enough energy, expels secondary photoelectrons from the bi-alkaline cathode. These photoelectrons are then accelerated in an electric field and hit consecutive dynodes where

each electron generates several new electrons. The swarm of electrons from the last dynode hits the anode and generates a voltage pulse that is then sent to the electronic readout.

Due to the statistical nature of this process it is very important to understand what is the correspondence between the voltage pulse registered by the acquisition system and a single photon arriving at the photocathode. Having this knowledge one can calibrate the data acquisition system and rescale all the event signals from ADC counts to photons or photoelectrons (since the two values correspond closely in the case of the WArP detector). This is needed, since photons are the actual physical quantity that is registered. This aspect becomes even more important, when one considers the fact that background separation in the WArP experiment depends heavily on the properties of light registered by the PMTs, and so the knowledge of the number of photons arriving at the cathode and their time of arrival is crucial in the analysis.

5.1.1 The Single Electron Response (SER)

The most important characteristic of a photomultiplier is its response to a single photon. This is usually determined by using a source of light with an intensity so low, that one can be sure that only single photons arrive at the photocathode. This is called the Single Electron Spectrum or SER. During the tests done by the WArP collaboration, we have seen, that a photomultiplier looking over a dark chamber with liquid argon, has practically the same spectrum as that induced by a low light source [107]. This is caused by thermionic noise inside the phototubes themselves, where electrons are expelled from the cathode due to thermal fluctuations. Therefore it was possible to perform most calibrations without using a dedicated light source.

When examining the SER, noise from two sources is always present. One is the electronics noise, and the second is the inherent quality of the phototube itself, which is the so-called dynodic noise, both of which manifest themselves as exponential distributions. A typical SER spectrum can be seen in Fig. 5.1, one can clearly distinguish the dynodic/electronic exponential part and the SER peak.

There have been some approaches to calibrating the Single Electron Response signals from phototubes. We have chosen, based on previous experience of the WArP collaboration [107], to use a phenomenological approach and fit the SER peak with consecutive Gaussian functions:

$$f(x) = \sum_{n=1}^{n=2} B_n \exp(-x/T_n) + \sum_{m=1}^{m=k} a_m \exp\left(\frac{(x - mx_o)^2}{(\sqrt{m}\sigma)^2}\right),$$
 (5.1)

where the two exponential functions account for the electronic and dynodic

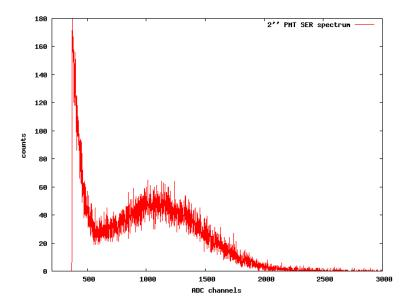


Figure 5.1: A typical SER spectrum, the dynodic and electronics noise, photoelectron peak and the so-called valley that separates them, are clearly visible. The signal was passed through a hardware discriminator, hence the threshold at 370 ADC counts.

noise components. x_o is the position of the first photoelectron peak. For subsequent peaks, corresponding to two, three or m photoelectrons exiting from the cathode the position is a multiple of the first photoelectron peak $x_m = (mx_o)$, while the dispersion grows with the square root of the peak number $\sigma_m = \sqrt{m}\sigma$. In the actual calibration it was rarely needed to fit peaks beyond the second one. Another approach was used by the Borexino experiment [108], where the signal was described also by exponential and Gaussian functions, but the electronics noise was convolved with the dynodic noise (the noise function has a negligible effect on the Gaussian component). The resulting noise function is also much more complicated than in our case.

5.1.2 The 2.3 liter prototype ongoing calibration

In order to calibrate the photomultipliers, during the data taking with the old electronics (up to wimp_005), the SERs were taken with a dedicated Multichannel Analyzer (MAESTRO MCA board)¹. The signal going into the board was integrated by a preamplifier. The SER were taken every day - after stopping the data

¹manufactured by ORTEC

acquisition and just before restarting it after performing the daily detector maintenance procedure. To use the SER acquired in this way, two things were needed, the conversion factor between the MCA board and the standard data acquisition electronics, and an association between the SER files and run numbers so that the proper SER positions would be applied to the corresponding runs. The conversion factor was obtained via an intercalibration of the DAQ system. A square wave with set values of the amplitude was sent to both the MCA board and the standard data acquisition electronics. The resulting peaks were located and by a method of two linear fits the conversion factor was calculated. The SER-run association, on the other hand, was achieved by means of a MySQL database, that was created by the author specifically for this purpose, but has been steadily growing since, and is now an inherent part of the WArP data taking process.

The fitting of the SERs was performed using a software that was developed and updated by the author throughout the 2.3 liter chamber runs. The software used Eq. (5.1) for the fits of the PMT spectra. The results, specifically the parameters of the single photoelectron peak - position, dispersion and height were saved in the MySQL database, from where they could be later retrieved by the main analysis software described in Chapter 6. The code operated in graphical and batch modes, although the batch mode turned out to be moderately unstable, and so all fits were checked visually. The peak position was used by all of the analysis software, and together with the intercalibration coefficient served to calculate the ADC/photoelectron conversion for each run. Figure 5.2 presents the graphical window of the SER fitting program used in the calibration. In Fig. 5.3 the time dependence of the SER position of six PMTs throughout the wimp_002 data run is presented. Note, that during this run, the voltage supplied to the PMTs was adjusted, so that the SER would remain in the same position, and so effects like the decrease of gain² during prolonged PMT operation are not visible.

5.1.3 Photomultiplier tests for the 100 l detector.

The SER fitting method was also used in the PMT Testing Facility in Naples, where all the phototubes to be used in the WArP 100 l detector were thoroughly tested. I have designed, and together with Biagio Rossi, coded the whole software system used for these tests. The setup consisted of a Graphical User Interface front panel, shown in Fig. 5.4 connected to a dedicated MySQL database and an analysis tool, capable of analyzing multiple phototube spectra in parallel. In the first phase of the tests an MCA was used and the parallel capability was not utilized, since the MCA board could only acquire one spectrum at a time.

²In a PMT, the gain is the number of electrons arriving at the anode of the PMT and signifies the PMT's signal amplification capability.

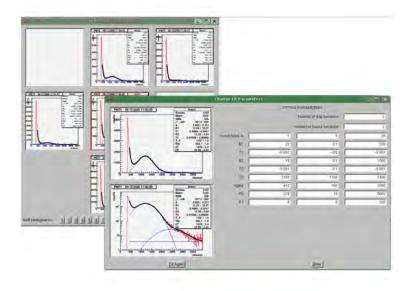


Figure 5.2: The SER fitting program used for the ongoing calibration of the WArP chamber. The main window is shown as well as the auxiliary window used to fit single PMTs if the fit with the standard parameters did not converge.

During a later phase, two QDC (Charge Digital Converter) boards were used that allowed a measurement of up to 18 phototubes contemporaneously. I have created a new GUI panel for this setup, and upgraded B. Rossi's DAQ code to work with the new setup. The new User Interface is presented in Fig.5.5. The data analysis was conducted with an adapted version of the software used for the routine calibrations of the 2.3 l chamber. The results of these tests were stored in a database created by the author, and then further developed by the collaborators in Naples.

For the tests, a special frame constructed from teflon, allowing the simultaneous immersion of 18 PMTs was placed in a dedicated dewar filled with liquid nitrogen. Special light-guide tubes, connected to a blue light pulser³, were inserted inside of the dewar and placed in such a manner, that all PMTs were illuminated in a uniform manner. The chamber was completely shielded from external light and so the only light that reached the PMTs came from the light pulser or from the dark counts inside the phototubes.

For each batch of 18 PMTs a series of tests was conducted. These involved measuring the properties of the photomultipliers at room temperature and in cryogenic

³manufactured by HAMAMATSU

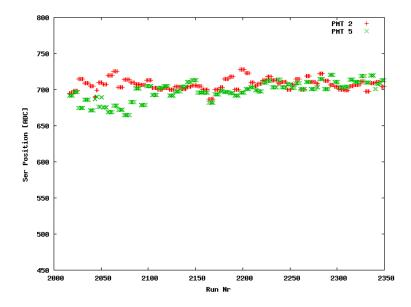


Figure 5.3: The SER peak positions for runs 2010 to 2350, the values shown are an average of the SER acquired before and after the data acquisition. Each data acquisition period consisted of a few runs.

conditions. For each PMT a series of SER spectra was then taken and analyzed. A series of parameters was obtained from each spectrum taken and saved in the database. The parameters saved were the peak position or gain, the peak to valley ratio (ratio between the amplitude of the pulse at the peak, and the amplitude at the lowest point of the spectrum between the peak and the exponential noise part) and the sigma to peak ratio (Gaussian dispersion to peak amplitude ratio). A stability measurement for one of the PMTs can be seen in Fig. 5.6 where these parameters are shown as a function of time for run number 5175 (unrelated to datasets defined in Section 4.6.2). In Fig. 5.7 the distributions of the sigma to peak, the peak to valley and the relative difference of the gain of the PMT measured in cryogenic conditions (cold) and in room temperature conditions (hot) are shown for over 300 PMTs tested in the Counting Test Facility in Naples during its running.

The software system was also used for gain stability measurements in cold and hot regimes as illustrated in Fig. 5.8 (top) where the red points are the gain as a function of voltage applied to the PMT, the blue points are the same dependence only at liquid nitrogen temperature. The lines are plotted to guide the eye. Another series of tests, that was tried but not completed because of a lack of time, were the attempts to see the effect of larger quantities of light on the phototube. The software system proved to be fully ready for these tests,

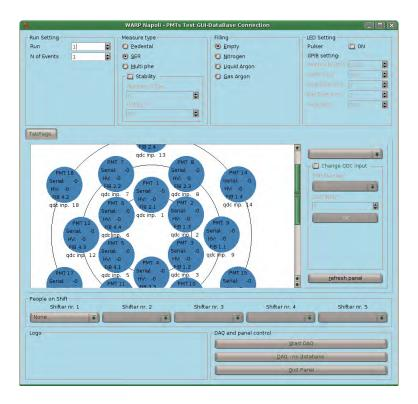


Figure 5.4: The front panel of the initial Graphical User Interface for the tests of the PMTs in Naples. Work done together with B. Rossi.

which can be observed in Fig. 5.8 (bottom) where a spectrum with the first, second and third photoelectron peaks is fitted. The code was capable of fitting up to eight photoelectrons separately, at which point it became prudent to fit a Gaussian function, since, due to statistics, the sum of the multiple photoelectron peaks converged into a single Gaussian.

5.2 The effect of nitrogen and oxygen contamination on the light yield of liquid argon

During the course of the 2.3 liter chamber measurements it has been found that the average signals used in the analysis differ substantially from dataset to dataset. This has been linked to the problem of purity in the chamber, as it was later found the possible culprit being nitrogen or oxygen contamination. An example of this difference can be seen in Fig. 5.9, where the average electron-like and neutron-like signals extracted from runs in wimp_002 and wimp_003 datasets



Figure 5.5: The second version of the GUI panel for the tests of the PMTs in Naples. This version allowed multiple PMTs to be saved simultaneously and provided an interface to the database allowing the quick retrieval of the needed PMT parameters.

are shown. It is clear that in one case the signal is much faster, i.e. has less light coming from the slow component. This is because the process in which the argon dimolecules can be deexcited by a collision with a nitrogen or oxygen molecule is relatively slow, so it will affect mainly the slow decaying argon dimers, since the fast component molecules will all scintillate before they have a chance to interact with the impurities. In the case of Fig. 5.9 nitrogen contamination was suspected. To confirm this hypothesis a dedicated test run was performed to examine this possibility. A second run, testing the effects of oxygen contamination was also performed.

A dedicated setup was operated in the external facility of the Gran Sasso laboratory, the so-called Mounting hall. The setup consisted of a 0.7 liter small LAr chamber observed by a single 2" phototube. The data acquisition was based on a LabView program, while the early analysis was done by means of a C++ program, that I wrote. Controlled quantities of contaminant were inserted into the chamber using a fixed volume cavity in the argon supply pipeline, that was filled with N_2 or O_2 at a calculated pressure. To ensure good mixing, the chamber was then flushed with gaseous argon. For each quantity of contaminant, starting

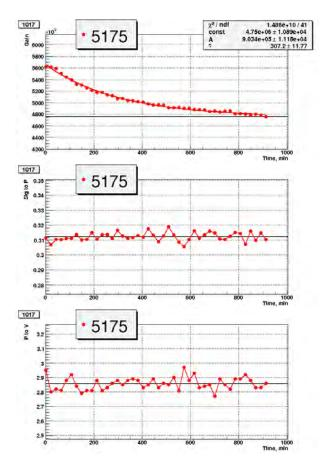


Figure 5.6: Stability plots for PMT number 1017 and run number 5175. The plots show the decrease of the gain with time, and the stability of the sigma to peak position ratio and of the peak to valley ratio [109].

with zero ppm (parts per million), several spectra were taken - mainly while the chamber was exposed to radioactive $^{60}\text{Co}^4$ and $^{137}\text{Cs}^5$. The data was acquired using a 1 GHz sampled fast ADC board, like the ones used in the 100 l detector. For each run single waveforms with a length of 10 μ s were saved; usually 100 000 single waveforms per run. Before and after each source spectrum the SER was taken using an MCA board for calibration purposes - a procedure entirely similar to the ongoing calibration of 2.3 liter chamber. The MCA was also used to acquire Compton spectra of the sources to cross check the functioning of the ADC board.

 $^{^4}$ A β emitter that apart from the low energy electron emits two energetic photons with energies of 1173 and 1333 keV.

 $^{^5}$ A β emitter that apart from the low energy electron emits a photon with an energy of 662 keV.

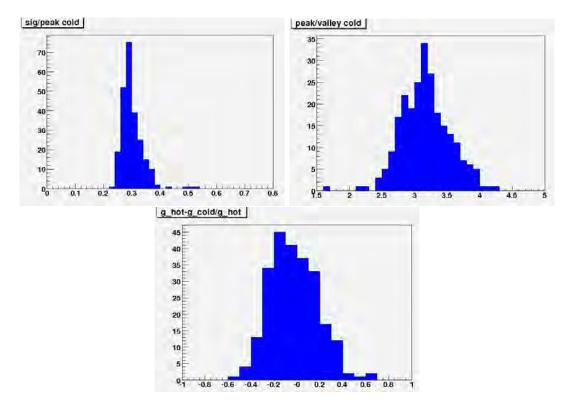


Figure 5.7: The distributions resulting from the tests of over 300 phototubes during the operation of the PMT Counting Test Facility in Naples. The parameters are the sigma to peak ratio (top left), the peak to valley ratio (top right) and the relative difference between of PMT gains operating in hot and cold conditions (bottom) [109].

After each set of measurements the amount of contaminant was raised and the measurements repeated. The setup is described with more detail in [106].

5.2.1 The light quenching effect

One of the effects observed due to the contamination was a partial loss of the scintillation light emitted by liquid argon, which, for example, meant that the number of photoelectrons at which the Compton edges and photoelectron peaks of the source spectra were observed became smaller. This is demonstrated in Fig. 5.10 for ⁶⁰Co spectra and different levels of nitrogen contamination. To quantify the value of the quenching factor a dedicated Monte Carlo simulation was constructed where the 0 ppm contamination spectrum served as the standard distribution from which random numbers were generated and then fitted to higher contamination

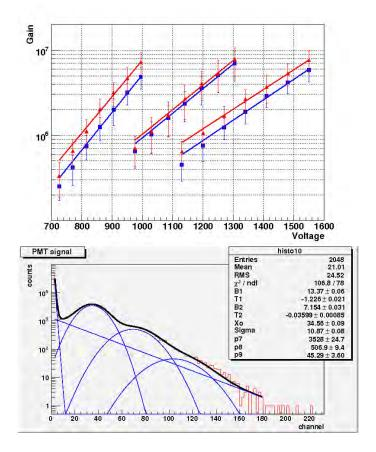


Figure 5.8: Further results of the measurements performed in the CTF in Naples. The linear rise of the gain with voltage applied to the phototube in cold and hot conditions (top) and the capability to fit spectra coming from more than one photon arriving at the cathode (bottom) [109].

spectra, but multiplied by a number smaller than one - the quenching factor. This analysis gave very good results, but was time consuming.

I have developed an alternative method of analysis, that is much simpler and quicker and was based on determining the position of the peak in the Compton spectrum. For each contamination level the spectra were normalized to photoelectrons using the corresponding SER spectra. The same was done for blank spectra, which were then subtracted from the signal. The resulting spectra were fitted with a phenomenological function:

$$f(x) = \begin{cases} ax + b, & x < x_0 \\ N \exp(-(x - x_p)^2 / \sigma^2), & x \ge x_0, \end{cases}$$
 (5.2)

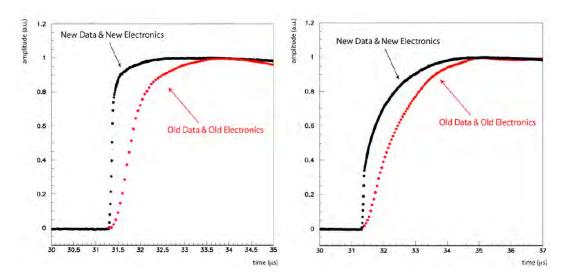


Figure 5.9: Average primary signals for neutron (left) and electron (right) type interactions for wimp_002 (red points) and wimp_003 (black points) datasets [110].

where x_p is the Compton edge position and x_0, a, b, N and σ are parameters of the fit. There is constraint on the parameters, such that $f(x_0)$ is continuous. A sample fit as well as the Compton and blank spectra are shown in Fig. 5.11. The fits were satisfactory up to 100 ppm of nitrogen contamination and reproduced the results of the full fledged analysis perfectly, as can be seen in Fig. 5.12 where the two analyses are plotted for the nitrogen contamination runs (the fit analysis is marked by the green triangles).

5.2.2 The τ_{long} quenching effect

The second effect of the N₂ and O₂ contaminations, which, as mentioned before, prompted the dedicated measurements in the first place, was the quenching of the light from the slow component of argon scintillation. To check the effect of the contaminants on the decay times of the short and long-lived components an average waveform was constructed for each run by first applying cuts to exclude saturated and noise events and then by summing up the remaining single waveforms. This was done by a pre-analysis code developed by the author. The resulting waveforms were not in fact pure argon light signals. There was an intrinsic detector component which was convoluted in the signal. Therefore to access the true signal a deconvolution procedure was used, where the detector response was obtained by creating an average single photoelectron waveform, as in Fig. 5.13, and then subtracting from the average waveform in the frequency domain,

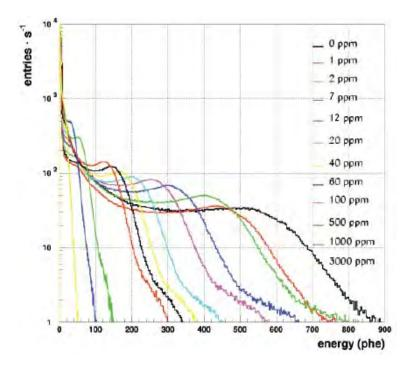


Figure 5.10: ⁶⁰Co spectra measured with different quantities of gaseous nitrogen injected into the test chamber. Only the Compton edge is visible in most cases, the full absorption peak is not very pronounced [106].

accessible via Fast Fourier Transform. The resulting true-signal waveforms were the ones used for the life-time analysis.

The attenuation of life-time, mainly of the long component, was observed both in the case of nitrogen and oxygen. The effect was much stronger in the second case. A possible explanation of this effect is that the scintillating dimolecules of argon can transfer their energy to nitrogen and oxygen molecules instead of emitting scintillation light. Since the longer the time passes, the larger the probability of encountering a contaminant molecule it is sensible that the long component (τ_{long}) would be affected more than the fast one.

Oxygen contamination

Oxygen contamination is very dangerous for ionization measuring experiments, since oxygen is electronegative and can attach the drifting electrons that would otherwise end up as the secondary pulse in the WArP chamber. This means that if the argon is contaminated with oxygen the secondary pulse will be suppressed more, the further the interaction is from the surface, since the electrons have a

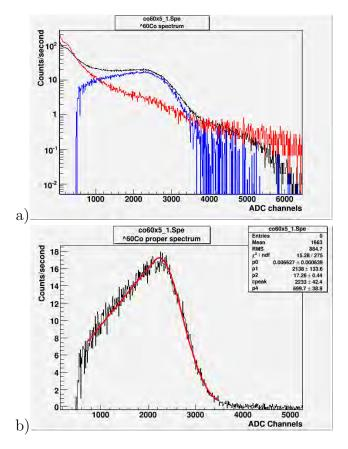


Figure 5.11: a) A 60 Co Compton spectrum at a contamination of 1 ppm of N_2 (black), a blank spectrum at the same contamination (red) and their difference (blue). b) The result of fitting the difference with the function (5.2).

larger path to travel and interact with the impurities. Thanks to this effect it was possible to determine the O_2 contamination in the 2.3 liter chamber and to add some of the data from the WArP 2.3 liter chamber (runs 4101-4140) to the analysis of the O_2 contamination in the dedicated chamber [111].

The part of the analysis using the 2.3 liter chamber was devised and executed by the author of this thesis. The first runs after an argon refill were chosen, so that the oxygen would not yet be trapped by the Oxysorb filter mounted in the chamber. Special data cuts were applied to the WArP chamber data to select events coming from β and γ particles (high S2/S1 ratio), with an energy between 100 and 200 photoelectrons (signals well above the noise region). The main cut used was the drift time between the primary and secondary pulses. Only events with a drift time longer than 20 μ s were selected, so that photons coming from the secondary pulse would not affect the part of the waveform corresponding to the primary pulse.

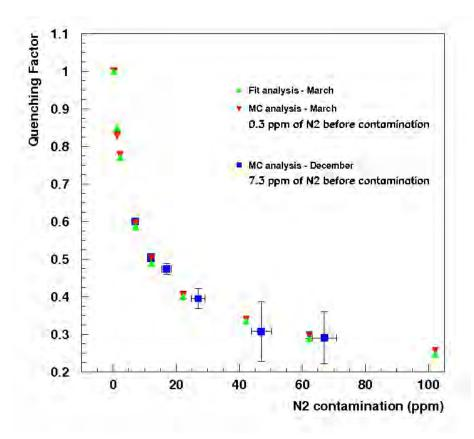


Figure 5.12: The results of the quenching factor analysis for nitrogen contamination; the data points are red and blue for the MC method and green for the fit procedure.

The cuts turned out to be stringent, but for each run of 100 000 events at least 100 events were selected and analyzed. The preamplifier response (decay constant of 120 μ s) was then deconvoluted and the resulting waveforms were added, like in the dedicated chamber runs. The resulting waveforms were very similar, as can be seen in Fig. 5.14 where the two average waveforms are overlaid, proving a good understanding and the correspondence of the data samples.

The level of oxygen contamination for each run was determined by calculating the average S2/S1 amplitude ratio with respect to the drift time. Since the O_2 contamination eats up drifting electrons, then electron swarms traveling a longer distance (i.e. those with a longer drift time) will be depleted more. So for each run the average S2/S1 amplitude with respect to the drift time was fitted with an exponential function to determine the electron lifetime τ_e . This quantity is translatable into the amount of electronegative impurities in liquid argon using

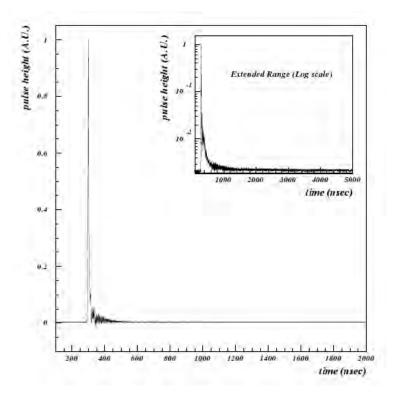


Figure 5.13: The average single electron waveform obtained from the dedicated chamber runs. In the inlay the signal is in log scale, and a longer component attributed to detector response is visible [106].

the following expression:

$$\frac{1}{\tau_e} = k_e[O_2] \tag{5.3}$$

where the rate constant $k_e = 1.9 \ \mu s^{-1} ppm^{-1}$ at 1 kV/cm electric field is taken from Ref. [112]. Because of the continuous purification of the 2.3 l chamber with an Oxysorb filter, the O_2 contamination level went down with time. At first the change was linear, then a saturation effect was observed, as can be seen in Fig. 5.15. This dependence allowed to determine the starting contamination of the argon used to fill the chamber to be 0.02 ppm. This value is smaller than the specifications of the 6.0 grade $argon^6$ used in both measurements, which is expected, since the argon entering the chamber passed through an Oxysorb filter. The filter should lower the amount of oxygen by two orders of magnitude to 0.002 ppm. The observed extra quantities of oxygen in the chamber are assumed to come from the outgassing of the detector parts.

⁶delivered by RIVOIRA ltd.

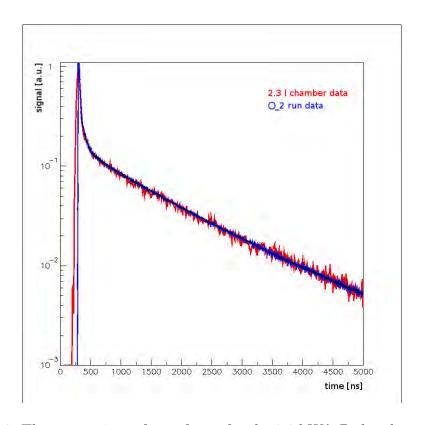


Figure 5.14: The comparison of waveforms for the 2.3 l WArP chamber data (red), and the dedicated chamber runs (blue). The difference at the beginning of the signal is probably caused by the 10 times worse sampling in the 2.3 l chamber electronics.

For the 2.3 liter chamber the SER deconvolution technique applied to the data taken with the dedicated chamber could not be used, since this data was acquired with different electronics and it was not possible to extract a single photoelectron waveform. However, it has been observed, that for the dedicated chamber waveforms the values of the decay-time for the short and long-lived components can be well reproduced if the raw signal is fitted with an extra fourth, very slow exponential component (instead of the deconvolution method). The fourth component has been observed in the 2.3 l chamber data and its decay time - τ_4 has been estimated at 3.097 μ s, which could be attributed to events in the gas phase. The τ_{long} resulting from these fits has been plotted against the contamination in Fig. 5.16 (blue triangles) together with the data from the dedicated chamber. It can be noted that for the 2.3 l chamber data the change in the scintillation time is very small and the quenching effects start at larger contamination values. The

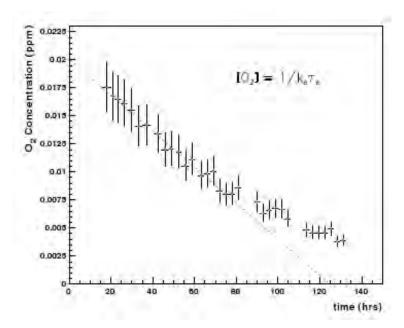


Figure 5.15: The changing of the oxygen contamination in the WArP 2.3 liter chamber with time [111].

data was fitted, using the following relation:

$$\frac{1}{\tau'_{long}} = \frac{1}{\tau_{long}} + k[O_2], \tag{5.4}$$

however as can be seen in Fig. 5.16, the data diverged from the model (green line) at higher contaminations and could be reproduced only if a type of saturation effect was introduced (red line). Using this improved model the light quenching constant for oxygen was found to be at $k[O_2] = (0.54 \pm 0.03) \text{ ppm}^{-1} \mu \text{s}^{-1}$. In general, the data obtained with the WArP 2.3 l chamber shows that the O_2 contamination levels found in commercial grade argon have little effect on the τ_{long} component, but are observable in the loss of ionization, which is a much better measurement of purity at lower contaminations.

Nitrogen contamination

For the measurement of the effect of nitrogen on the decay time of the long component, the 2.3 liter chamber runs could not be used, since it was impossible to gauge the quantity of N_2 in the runs. Hence, only the dedicated chamber runs were used. The light quenching constant for nitrogen was found to be at $k[N_2] = (0.11 \pm 0.01)$ ppm⁻¹ μ s⁻¹, much smaller than the one measured for oxygen, consistent with

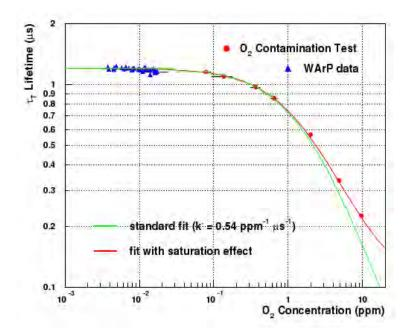


Figure 5.16: The change of τ_{long} due to contamination with oxygen. Blue triangles are WArP 2.3 l data, red circles are dedicated chamber data [111].

previous measurements [113]. An attenuation of lifetime was observed for both the τ_{long} and τ_{short} , with the strongest effect being for the long component.

During the course of the measurements a third, intermediate component was observed, its life time being around (30-40) ns. Its origin is supposed to be instrumental and it is currently under further investigation. The overall change of the lifetime with contamination can be seen in Fig. 5.17, where all 3 components are plotted in log-log scale. It is evident that the effect is strongest for the slow component, and affects the other two in a much weaker manner.

Knowing the quenching constant $k[N_2]$ it is possible to estimate the decay time of the long component in pure, non-contaminated, argon. For this, the contamination level of the commercial argon had to be estimated. This was done, by performing an overall fit for all contamination levels and extrapolating the functional dependence to 0 ppm. With this method the initial contamination was found to be (0.40 ± 0.20) ppm, well in accordance with the specifications of the industrial argon used. Using this result, the decay time of the long component at 0 ppm was estimated, by extrapolating the aforementioned functional dependence, to be (1260 ± 10) ns i.e. significantly lower than the most known measurements [96].

To double check our results I have simulated a single photon-counting technique

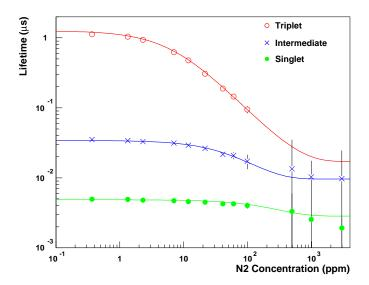


Figure 5.17: The change of τ_{long} (empty circles), τ_{inter} (crosses) and τ_{short} (filled circles) due to contamination with nitrogen. The decrease is strongest in the 3rd, longest component [106].

to imitate that, used in [96], where a very clever detector was set up. In that work, the chamber is watched by two PMTs. The first PMT acted as a trigger, registering the first burst of light, and started a timer. The second PMT was behind a light guide, which allowed only single photons to arrive at the PMT window. When such a photon arrived, the timer was stopped. Actually, the second PMT was opened only after a certain offset time, to avoid counting the beginning of the pulse where multiple photons coming from the fast component could arrive simultaneously at the window. The times obtained in this manner were added which resulted in the average waveform used for the analysis. In our case, the chamber operated with a single PMT, so the single photon technique had to be simulated using software methods. For each waveform a single photon finding algorithm was used, and each found photon peak was replaced with a single bin equal to one. In this way the single photons were counted and all noise signals lower than single photoelectrons were eliminated. in other words, only the clean signal remained. The effect of this analysis can be seen in Fig. 5.18, where the normal average waveform is compared to a waveform created from summing up the single photoelectron waveforms. The delay in the start of the simulated single photon pulse is caused by having to cut out the first $0.5\mu s$ of each waveform to avoid counting multiple photon signals,

which are abundant at the beginning of the signal. It is plain that both curves are parallel and the results of the fit used to obtain the decay time of the long component were consistent with the standard method used.

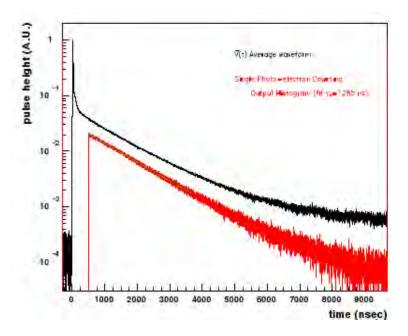


Figure 5.18: A comparison of a standard average waveform (black), with a simulated single photon counting waveform (red). The red waveform starts at 500ns after the onset of the pulse to avoid counting multiple photons [106].

5.3 Pulse shape discrimination methods.

As has been mentioned before, the pulse shape discrimination technique is one of the foundations on which the WArP experiment is based. It is known, that pulses coming from argon-recoil events (from WIMP and neutron interactions), that we will call neutron-like, and electron-recoil events (from β and γ interactions), that we will call electron-like or gamma-like, have different ratios of the fast and slow light components. However, when looking at the data, we cannot say if a given photon came from a fast or slow decaying dimolecule, therefore a method of quantifying the pulse shape must be found. In principle it is possible to fit a signal with average pure neutron-like and gamma-like signals, and extract the value of one of the amplitudes as the pulse shape parameter. This method is rather slow, and even though it may be acceptable in the case of the 2.3 l chamber data, it will definitely not work for the much larger data stream that will come

from the 100 l detector because of the toll it would take on the computing time. Hence, a different, simpler method must be found that will not use too much CPU, and yet provide sufficient background suppression. The purpose of this section is to show a study of different pulse shape classification schemes.

The data used in this study comes from a dedicated run with the 0.7 liter chamber used in the N_2 and O_2 contamination tests. This time, the argon was kept pure, and the chamber was illuminated with an Am-Be⁷ source to provide neutrons. The chamber was viewed with a single 2" phototube optimized for the neutron source spectrum.

The analysis was performed in an analogous way to the N_2 , O_2 contamination measurements. For each run all events were examined by the preanalysis code and spurious events were discarded. For the remaining events, different pulse shape parameters were calculated. The events were divided into energy slices. The full energy range used in this study is from 13 to 240 phe, however at low energies it is difficult to separate the electron-like and neutron-like populations because of the small number of photons while at large energies neutrons are scarce.

The pulse shape discrimination methods studied were the following:

- Q_{del}/Q_{tot} ratio of slow component to total signal.
- Q_{fast}/Q_{tot} ratio of fast component to total signal.
- $(Q_{fast} Q_{del})/(Q_{fast} + Q_{del})$ normalized difference between fast and slow components.
- local Gatti method linear filter method, energy dependent.
- total Gatti method linear filter method, energy independent.
- F-prompt parameter used in the 2.3 liter chamber, explanation is given in text below.

The Q_{del} and Q_{fast} parameters are the integrals of the pulse calculated after and before, respectively, a certain time called T_{calc} . This time signifies the separation of the fast part of the pulse from the slow one. The value of this parameter was obtained by taking the integrals of the average neutron-like and gamma-like pulses and checking where their difference is the largest. This lead to the value of $T_{calc} = 140$ ns used in this study. Q_{tot} is the total integral of the pulse ending at 5 μ s after the onset of the pulse. The parameters are pictured in Fig. 5.19.

The F-prompt parameter is the pulse shape parameter used in the analysis of the 2.3 liter chamber runs. It is the ratio of the signal at T_{calc} to the amplitude

⁷ A neutron emitting source, that gives neutrons up to energies of 8MeV. The decay of 241 Am also provides γ 's with an endpoint at 4.43 MeV.

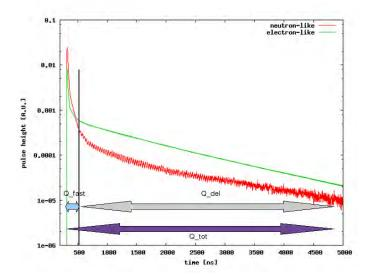


Figure 5.19: Average normalized gamma-like (green) and neutron-like (red) pulses, with the Q_{del} , Q_{fast} and Q_{tot} marked.

of the signal. Since the signals in the WArP prototype detector were hardware integrated, this roughly corresponds to Q_{fast}/Q_{tot} , but in the analysis of the 2.3 liter chamber the F-prompt value was actually an average of a few data points around T_{calc} . This is repeated here, i.e. F-prompt is an average of 45 channels around T_{calc} .

The Gatti method, described in [114, 115] is still another method used to discriminate between two types of pulses, α and β . To use it, ideal average pulses $\bar{\alpha}(t)$ and $\bar{\beta}(t)$ for each type must be known. Then, for any given pulse, it can be divided into short time intervals δt_i and the values of the examined signal at these intervals are S_i . The Gatti parameter is then calculated as:

$$\sum_{i} P_i S_i, \tag{5.5}$$

where the weights P_i are calculated in the following way:

$$P_i = \frac{(\bar{\alpha}_i - \bar{\beta}_i)}{(\bar{\alpha}_i + \bar{\beta}_i)}.$$
 (5.6)

Let us repeat, that to use the Gatti method, ideal signals must be known so, in principle, a dataset must first be analyzed using one of the other pulse-shape discrimination methods, to create the average pulses for neutron-like and gamma-like events. The average pulses can be created for the whole sample of events as

well as for each energy slice used in the analysis. Both of these approaches have been tested, and they are called the total Gatti method and local Gatti method in the list above.

The result of the analysis, after binning all the events together was a histogram with two peaks (one for neutron-like and one for gamma-like events) for each energy slice. An example of such peaks for the energy range of (63-75) phe can be seen in Fig. 5.20. The separation of these peaks was to be calculated using the following parameter [116]:

$$S = \left| \frac{X_n - X_e}{\sigma_n + \sigma_e} \right|,\tag{5.7}$$

where X_n, X_e are the positions of the peaks and σ_n, σ_e are their variances. The larger the S parameter the better the separation. To calculate it, Gaussian functions should be fitted to each peak and the parameters obtained from the fit could then be used to calculate the measure of separation S.

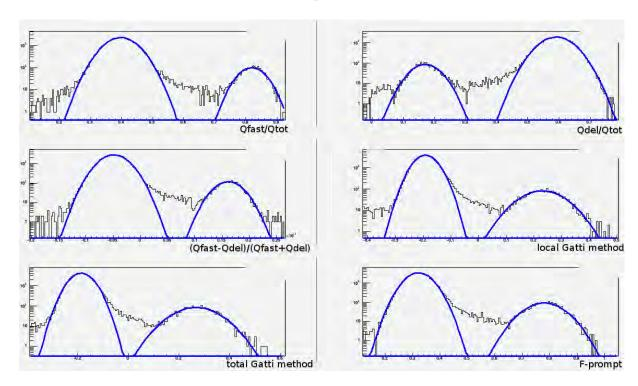


Figure 5.20: The separation plots for each of the separation methods: Q_{fast}/Q_{tot} (top left), Q_{del}/Q_{tot} (top right), $(Q_{fast}-Q_{del})/(Q_{fast}+Q_{del})$ (middle left), local Gatti method (middle right), total Gatti method (bottom left), F-prompt (bottom right), for the energy range (63-75) phe and fitted with two Gaussian functions, one for each peak.

However, it was noticed that the Gaussian function does not fit the electron peak well, and there is a surplus of events towards the neutron peak. This may have been caused by either the Gaussian function not being the correct function to fit the peaks or an effect induced by neutrons. In the first case it has been speculated that the peaks should actually follow the binomial distribution:

$$f(k; n, p) = \binom{n}{k} p^k (1 - p)^{n-k}, \tag{5.8}$$

where, in our case, n is the total number of photoelectrons arriving for a given pulse, k is the the number of photoelectrons that are a success, i.e. slow for an electron pulse with a probability p. The parameter n should, in principle, be constant hence the need to separate the signals into energy slices which correspond to events with a fixed number of photoelectrons (to an approximation). The probability p, in the definition of the binomial function, is the parameter that signifies the peak position. This reasoning can be soundly applied only to the F-prompt, Q_{del}/Q_{tot} and Q_{fast}/Q_{tot} methods. The results of fitting the binomial distribution to both peaks are shown in Fig. 5.21. The surplus in the region of intermediate events, i.e. between the neutron-like and gamma-like events remains, hence the alternative explanation, described below, was also pursued.

5.3.1 The third Gaussian population

To check if the surplus of the electron like events is in fact an artifact of the neutron interactions an additional study was performed on the other data sample taken with the 0.7 l chamber during the N_2 contamination run. During this measurement, at 0 ppm of contamination, the chamber was illuminated first with a ⁶⁰Co source and then with an Am-Be source. This allowed to extract the separation plots for the same energy slices, as for the dedicated neutron measurement, both for a source with neutron interactions and for a source without them. Thus, it was possible to compare these two datasets. If for the ⁶⁰Co runs the surplus of events would still be visible, then the effect is not generated by neutrons. However, if the surplus is visible only in the neutron runs (with the Am-Be source), then it can be a result of inelastic neutron interactions in the chamber, where the neutron interaction could produce a γ -pulse causing an intermediate type of event. In Fig. 5.22 the distributions for all the tested parameters are plotted for both the ⁶⁰Co and Am-Be runs normalized to height of the electron peak, as to be able to compare the two populations in spite of different statistics. The effect of subtracting the pure electron-like peak from the Am-Be electron-peak is also plotted. It can be observed, that indeed a residue of events remains after subtracting the pure events. However, the statistics are too low to be able to describe the distribution precisely.

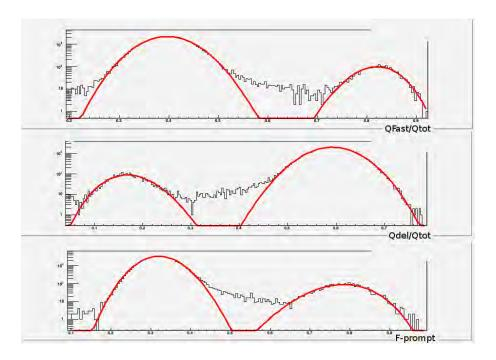


Figure 5.21: The separation plots for each of the separation methods: Q_{fast}/Q_{tot} (top), Q_{del}/Q_{tot} (middle), F-prompt (bottom), for the energy range (63-75) phe where the peaks are fitted with the binomial distribution.

By trial and error, it has been determined that, if a third population is assumed the obtained peaks are best fitted by a sum of three Gaussian functions, where the third Gaussian is closely positioned to the electron peak and responsible for the hypothetical inelastic-neutron population. An example of such a fit can be seen in Fig. 5.23. However, it is difficult to draw any definite conclusions from this exercise, since the statistics of the data are definitely too low. A dedicated measurement with a much larger sample would be desirable, especially with a coincidence measurement that would allow neutron tagging, like in [117], to be sure that the extra effects do arise from neutron interactions and not from something else. Such an analysis will be possible for the data taken with the 100 l detector. For the sake of this analysis, we will however assume that a third population of events is present.

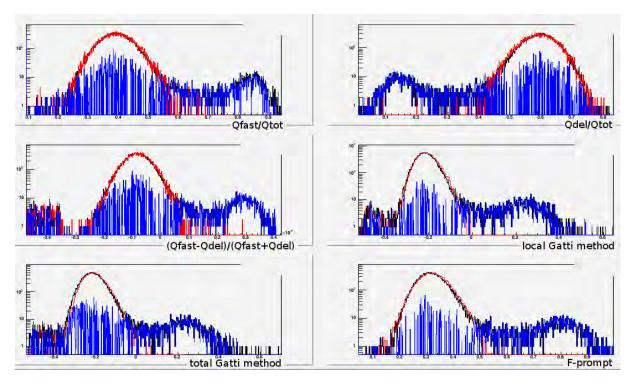


Figure 5.22: The separation plots for each of the separation methods: Q_{fast}/Q_{tot} (top left), Q_{del}/Q_{tot} (top right), $(Q_{fast} - Q_{del})/(Q_{fast} + Q_{del})$ (middle left), local Gatti method (middle right), total Gatti method (bottom left), F-prompt (bottom right), for the 60 Co events (red) and Am-Be events (black) and their difference (blue) in the (80-120) phe energy range.

5.3.2 The pulse shape discrimination with the dedicated neutron dataset

The assumption of three populations has been used to analyze the aforementioned results of the dedicated neutron run to check if these populations have an energy dependence or how the separation differs. For each of the chosen energy slices the positions of the three Gaussian peaks were obtained by means of a fit. These positions with respect to energy are plotted in Fig. 5.24. The blue points represent the neutron peaks, while the green and red the intermediate and gamma populations respectively. It can be observed, that for all methods the neutron and gamma populations at higher energies tend to edge closer to each other, however this could be an artifact of the low statistics of the neutron sample. The method $(Q_{fast} - Q_{del})/(Q_{fast} + Q_{del})$ shows the strongest of this type of behaviour making it practically unusable in a normal experiment. The other methods give separation

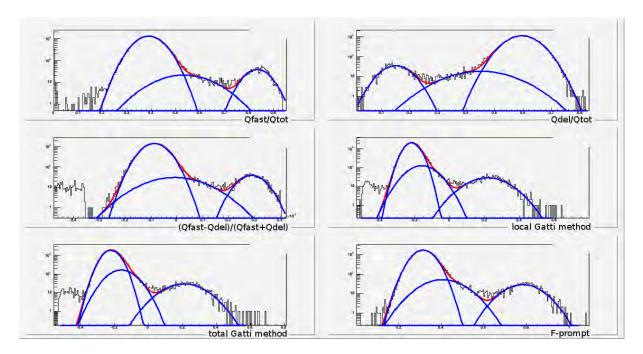


Figure 5.23: The separation plots for each of the separation methods: Q_{fast}/Q_{tot} (top left), Q_{del}/Q_{tot} (top right), $(Q_{fast} - Q_{del})/(Q_{fast} + Q_{del})$ (middle left), local Gatti method (middle right), total Gatti method (bottom left), F-prompt (bottom right), for the Am-Be events fitted with three Gaussian functions.

at the level of at least 1 σ .

The fact that the results are best described with three Gaussians makes using the separation parameter S, defined in Eq. (5.7) questionable. Therefore a new way of estimating the quality of the separation of the peaks must be found. In principle, two approaches are possible. The first, more ambitious, is to try to separate the pure neutron peak from both the gamma and intermediate populations. The second approach, likely to be used if problems are encountered pursuing the ambitious approach, is to try to separate only the gamma peak assuming that the intermediate population is somehow an effect of the presence of neutrons. This assumption is supported by the reasoning in the previous section. I have chosen to estimate the quality of a pulse shape parameter with the following method. Let us estimate at what value of a given pulse shape parameter the electron and intermediate populations would contaminate the neutron population at a defined level. Let me choose this level as 1 in 10⁷ events. This is obtained by numerically

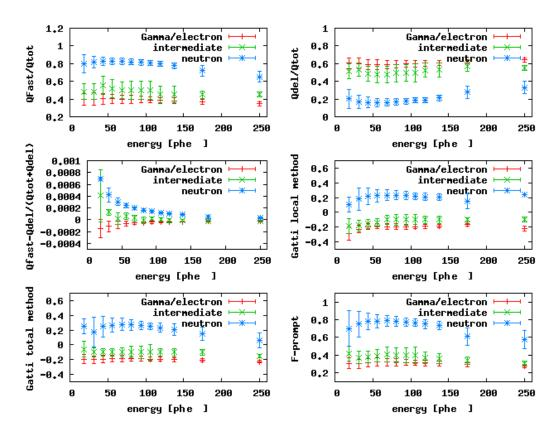


Figure 5.24: The positions of the Gaussian peaks for each of the three populations with respect to energy for each of the separation methods: Q_{fast}/Q_{tot} (top left), Q_{del}/Q_{tot} (top right), $(Q_{fast}-Q_{del})/(Q_{fast}+Q_{del})$ (middle left), local Gatti method (middle right), total Gatti method (bottom left), F-prompt (bottom right). The error bars are the Gaussian variances obtained from the fit. The red points denote the electron peak, the blue the neutron peak and the green the intermediate peak. The fits of the neutron peak at high energies are not trustworthy since the number of analyzed events is rather small.

solving the following equation for y,

$$\mp \frac{1}{N_{\gamma} + N_{int}} \int_{X_n \pm 4\sigma_n}^{y} (F_{\gamma} + F_{int}) = 10^{-7}.$$
 (5.9)

Here $N_{\gamma} + N_{int}$ is the total number of non-neutron events and F_{γ} and F_{int} are the gamma-like and intermediate event distribution functions, in this case the fitted Gaussians. Like in Eq. (5.7) X_n and σ_n are the neutron peak position and dispersion. The lower sign is for the Q_{del}/Q_{tot} method while the upper one is for all the other ones. Once y is found, another integral is calculated to estimate the number of surviving neutrons. The fraction of neutrons surviving a cut with the goodness of 10^{-7} will be the parameter quantifying the efficiency of the applied separation method, i.e.

$$S_{new} = \pm \frac{1}{N_{neut}} \int_{y}^{\infty} F_{neut}, \tag{5.10}$$

where again the lower sign is for the Q_{del}/Q_{tot} and F_{neut} is the neutron distribution function.

However, when calculating this parameter for contamination with both electron-like and intermediate populations it became clear that the fit of the intermediate population was, in fact, correlated to the gamma-like population and did not allow for sensible estimation of the cuts. Because of this, and based on the fact that the intermediate events are most probably inelastic neutron events, which has been confirmed by a dedicated Monte Carlo simulation [118], I have chosen the less ambitious approach to use only the gamma peak population to gauge the efficiency of the pulse shape parameters. Thus, the y was calculated by solving,

$$\mp \frac{1}{N_{\gamma}} \int_{X_n \pm 4\sigma_n}^{y} (F_{\gamma}) = 10^{-7}, \tag{5.11}$$

instead of Eq. (5.9). The fraction of neutrons surviving this cut is shown in Fig. 5.25. The difference between the parameters is not very profound and, in principle, one could argue that all of the parameters represent a similar quality with the exclusion of the $(Q_{fast} - Q_{del})/(Q_{fast} + Q_{del})$ at low energies, and the Gatti total method at highest energies (there, however, the statistics are rather scarce). It can also be observed that the Gatti method is much better when an average pulse is generated for each energy slice rather than for a single waveform for all events.

One must realize however, that usually cuts are not applied for each energy slice. In practice, what would be used in a data analysis, or what would be the most desirable, is to have a cut that is a single value of the parameter for all energies of an event. In order to determine this cut for each parameter, one should choose the energy for which the cut is most stringent and apply it to all other

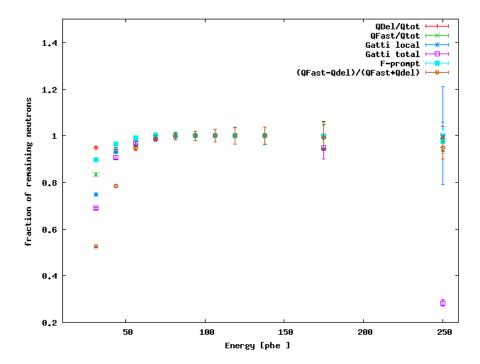


Figure 5.25: The fraction of neutrons surviving a 1 in 10^7 cut of gamma like contamination for the Q_{fast}/Q_{tot} , Q_{del}/Q_{tot} , $(Q_{fast}-Q_{del})/(Q_{fast}+Q_{del})$, local Gatti method, total Gatti method, F-prompt methods. The error bars, are based on the Poisson variance of the number of counts in the neutron peak.

energies. The positions of the cuts for each energy slice can be seen in Fig. 5.26. For each pulse shape parameter the highest value of the cut was chosen as the proper cut in the parameter (except for the Q_{del}/Q_{tot} method, where the lowest value was chosen because the peaks are inverted). Using this value the integral of the remaining neutrons was calculated again to check which parameter will allow the collection of most neutrons with a fixed value of the cut. The results of this are shown in Fig. 5.27.

As it turns out in this case the best method to use seems to be the local Gatti method, which benefits from its lack of dependence on energy. Hence it would be advisable to use it as the most stable discrimination method. It could probably be improved if the energy slices in which the average pulses are created were even narrower. This would, however, require a larger sample of neutron events than those available for this study. It is actually possible, that the Gatti method could still be improved if the events used for the average pulses were tagged as neutrons or gammas, i.e. using a setup like in [117], when in this method the events were selected using a conservative cut on Q_{fast}/Q_{tot} . It must be said,

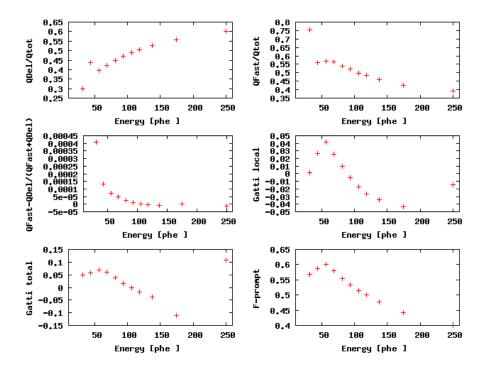


Figure 5.26: The positions of the cuts allowing a 1 in 10^7 contamination of gamma like for the Q_{fast}/Q_{tot} , Q_{del}/Q_{tot} , $(Q_{fast}-Q_{del})/(Q_{fast}+Q_{del})$, local Gatti method, total Gatti method, F-prompt methods, respectively.

however, that because of the requirement of the average pulses as input, the Gatti method is troublesome to implement in a running analysis program. Especially if the contamination with nitrogen or oxygen changes with time, which could change the average waveform shapes, as has been described in this chapter and in [111, 106]. This analysis though can be used at the final stage of an analysis, when all calibrated pulses are available and a more detailed approach is needed.

This is why, for practical purposes it would be best to use one of the "standard" pulse shape discrimination parameters, and from these the F-prompt seems the wisest choice. For most energies it is just as good as the local Gatti method, at low energies surpassing the Q_{fast}/Q_{tot} and Q_{del}/Q_{tot} parameters, probably thanks to the averaging used in the calculation, which helps this method overcome fluctuations present at low energies. It's true that at higher energies the fraction o remaining neutrons drastically lowers, due to the fact that the neutron peak position goes down (see Fig. 5.24), but it is worth noting that these last two bins have the lowest number of neutrons in them, so the gross loss of neutrons is not that large.

As a result, this study suggests the use of the F-prompt and local Gatti methods

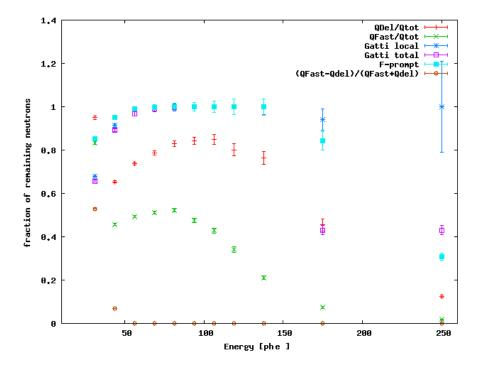


Figure 5.27: The fraction of neutrons surviving a fixed cut with at most 1 in 10^7 of gamma like contamination for the Q_{fast}/Q_{tot} , Q_{del}/Q_{tot} , $(Q_{fast}-Q_{del})/(Q_{fast}+Q_{del})$, local Gatti, total Gatti, F-prompt methods. The error bars, are based on the Poisson variance of the number of counts in the neutron peak.

as the best choices for pulse shape discrimination. It should be however noted, that this result is not conclusive and should be repeated with a larger data sample and possibly a dedicated Monte Carlo simulation to understand the intermediate events, or a neutron and gamma tagging method as described in [117] to allow for an unbiased separation and understanding of the recorded events. The data for such a next order study has already been collected and the analysis is in progress. It will be also very interesting to repeat this kind of study with the 100 liter detector, where much more data can be collected.

5.4 Preliminary neutron quenching measurement.

It has been mentioned before, that the number of photons emitted in low-energy nuclear recoils is smaller than for gamma-like events of the same energy. This is called quenching and is observed in most detector media. This effect is usually quantified by defining the quenching factor q_f as the ratio of the scintillation

light emitted in a nuclear recoil and in an electron recoil of the same energy. In an ideal situation this factor would be equal to one, but in reality it is usually much smaller. The quenching factor is obviously a very important parameter, since it can affect the amount of light coming from nuclear recoils, and hence WIMPS, yet it has not been studied thoroughly for argon, at least on the level of experiment. Some measurements exist for xenon ([119], [120]) but for argon and neon the measurements do not give energy dependent values and are in fact single values for a range of energies ([98],[121],[122]). There are models that try to predict the value of q_f and its behaviour with energy, but it is hard to make any assumptions without sound measurements. It does seem, however, that the most popular model, that of Lindhard, has problems with explaining the behaviour in xenon [123]. Actually, in [123], an interesting approach can be found, where the Lindhard model is combined with Birks's saturation law. This combination is in much better agreement with the xenon, argon and neon data.

5.4.1 Lindhard model and Birks's saturation law

The Lindhard Model

The Lindhard model [124] tries to explain the quenching effect by dividing the energy deposited by particles in the medium into electronic and nuclear stopping power. The electronic stopping power can be described as all effects that result in the excitation or ionization of the medium atoms. The nuclear stopping power is only significant at low energies, hence interesting in terms of a WIMP search, and is the effect of the energy being transferred into collisions with the medium nuclei which contribute to the kinetic energy (or thermal motion) of atoms. Based on these assumptions, Lindhard proposed the following functional dependence:

$$f_n = \frac{k \ g(\varepsilon)}{1 + k \ g(\varepsilon)},\tag{5.12}$$

where, for a nucleus of atomic number Z, $\varepsilon = 11.5~E_R(\text{keV})\text{Z}^{-7/3}$, $k = 0.133~\text{Z}^{2/3}\text{A}^{-1/2}$ and $g(\varepsilon)$ is approximated by: $g(\varepsilon) = 3~\varepsilon^{0.15} + 0.7~\varepsilon^{0.6} + \varepsilon$. This model is apparently very successful at lowest energies, but at slightly higher energies it seems that other effects, like collisions of two excited dimolecules into one excited dimolecule and a ground state dimolecule or superelastic collisions that quench the singlet states to triplet states can occur and additionally increase the quenching. This is why the Lindhard model is combined with Birks's saturation law.

Birks's Saturation Law

This law is based on the assumption that a particle passing through the medium (the law was first described for liquid scintillator) produces a track of ionization

that can be described in terms of a core and a penumbra [125]. The penumbra is a low ionization density region that surrounds the high ionization density core. So, most of the quenching processes will occur in the core. There are two assumptions to be made. First, that the number of exciton (dimolecule) collisions that increase the quenching depends on the ionization density, and second that the number of excitons produced per unit of path length as well as the local concentration in the core are proportional to this density. Together they lead to Birks's saturation law [126], which in turn allows to calculate the quenching function [123]:

$$f_l = \frac{1}{1 + k_B B \frac{dE}{dx}},\tag{5.13}$$

where k_B is the overall collision probability and B is a parameter connected to local concentration in the core. In liquid argon $k_B B = 7.4 \times 10^{-4} \text{ MeV}^{-1} \text{ g cm}^{-1}$ and $dE/dx = 1586.4 \text{ MeV cm}^2/\text{g} = 31.9 \text{ MeV/amu}$.

The total quenching factor is then calculated by combining the two factors above:

$$q_f = f_n \times f_l \tag{5.14}$$

and for argon could be compared to one point, measured previously by the WArP collaboration [121], which is presented in Fig. 5.28. Note that the prediction of the combined model in this plot is a result of fitting one of the parameters of Birks's law.

Apart from the theoretical uncertainties it is important to measure q_f in argon and its dependence on recoil energy - if it exists - to better understand the signals in the WArP detector. The WArP collaboration is preparing a dedicated experiment with a fixed neutron beam in the Braunschweig facility in Germany. In the meantime to have a qualitative idea of the value of q_f a preliminary measurement was carried out using the 0.7 liter chamber described in Section 4.6.2 and in the paper on the nitrogen contamination [106].

The chamber was filled with liquid argon, and no external electric field was applied, so only primary scintillation light was observed. The chamber was radiated using a $^{137}\mathrm{Cs}$ source to measure the light yield for electron-like particles and with an Am-Be source to see the effect of exposition to neutrons. The principle of the measurement was to obtain a light yield in phe/keV both for electron-like and neutron-like recoils and compare them to obtain the quenching factor. The light yields were obtained by fitting the full absorption peak and the Compton edge to the $^{137}\mathrm{Cs}$ spectrum for gamma-like events. The determination of the light yield for neutron-like events used a specially tailored Monte Carlo generated neutron spectrum which was fitted to the Am-Be spectrum found in the measurement. The neutron Monte Carlo spectrum, and the Am-Be neutron spectrum are shown in Fig. 5.29 . In principle, it is also possible to fit the γ spectrum, present in

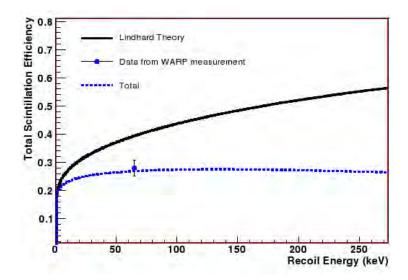


Figure 5.28: The combined Lindhard model and Birks's saturation law quenching factor (dotted line) compared with the WArP measurement of the quenching factor. The pure Lindhard model is also shown for reference [123].

the Am-Be source, but since it has no significant features a fit would be rather imprecise - hence the need for the ¹³⁷Cs source.

The electronics used for this measurement was the same as the one used for the 2.3 liter chamber in the wimp_005 runs - integrated with a 120 μ s decay time preamplifier, sampled at 100 MHz and with a 14 bit ADC range but with a single 2" PMT. The data taken were analyzed as no field data, since the secondary pulses were not present. The data acquisition software and the NEWSCAN software package, described in the next chapter, were modified to work with only one data channel. The whole electronics and DAQ setup for this measurement were prepared by the author of the thesis.

The first measurement was performed by irradiating the chamber with the $^{137}\mathrm{Cs}$ source and the Am-Be sources separately and comparing the light yields obtained. The results were 1.67 phe/keV (rather high compared to other runs with the 0.7 liter chamber) for the $^{137}\mathrm{Cs}$ full absorption peak and 0.835 phe/keV for the neutron source. The result of this fit is plotted in Fig. 5.30 (a), where the assumption from the Lindhard model, i.e. a constant light yield of 0.5 phe/keV in the range 200-400 phe is plotted for comparison. The quenching factor obtained in this analysis: $q_f = 0.5$ is rather high as far as noble gases are concerned.

It has been observed, however, that a large amount of light decreases the quantum efficiency of a phototube. To avoid the influence of this effect another run was performed where the chamber was simultaneously illuminated with the ¹³⁷Cs and

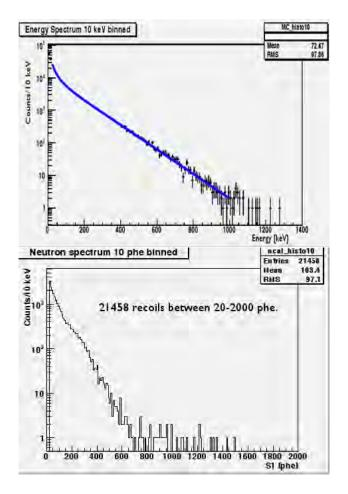


Figure 5.29: The dedicated Monte Carlo neutron spectrum used to determine the light yield of neutrons and a neutron spectrum obtained during the measurement with the Am-Be source [127].

Am-Be source, assuring that the loss of quantum efficiency affected both spectra in the same way. The neutron light yield obtained in the second measurement was indeed lower than in the first one and was measured to be 0.65 phe/keV resulting in a quenching factor of $q_f = 0.39$. It is important to note, that this measurement assumes that the quenching factor is constant in a range of energy from about 150 keV to 300 keV which may not be the case. Although, if the Lindhard-Birks model is correct this should be a good approximation. It should be noted, that the q_f value obtained here is higher than the value previously quoted by the WArP collaboration ($q_f = 0.28$). As such, it would not lay on the combined model prediction in Fig. 5.28, but it should be noted that this curve, taken from [123], was fitted to the old WArP value. Then it is probable that the curve should be

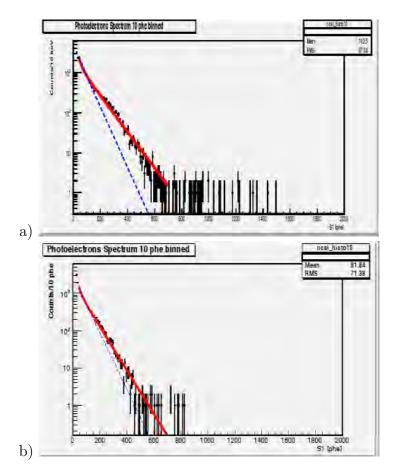


Figure 5.30: a) The results of the fit (red) to the experimental neutron spectrum (black) compared with the expectations coming from the Lindhard theory (blue) for the run with the chamber irradiated with only the Am-Be source and b) the run with the chamber irradiated simultaneously with Am-Be and ¹³⁷Cs sources.

refitted for the new value of q_f and new values of Birks's model parameters would be obtained.

Nevertheless, the measurement reported here remains only an ad-hoc approximation and a dedicated measurement with monochromatic beams in Braunschweig is needed to precisely measure the quenching factor for argon.

Chapter 6

Analysis of the Data Collected with the 2.3 liter Detector

The 2.3 liter WArP detector, though intended as only a testing ground for the main detector, was actually able to provide significant physics results on its own. The published result of the Dark Matter search was quite competitive with other direct detection experiments at the time of the first presentation [128]. The small WArP chamber delivered the first results from an argon Dark Matter detector, thereby becoming a sort of proof of concept for all the projects working to implement argon for this use. As such, it was a large success, since most expectations were confirmed or even exceeded, but some surprising effects were encountered as well, which introduced new angles, but also challenges into the field of argon Dark Matter detectors.

The object of this chapter is to describe the published results [101], to present further work on the development of the analysis program and its application to the collected data, to discuss studied backgrounds and to see whether it is possible to improve the published result by using the improved version of the analysis program - in a large part the result of the work performed by the author of this thesis.

During the course of running of the WArP detector I had a hand in many aspects of the analysis process, that will be described in this chapter. First of all, I became solely responsible for maintaining and developing the main reconstruction software used in the analysis. Subsequently I rewrote and restructured this code, to optimize it in terms of speed, performance and readability. Before that, I took part in the analysis that resulted in the publication described here [101], mainly on the studies of the neutron background that was spurred by the observation of unexpected behaviour of neutron induced events during the first calibration performed with the small chamber. This input included scanning neutron events to search for cases where the neutron would interact two or more times, participating in the development of a classification scheme for the neutron events and develop-

ing a code, that would automatically reconstruct the multiple interaction events. I also participated in the analysis of the other background region, the so called "baffo" events, which exhibit characteristics of both neutron-like and electron-like events, namely by performing the first visual scanning and searching for preliminary dependencies of these events. I also participated in the second analysis run, where my involvement was mainly, but not limited to, developing a method to fit the WArP 2.3 liter chamber data to find the decay time of the slow component of the background events.

6.1 WIMP limits obtained with the WArP 2.3 l chamber result

6.1.1 The chamber setup

The chamber used in the measurements was the old 2.3 liter chamber, which, as mentioned before, was constructed with little care of its radiopurity. This was considered a bonus in the research phase, because it allowed the collaboration to perfect the technology in conditions much worse than the ones expected from the proper, radiopure detector. During the cited measurements the chamber was equipped with $7 \times 2''$ PMTs read out by 20 MHz sampled electronics. This meant that only a robust X-Y identification was possible and the primary pulse analysis was crude at best, since one channel corresponded to 50 ns and so easily encompassed the whole range of the fast, 7 ns component of the scintillation light. The signals from the PMTs were integrated using a preamplifier with a time constant of $40~\mu s$. Events were selected for recording based on a majority trigger condition, which usually meant that at least four PMTs were needed to accept a signal (in the 7 2" PMT setup).

The chamber was filled with commercial grade argon, which, as expected, resulted in the presence of radon in the detector chamber. Radon is a natural contaminant, that is present in the atmosphere, but, since it is chemically in the noble elements group, even more so in noble gases and liquids. Radon usually comes from decays of radium and its longest lived isotope 222 Rn has a half-life of 3.8 days. It is the longest half-life in the whole radon decay chain, so the radioactive contamination related to radon disappears after about a month. In the meantime, the presence of radon in the chamber turned out to be beneficial for the experiment, because valuable insight into the interactions of α particles and recoiling nuclei was gained by observing the decays of 218 Po and 214 Po, which are the only two radon daughters to decay emitting an α particle. These events were easy to locate, because after the first β decays in the radon chain the daughters' atoms had a positive charge and so were drifted down in the electric field towards

the cathode region, where the nuclear recoil events were usually registered. A decay of the number of fast recoil events in the cathode region has been observed with the expected ²²²Rn decay time [129].

Radioactive sources were used to calibrate the chamber, both for electron-like and recoil-like events. In the first case 137 Cs and 60 Co, while in the second an Am-Be neutron source was implemented. The results of these calibrations were used to determine the light yield, i.e. the ratio of photoelectrons per keV of deposited energy, obtained in the chamber. Measurements of the energy of the recoiling 210 Pb and 214 Pb nuclei (coming from the α decays of polonium mentioned above) and from the natural neutron spectrum present in the chamber before the polyethylene shielding was installed served to calculate the light yield for nuclear recoils. To perform all of these calculations the knowledge of the Single Electron Response (SER) spectra, described in Chapter 5 was crucial in order to establish the ADC to phe conversion factor.

6.1.2 Data analysis using the SCANWARP software package

The SCANWARP package, created by N. Ferrari, was the original software used by the WArP collaboration in the course of data analysis. It later evolved into the the NEWSCAN package, written by the author of this thesis, which will be described in the following section. To understand the evolution of the code it is important to understand the workings of the analysis process. It is worth noting that this package was only a part of the whole analysis, since in order to fully analyze the gathered data multiple steps needed to be performed.

- 1. The SER spectra had to be fitted. The results were then used in the main analysis package, to convert the ADC counts into photoelectrons.
- 2. The run was analyzed to check for the effects of oxygen contamination, by examining the height of the average S2/S1 ratio versus the drift time. In the case of contamination, events further from the surface exhibit a lower S2 pulse, since some ionization electrons are "eaten" by impurities, as can be seen in Fig. 6.1 . If that was the case, a correction factor was obtained and used in the subsequent analysis.
- 3. The SCANWARP/NEWSCAN code was run on the data. As a result, for each event, a number of parameters were saved including the height of the S1 and S2 pulses and the drift time.
- 4. The files resulting from the SCANWARP/NEWSCAN analysis were used to apply data cuts and select the interesting events.

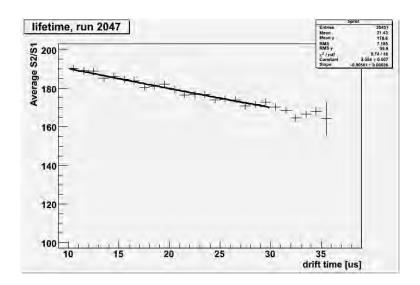


Figure 6.1: The average S2/S1 ratio plotted vs drift time for run 2047 of the wimp_002 dataset. A decrease of the ratio for longer drift times suggests the presence of impurities that deplete the number of ionization electrons drifting up to the surface.

The SCANWARP package

The SCANWARP package originally was a code written in the simplest version of the ANSI C programming language. The code was housed in a single file and all of it resided in the main() subroutine. All of the constants used in the analysis were hard coded in each place where they were used, which made it rather difficult to modify any parameters needed by the analysis process. At some point, a small restructuring of the code took place and parts of the code were moved to external functions, but the sequence of the code remained the same.

At the beginning, the code first read in the waveforms from the raw data file and applied the phe/ADC coefficient coming from the SER spectra. The waveforms were smoothed to get rid of instrumental artifacts. The first step of the analysis was to find the maximum of the signal and check whether it was saturated. This was done for both the low-gain and high-gain data, mentioned already in Section 4.4, and if the high-gain was saturated the low-gain was used for further analysis. An example of a saturated high-gain pulse and its corresponding low-gain pulse can be seen in Fig. 6.2.

Next, the signal was differentiated and the resulting waveform served to find peaks in the event. Once located, the peaks were then classified as primary (S1) or secondary (S2) based on their times of onset (tp, ts), i.e. the first was usually the primary, then the secondary, but also based on how fast the pulses grew -

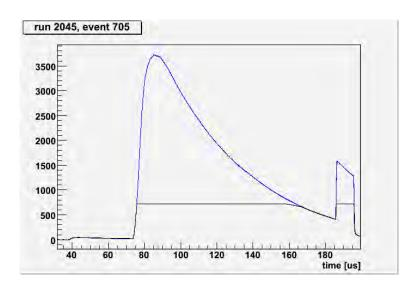


Figure 6.2: An event with a pulse saturated in high gain (black) found in the WArP 2.3 liter detector. The low-gain (blue, multiplied by 10) is shown for reference.

these parameters are called: rs, rp, rise time of the secondary and primary signal respectively. Due to the different origins of the two types of pulses, as described in Chapter 4, the secondary signals usually take longer (from 10 to 20 μ s) to reach the pulse maximum as compared to up to 7 μ s for the primary pulse. The differentiated signal compared with the real pulse can be seen in Fig. 6.3.

The baseline, meaning the instrumental offset of the signal, was calculated and then the primary pulse shape parameter was obtained by calculating the ratio of the signal at 500 ns after the onset and in the region of the maximum of the primary pulse. This is the F-prompt parameter and, since the signal is integrated, it corresponds to the ratio of the quantity of light observed in the first 500 ns after the onset to the total registered light.

Afterwards, a fit was attempted to gauge the heights of the pulses in photoelectrons. It would be near impossible to try to fit a proper functional dependence for each of the hundreds of thousands of events. Therefore, a simplified method was implemented, where average electron-like and neutron-like signals were used as a template for the fit and only their onset and amplitude were used as fit parameters. Both templates were tried for each event, but the saved result was always based on the F-prompt parameter of a given event, e.g. events with a high F-prompt (i.e. neutron-like) were always ultimately saved with the result of fitting the neutron template. Saturated events were fitted based on their behaviour in tail section of the signal, dominated by the preamplifier decay time. In Fig. 6.4 a typical event is presented with the average electron-like and neutron-like templates with their

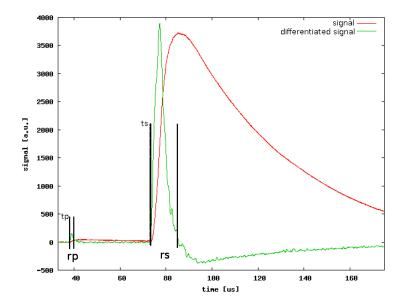


Figure 6.3: A typical event (red) with the differential of the signal (green) overimposed. The positions of the tp (primary arrival time), ts (secondary arrival time), rp (primary rise time), rs (secondary rise time) parameters are shown.

onsets and amplitudes resulting from a fit.

The whole procedure described above was repeated for each event collected. The results of the analysis were then presented using a PAW [130] macro. Many of the events, that survived the applied cuts were then scanned visually, to check for software bugs and misreconstructed events. In such a case, the events were flagged and not taken into account in further analysis.

6.1.3 The published results

The first results from the small 2.3 liter chamber were presented in March 2006 [128]. At the time they were competitive with the leading experiments in the field. These results were based on a sample of runs from the wimp_002 data set, totaling an exposure of 96.5 kg×days and 2.8×10^7 analyzed triggers.

Before the data taking a neutron calibration was performed, which provided a lot of insight into the neutron background, and which allowed to set the cuts to select neutron-like events. The working hypothesis of most Dark Matter searching experiments is that a WIMP signature will be identical to that of the neutron, hence the importance of these cuts. Unexpected behaviour was also observed from the neutron population, which will be discussed later in this chapter.

In the course of the WIMP search, eight events survived the defined cuts. All

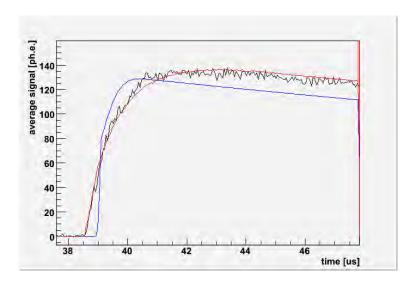


Figure 6.4: A typical gamma event primary pulse (black) with the results of fitting a neutron-like (blue) and electron-like (red) template.

were found in the energy bin between 40 keV and 54 keV. Five of these events were so called single-hit, while the remainder were double-hit events with two interactions in the experimental chamber, which is a typical signature of neutrons. Therefore the single hit events were also assumed to be coming from the environmental background found in the chamber. So, the result of the WIMP search was declared null. Based on these findings it was possible, using the method developed in [95], to evaluate the excluded region in the cross-section vs WIMP mass parameter space. The result, assuming a 55 keV threshold, allowed to almost exclude the region preferred by the DAMA annual modulation result [82]. This is shown in Fig. 6.5 where the WArP exclusion limit is plotted on the two dimensional plot of spin-independent cross-section per nucleon versus the hypothetical WIMP mass.

6.1.4 Results from the subsequent wimp_003 and wimp_004 data runs

The results from the next data runs [131] have been used to validate some assumptions used in the previous analysis. This data has not been published, since using the analysis program at the time, it was not possible to significantly improve the results obtained in the published paper [101]. For this analysis 43 kg \times days of exposure were obtained totaling a number of triggers over 11.9×10^6 . The electronics and setup in this run were modified and improved. The sampling rate was increased from 20 MHz to 100 MHz which dramatically improved the

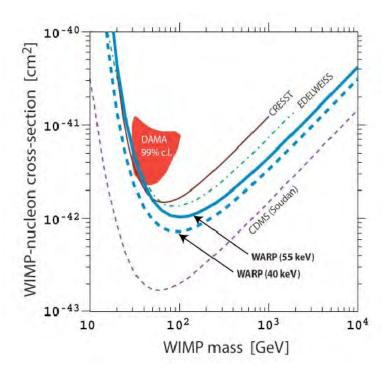


Figure 6.5: 90 % C.L. spin independent limits (solid blue curve) obtained by WArP 2.3 l for a threshold of 55 keV. An analogous curve for a threshold of 40 keV under the (optimistic) assumption that the observed 5 events are due to background is also plotted (dashed blue curve). The limit is compared with the ones from CDMS, EDELWEISS and CRESST and with the allowed 3 σ C.L. from the DAMA annual modulation data. Figure from [101].

pulse shape discrimination procedure. The data was now saved in a single 14bit ADC word instead of the two overlapping 10bit words requiring a large upgrade of the code.

Assuming an acceptance of 50% for nuclear recoils it was possible to obtain a discrimination of 3×10^{-7} based on the pulse shape analysis alone. During this run it was also observed that the typical gamma and neutron signals differ from the standard average signals used in the fit for the signals from previous runs. The difference was ascribed to a possible nitrogen contamination of the sample and spurred the dedicated research program discussed in the previous chapter.

6.2 The *NEWSCAN* software package.

While implementing the new parameters of the electronics setup into the software it was realized, that the software used in the analysis needs to be more versatile. To facilitate the whole analysis process additional improvements were made. As a result, an idea was born to create an object oriented package based on the original SCANWARP package, that would be easier to modify in the case of changing parameters of the runs. This package was named NEWSCAN, to emphasize the continuity between the new and old codes. The main aspects of the analysis process were kept, but the code was rewritten using C++ syntax with classes and an object oriented approach. In the course of this work, many bugs in the original code were found and many improvements were introduced into the code. These include:

- The window, where the code searched for the onset of the pulse, was widened to the whole data range. Before the code only analyzed events where the primary pulse occurred between 38 μ s and 40 μ s. In the later data runs this allowed to analyze events, that were triggered on the secondary pulse
- The baseline calculation has been improved and a running baseline algorithm has been implemented.
- An optional running mode was created to check the synchronization of the pulses. In earlier runs, the synchronization was performed using a test pulse injected at the end of each event.
- The pulse-shape parameter (F-prompt) was now calculated at five time intervals, which were defined for each dataset, after the onset of the pulse, to be able to choose the best separation for a given run.
- Saturated events that could not be fitted via extrapolation, were marked with a special flag and excluded from the analysis.
- The parameters used in the analysis have all been moved to a single instance class both for easy reference and faster loading times.
- The analysis time has been shortened by optimizing the code and its usage of large arrays.
- Additional parameters have been introduced into the external analysis, which
 allowed a better procedure of applying cuts. These include the rise times of
 both pulses, new "goodness of fit" parameters for fits of the primary and
 secondary pulses as well as for the baseline region to check for events with
 artifacts before the physical pulses.

Many other minor improvements were introduced to algorithms used in the analysis.

The whole analysis process has been automatized and was possible to run with one script instead of a number of single unrelated programs. A large part in the automatization was played by the database created to store the results of the PMT calibrations. The database grew with time and is now a rich source of information about the runs taken so far by the WArP collaboration. Parameters such as the chamber pressure, number of events in a run, the time duration of a run, calibration coefficients and others can be saved. The database also contains the average pulses for all datasets.

One very important aspect of the improved analysis process was the creation of the average signals used in the fitting procedure. As mentioned before, the average neutron-like and electron-like pulses differ from run to run, presumably depending on the presence of nitrogen, oxygen, H_2O and other contaminants in the liquid. It is therefore reasonable to use separate templates for each data run. The process of obtaining these average template pulses has been automatized by the author and hence the average waveforms for each dataset could be calculated with relative ease. The difference between average waveforms for different runs has already been shown in Fig. 5.9.

6.2.1 Reanalysis of the WArP data using *NEWSCAN*.

Since the new analysis setup allowed much better control of the acquired data it seemed prudent to use the new capabilities and reanalyze the old data to check if an improvement in the acquired sensitivity could be achieved. The analysis procedure I have chosen to use here was to take the wimp_002 dataset, defined in Chapter 4 and recreate the average template pulses for use in the fit of the S1 and S2 amplitudes. Afterwards, the calibration data (ncal_003) together with a few runs from the wimp_002 runs were used as the sample on which the set of cuts to be used was established. This allowed for a "blind analysis" of the remaining runs in the dataset. The cuts were applied to the unanalyzed part of the data and the events that survived the cuts were visually scanned. Based on the events that survived the cuts and the total livetime a new sensitivity of the 2.3 liter runs was achieved. But before we come to this conclusion let us describe the parameters used in the analysis.

parameters used for cuts

- S1 the height of the primary pulse, as determined by the template fit.
- S2/S1 the ratio of the amplitude of the secondary pulse to that of the

primary.

- arrival time the onset of the primary pulse.
- drift time (t_{drift}) time between the onsets of the primary and secondary pulses. It can be transformed into the Z-position in the chamber.
- scartp goodness of fit parameter for the primary pulse, sum of squared differences between the signal and template used for the fit.
- saturation flag used if any of the single PMT channels was saturated, in that case it would be incremented by one. In the case of a totally saturated event, i.e. such, that even the tail part of the signal was saturated the flag was set to 9.
- barx, bary, barxs, barys the barycenter parameters. Calculated as an average of the PMT signals weighted by the amplitude of the primary or secondary pulses, respectively.
- F-prompt the pulse shape parameter, describing the ratio of the light deposited in the fast component, to the total light in the primary pulse. It was calculated at 5 intervals: 100, 200, 300, 400, 500 ns after the onset (F-prompt₁₀₀,...,F-prompt₅₀₀).

Using the neutron calibration runs as the blind sample for analysis, cuts were set in order to select the searched for events from the whole sample. These cuts can be divided into technical cuts to select only well reconstructed physical events and into physical cuts to select only neutron-like interactions. The technical cuts chosen are defined in Tab. 6.1. These cuts serve to discard noise and badly reconstructed events. For example the arrival time cut is used, because the trigger was hardware set at 38.5 μ s hence, if an event exhibits an arrival time largely different from this, it is usually a sign that it is misreconstructed (the software is in principle capable of reconstructing events with a different arrival time). The drift time cut on the other hand serves to select the fiducial volume in the chamber. The new software has allowed to enlarge this volume. Before, the lower value cut used was 10 μ s, the new software is capable of reconstructing events closer to the surface, even as close as 5 μ s. The upper bound of this cut is used to cut out events happening at the cathode of the chamber. The barx, bary, barxs, barys cuts serve to eliminate single PMT discharges and the scartp cut eliminates events with a pathological primary signal. The S2 > 0 cut actually serves to cut out completely saturated events, in which it is impossible to even judge the value of the secondary signal and hence the S2 value is arbitrarily set to 0. The cuts are also pictured in Fig. 6.6.

Parameter	Cut	Percentage of Events surviving cut
Arrival time (tp)	$(37,42) \mu s$	78.3 %
Drift time (t_{drift})	$(5,35) \mu s$	60.3~%
Number of peaks	=2	75.6%
F-prompt ₅₀₀	< 1	96.8~%
$\sqrt{\mathrm{barx}^2 + \mathrm{bary}^2}$	< 0.45	73.7%
$barxs^2 + barys^2$	< 0.05	99.7%
scartp	< 8	84.7 %
S2	> 0	61.4 %

Table 6.1: The technical cuts selected based on the "blind" sample analysis from the neutron calibration run. Details in text.

Tab. 6.2 presents the "physics" cuts selected based on the blind sample analysis. The S2/S1 and F-prompt₅₀₀ cuts were used to select the neutron induced recoil events, working with the assumption that WIMPs would induce the same kind of events. The distribution of these parameters is shown in Fig. 6.7. The S1 cut is based on taking the F-prompt₅₀₀ distribution, applying the selected S2/S1 cut and then calculating how many electron recoil events would end up in the neutron/WIMP region. Assuming a cut on F-prompt₅₀₀ of 0.8, this parameter has reached a satisfactory value of less than 1 in 10^8 for a cut in S1 of 40 phe, corresponding to an energy cut of 32 keV, assuming the light yield for nuclear recoils $Y_{nc} = 1.25$ phe/keV [132].

Parameter	Cut
S1	> 32 keV
S2/S1	(10,30) (0.8,0.95)
F-prompt ₅₀₀	(0.8, 0.95)

Table 6.2: The physics cuts selected based on the "blind" sample analysis from the neutron calibration run. Details in text.

Results

 2.28×10^7 events of the wimp_002 data run have been analyzed for a total livetime of 44.82 days, which combined with the larger fiducial mass of 2.36 kg

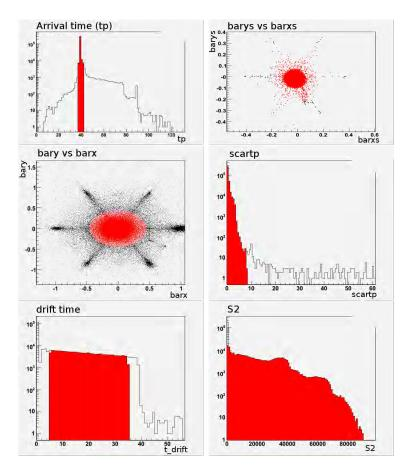


Figure 6.6: Distributions of the parameters used in the cuts, with the selected regions marked red. The parameters are arrival time (top-left), barxs vs barys (top-right), barx vs bary (middle-left), scartp (middle-right), drift time (bottom-left), S2 (bottom-right).

resulted in a total exposure of 115.2 kg×days, compared to 96.5 kg×days for the published data[101]. 18 events have been found in the selected window which are assumed to be neutron background. This claim is founded on the observation that, through visual scanning 6 of these events have been identified as double secondary events. Since, using a Monte Carlo simulation it has been determined that the double events should represent about 30% of all events attributed to neutrons [133], it can be safely said, that within the error all of the observed events can be accounted for by neutron background. The results of the analysis can be observed in Fig. 6.8, where all the events are plotted based on their F-prompt and S2/S1 values, the selected events being colored in blue.

Assuming, that all of the observed events are in fact neutron background allows

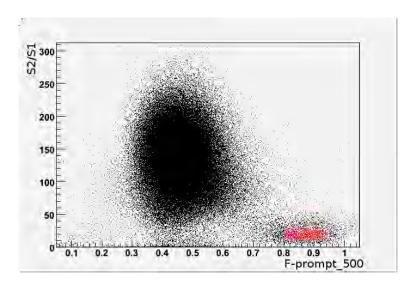


Figure 6.7: Distributions of the S2/S1 and F-prompt₅₀₀ parameters used in the blind sample analysis, with the selected region marked in red.

to perform a background subtraction, and assume, that the run has been a null WIMP run. The sensitivity obtained in this way is shown in Fig. 6.9 a) and it is lower than the previously obtained WArP result, due to the higher total exposure and lower energy threshold. In a conservative approach, a null run can be claimed only for an energy threshold above 63 keV, since the most energetic event was observed at this energy. In this conservative case the sensitivity is presented in Fig. 6.9 b) and is worse than the published one, because when using the improved algorithms and larger fiducial volume new events had to be taken into account. One of these new events turned out to have a high energy and hence the total threshold had to be raised. Nevertheless, both cases prove the proper functioning of the NEWSCAN code. In the main WArP detector, thanks to the outer veto, the neutron background will be kept under better control and so the analysis of the data obtained in a WIMP search will be much more straightforward.

6.3 Background studies.

During the course of the WArP measurements, dedicated studies of some background effects were performed. These studies were an important step in understanding the data from the WArP detector.

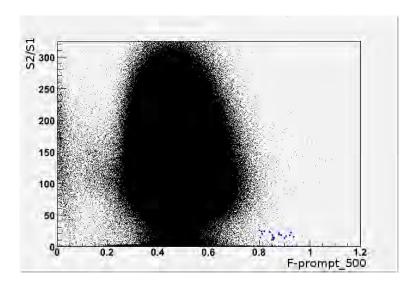


Figure 6.8: Distribution of the events in the wimp_002 data run analyzed with the *NEWSCAN* software package. The 18 selected events in the window of interest are marked in blue.

6.3.1 The Baffo region

The "baffo" region as it is called by the WArP collaboration, meaning "mustache", is a group of events that exhibit the primary pulse shape behaviour of electron-like events while their S2/S1 ratio is that of neutron-like events. They can be found in the lower left of the WArP data plots like in Figs. 6.10, 6.11 where the baffo region is enclosed in the red rectangles. It was of paramount importance to identify these events and make sure that they are not neutron-like events that are lost, due to some detector inefficiency or error in the analysis software.

Two studies have been performed on two data sets, the first one in June 2006 [134] on the wimp_002 dataset and the second one in January 2008 [135] on the wimp_005 dataset and it seems that the mysterious events' origin has been found.

The events from this region, if they are not misreconstructed events - and this has been excluded by visually scanning a sample of over 5×10^2 such events, can be explained either by events that are electron-like by nature, but the ionization signal is somehow suppressed or are neutron-like in nature, but a slow component is somehow added into the primary pulse. Both of these possibilities have been investigated in both analyses.

Already in the first analysis it was apparent that there is little correlation between the neutron and baffo events. Although some leakage of the events exists, but this can be attributed to a rather high value of the upper bound of the F-prompt parameter used in this analysis. Events with the F-prompt and S2/S1

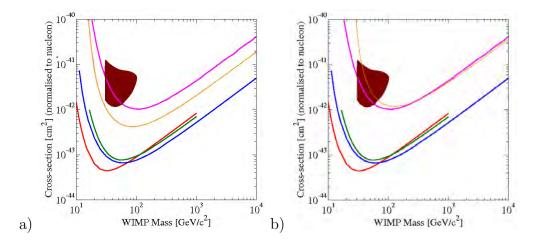


Figure 6.9: The sensitivity of the wimp_002 run obtained using the *NEWSCAN* package (orange) compared with the published WArP sensitivity (purple) and the newest results of XENON[85] (red), CDMS[83] (blue) and ZEPLIN[86] (green) detectors. The DAMA preferred region is also shown for reference. a) presents the case for a 32 keV threshold with background subtraction, while b) presents the case for a 63 keV threshold.

parameters in the range 0.2 < F-prompt < 0.8 and 0.1 < S2/S1 < 30, as in Fig. 6.10 were scanned visually and used for the first analysis.

Three groups of events were identified, which became a starting point for the subsequent analysis. The first group were events with a saturated secondary pulse, where the extrapolated fitting procedure underestimated the height of the secondary pulse hence lowering the S2/S1 ratio. The second group were events that exhibited a dependence in drift time, namely that the number of events in question grows if they are closer to the surface of the liquid. No explanation was found for these events. The third group was attributed to double electron events, because they exhibited a slow primary pulse and two secondary pulses. These events were thought to be Compton scattering events, where a photon traveling in the argon would lose only part of its energy allowing for a second interaction.

The subsequent analysis [135] was able to shed some light on the group of events closer to the surface of the liquid. In the new electronics setup, it was possible to examine these events more closely, for example looking at the rise time of the pulses, and it was ascertained that they are indeed much slower than the standard events coming from the liquid. The cuts used in the new analysis can be summed up as follows:

• S1 > 20 phe;

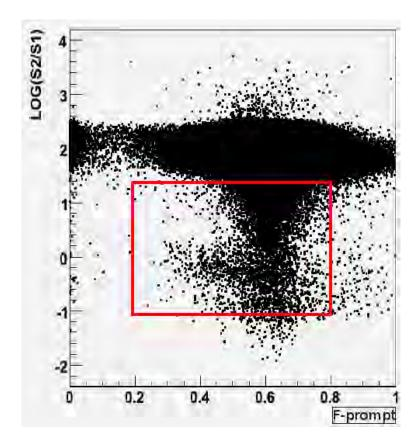


Figure 6.10: A scatter plot of the WArP wimp_002 data with the "baffo" region enclosed in the red rectangle [134]. Details in the text.

- S2 not saturated;
- 6 μ s < t_{drift} < 35 μ s to reject events occurring near the gas-liquid interface for which S1 and S2 are too close;
- 50 μ s < tp < 54 μ s to discard events triggered on noise and the secondary pulse S2;
- $barx^2 + bary^2 < 0.66$ to reject discharges in the PMTs;
- F-prompt < 0.5;
- Log(S2/S1) < 1.5.

It follows that the sample analyzed in the new analysis is different from the previous one.

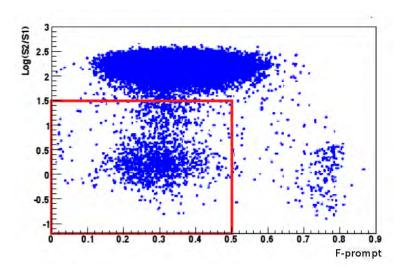


Figure 6.11: A scatter plot of the WArP wimp_005 data with the "baffo" region enclosed in the red rectangle [135]. Details in the text.

Using newly developed tools it was possible to fit the lifetime of the slow component of the signal and the result of this analysis yielded the value of $\tau_{long} \simeq$ $2.86 \mu s$. The result of this fit can be seen in Fig. 6.12 where the average of the slow, close to surface, events is plotted against standard baffo events, for which the $\tau_{long} \simeq 1.43 \mu s$. This phenomenology strongly suggests that these are in fact double Compton events, where one of the interactions happens in the gas phase, since the scintillation light decay time is longer in the gas - $\tau_{qas} = 3.2 \ \mu s$ [136]. If so, then the ionization electrons are less abundant because they come only from the interaction in the liquid and the total secondary scintillation is smaller than expected. The second group of the baffo events identified in the course of the second analysis showed a strange behaviour in the drift time, as seen in Fig. 6.13, where peaks in the number of events were found at intervals of 7 μ s. The explanation of this is that in this particular run, the chamber walls were not covered with a sheet of reflector, instead the walls were painted with a reflective paint. Since the walls were constructed from slanted PEEK¹ rings of equal height, that corresponds to 7 μ s drift time, it was hypothesized that the "baffo" events may originate near the walls in such a way that some of the ionization electrons are caught in the edges created by temperature deformations of the rings. The cluster of events near the cathode was ascribed to a similar effect, where the events occurred in a cavity created to enable the circulation of liquid argon, which was placed at the bottom of the chamber. In the case of such events it would be extremely difficult for

¹An organic polymer, also referred to as an polyaryletheretherketone.

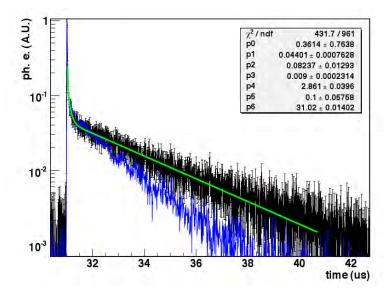


Figure 6.12: A comparison of a slow "baffo" average waveform (black), with a standard baffo event (blue). The close to surface events exhibit a much larger slow component and the fit yields the result of 2.86 μ s as the decay time of the slow component [135].

electrons to arrive in the uniform electric field region, where they could be drifted up, while the primary scintillation light could still be registered thanks to photon reflections off of the walls.

6.3.2 Double neutron events

Already before the data taking and the calibration run used in the published paper unexpected effects in the neutron interactions were observed. The average S2/S1 ratio of these events was expected to be independent of energy, however, in the acquired data such a dependence was observed especially at low energies. In general, most of these events were found to be around a curve defined as:

$$\frac{S2}{S1}[E_{keV}] = \left(a + \frac{b}{E_{keV}}\right) \left(1 - \exp(E_{keV}/10)\right),\tag{6.1}$$

where E_{keV} is the S1 recoil energy in keV and the parameters have been measured as a = 2.1 and b = 670 keV. The confirmation that these are, in fact, neutrons came from observing the double events found above the band which is illustrated in Fig. 6.14. The number of these events is in agreement with the predictions of a dedicated Monte Carlo simulation [133]. It has been assumed that a WIMP inter-

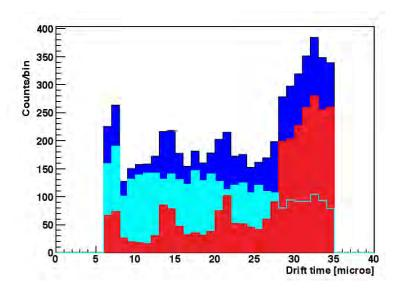


Figure 6.13: The drift times for the "baffo" region events plotted together (dark blue) with a separation to the slow gas Compton events (light blue) which show only a small rising dependence towards the surface and the remaining events which show a definite structure [135].

action would follow the same pattern as the neutron interaction, hence additional cuts were applied in the actual WIMP search run.

To understand the neutron background and the newly observed effects a dedicated study [137] was performed. Data from an Am-Be source (2200 neutrons/s above 1 MeV) calibration run in the 2.3 liter chamber were used. The source was placed on top of the experimental setup between the polyethylene and gamma shieldings. The setup was recreated in a dedicated GEANT4 Monte Carlo simulation to cross-check the results. Events with a F-prompt ≥ 0.7 and $3 \leq S2/S1 \leq 30.0$ were selected as the neutron recoil region. Another surprising result was that the region in the S2/S1 vs F-prompt parameter space attributed to neutrons was different from that of the radon recoils, as pictured in Fig. 6.15. The events coming from nuclear recoils of 222 Rn daughters are selected using the cuts: $0.75 \leq$ F-prompt ≤ 0.97 and $0.4 \leq S2/S1 \leq 5.0$. The sample used in this analysis contained 2200 events in the neutron recoil region out of over 6.5×10^5 triggers.

The light collection efficiency was determined using the dedicated MC simulation, which generated the expected neutron spectrum which in turn was fitted to the experimental spectrum. This procedure resulted in obtaining the light yield value for neutrons of $Y_{nc} = 0.48$ phe/keV, much smaller than in the later, published WIMP run.

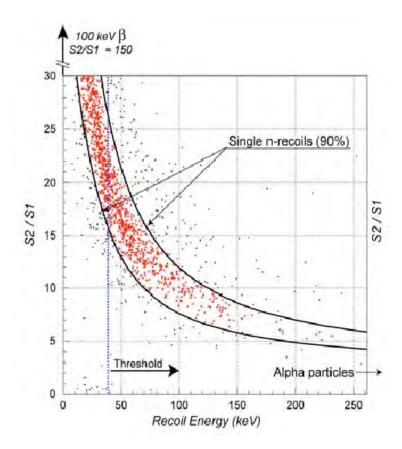


Figure 6.14: The distribution of neutron-recoil signals coming from an Am-Be radioactive source calibration in the S2/S1 vs recoil energy plane. The band encompasses 90% of events, the lowest threshold used in the published analysis is shown [101].

A more detailed look into the neutron bands can be seen in Fig. 6.16, where the neutrons are separated into 1- and 2- hit bands based on the following reasoning: from Eq. (6.1), assuming that the exponential factor is purely an instrumental and not physical effect and so setting it equal to 1, we obtain $S2 = a \cdot S1 + b$. So for each neutron interaction a constant amount of light is registered. Then for a double interaction or n-multiple interaction the factor b will be added twice or n times. Hence in the plot, the 1-hit band signifies events deemed to be single neutron interactions in the liquid phase, while the region above it denotes multiple neutron interactions. This model has been tested via dedicated software used to fit double and multiple interactions. Two versions of the code were created - the main code used by the collaboration performed a Fourier transform of the event waveform. In Fourier space it was easy to deconvolute the effect of the preamplifier integration

with a time constant and then perform the actual fit. Then the fit and the original waveform were transformed back and the results compared. The second, auxiliary code created by the author of this thesis, which performed a semi-analytical fit of the multiple events, mainly focusing on fitting the onset part of the signals. Both codes had a limited functionality, because they could not fit events that were not separated by at least $5\mu s$ of drift time (1 cm of separation in the vertical direction) and were too slow to use in the standard analysis, hence they were used offline and had to be provided with a list of double events obtained firsthand from visual scanning. However, they were still able to aid in the confirmation of the 1-hit/multiple-hit bands scenario, since they allowed a proper fitting of the total S2 signal and returned the result that 15% of the neutron events should be double events fittable by the codes, which agreed quite nicely with the 14% of actual events observed.

It should be noted, that the neutron background will be under much better control in the WArP 100 l detector thanks to the outer VETO detector. The detector is also constructed out of radiopure materials, which substantially lower the background found in the chamber compared to the old 2.3 liter chamber.

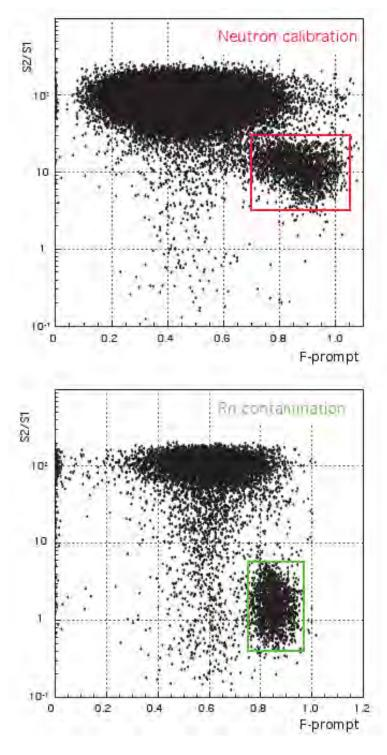


Figure 6.15: The scatter plot of the Am-Be source calibration. The neutron-recoil region and radon-recoil region are inside the rectangles [137].

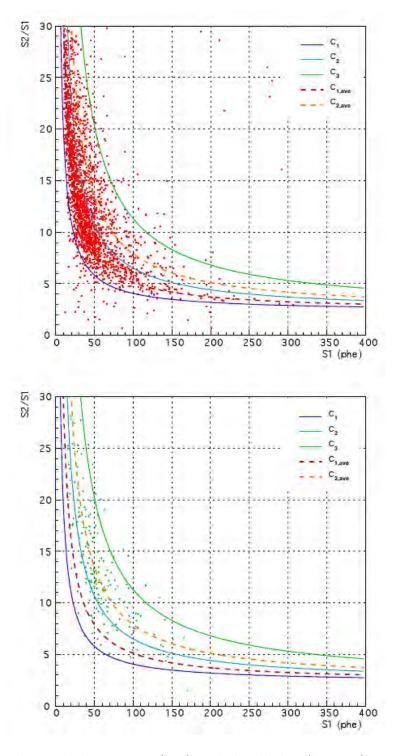


Figure 6.16: The single-hit events (top) and double-hit (bottom) neutron events obtained during the calibration, with the corresponding one-hit (c_1 to c_2) and two-hit (c_2 to c_3) bands. $c_{1,ave}$, $c_{2,ave}$ denote the average values for single hit and double hit bands, respectively [137].

Chapter 7

Annual Modulation Effects Observable in an Argon Detector

It has been mentioned before, that all the direct detection experiments use the halo model to interpret their results. The model generally applied is that of the isothermal sphere of WIMPs [138], called the Standard Halo Model (SHM). This allows a straightforward comparison between experiments if all experiments use this model to calculate their experimental results. It is not clear if the isothermal sphere is how the Dark Matter is actually distributed in our galaxy, and therefore, if the exclusion plots give the actual values of the WIMP-nucleon cross-sections. There are numerous other halo models on the market, some based on N-Body simulations and some evolved from fitting the galaxy rotation curves. There is also quite a lot of papers on how these different models of Dark Matter distribution might affect the results of Dark Matter detectors. It is however very rare, that in these papers an argon detector is considered. For this reason, we find it prudent to try to see how some nonstandard effects would affect the results from the WArP experiment. Here, we will concentrate on some very interesting aspects of the annual modulation effect which, if they could be observed, might lead to valuable insight and provide interesting experimental information. We would like to note, that the idea to observe the Annual Modulation effect in an argon detector, was first proposed by C. Rubbia [139]. We will mostly follow the reasoning found in [94],[140]. A short study of whether mirror Dark Matter could be observed in an argon detector is also included. The calculations presented in this chapter are the sole work of the author of this thesis.

7.1 Dark Matter Detection

As mentioned before, an actual WIMP particle will be detected by registering the recoil energy it will deposit inside a detector. Through kinematic considerations it follows that the energy of an elastic scattering on a target nucleus of mass M_T will be equal to $E = (\mu^2 v^2/M_T)(1-\cos\theta)$, where $\mu = M_T M_W/(M_T + M_W)$ is the WIMP-nucleus reduced mass and v is the speed of the incident WIMP, while θ is the scattering angle in the center of mass frame of the collision.

The most interesting quantity, from the point of view of an actual detector is the so called differential recoil rate, which represents the number of counts per kg, per keV, per day, and is defined as [94]:

$$\Re = \frac{dR}{dE} = \frac{\sigma(q)}{2M_W \mu^2} \rho \, \eta(E, t), \tag{7.1}$$

where q is the momentum transfer, $\sigma(q)$ the WIMP-nucleus cross-section, ρ is the local WIMP density in the halo and $\eta(E,t)$ is the mean inverse speed, which stores the information about the velocity distribution and is defined as follows:

$$\eta(E,t) = \int_{v > v_{min}} \frac{f(u,t)}{u} d^3 u.$$
 (7.2)

Here, v_{min} signifies the lowest incident WIMP speed at which the WIMP could recoil with an energy E and is defined as $v_{min} = \sqrt{\frac{M_T E}{2\mu^2}}$, f(u,t) is the velocity distribution, which in the isothermal sphere model is represented by the Maxwell-Boltzmann distribution. However, this description is correct only in the WIMP halo rest frame. The Earth, and all of the Earth-based Dark Matter detectors with it, is moving with respect to this frame of reference with a speed that is a composition of the rotational speed of the solar neighbourhood around the galactic center, the Sun's peculiar motion in the solar neighbourhood and the rotational velocity of the Earth in its yearly movement around the Sun. When trying to predict experimental results, all of these speeds should be taken into account. The values of these speeds, after performing vector summation, are $v_{\oplus} = 29.8 \text{ km/s}$ for the Earth, and $v_{\odot} = 233.3 \text{ km/s}$ for the Sun, where both the peculiar motion and the rotation around the center of the galaxy have been taken into account. The total speed of the Earth with respect to the WIMP can be approximated as [94]

$$v_{obs}(t) \simeq v_{\odot} \left[1 + b \frac{v_{\oplus}}{v_{\odot}} \cos \omega (t - t_c) \right],$$
 (7.3)

where we have introduced the cosine function to represent the yearly movement of the Earth, t_c is the so called characteristic time, at which the cosine function

peaks. In the case of the WIMPs in the galactic halo, this is equal to $t_c = 0.415$ yr (June 2). A geometric factor b is introduced to take into account the 60^{o} tilt of the Earth's orbit with respect to the Galactic plane, and for an isothermal halo its value is b = 0.49.

Knowing these speeds, the mean inverse velocity can be calculated, and following [94] the results are:

$$\eta(E,t) = \begin{cases} \frac{1}{2N_{esc}\bar{v_o}y} [\operatorname{erf}(x+y) - \operatorname{erf}(x-y) - \frac{4}{\pi}ye^{-z^2}] & \text{for } x < z - y \\ \frac{1}{2N_{esc}\bar{v_o}y} [\operatorname{erf}(z) - \operatorname{erf}(x-y) - \frac{2}{\pi}(y+z-x)e^{-z^2}] & \text{for } z - y < x < z + y \end{cases}$$
(7.4)

where, for clarity, $x = v_{min}/\bar{v_o}$, $y = v_{obs}/\bar{v_o}$ and $z = v_{esc}/\bar{v_o}$. Here $v_{esc} = 650$ km/s is the escape velocity from the halo, $\bar{v_o} = 220$ km/s is the most probable speed from the Maxwellian distribution and $N_{esc} = \text{erf}(z) - 2z \exp(-z^2)/\pi^{1/2}$ is a normalization factor.

7.1.1 Cross-section

The value of $\sigma(q)$ used in Eq. (7.1) is actually composed of the cross-section itself, denoted σ_o and the form-factor which is a result of the fact that the nucleus has finite dimensions, so it is represented as:

$$\sigma(q) = \sigma_o F^2(q) = \sigma_p \left(\frac{\mu}{\mu_p} A\right)^2 F^2(q), \tag{7.6}$$

where we applied the parametrization obtained from the cross-section for scattering on a single nucleon σ_p and μ_p is the reduced mass of a nucleon-WIMP system. In this study we have chosen to use the solid sphere form factor found in [95]. The value of $\sigma_p = 10^{-42}$ cm² was assumed in the following calculations.

7.2 Annual modulation used to determine the WIMP mass

It has already been said in this thesis, that a claim of discovering the annual modulation effect has been made by the DAMA collaboration [82]. Their signal is peaked at June 2^{nd} , as would be generally expected since the cosine function in Eq. (7.3) peaks on that date. However, when studying the modulation effects more closely, additional effects arise, that might put the DAMA result in an interesting light.

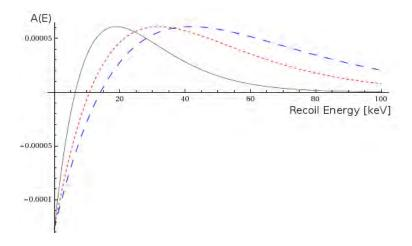


Figure 7.1: The amplitude of the modulation signal for three WIMP masses: 30 (black, solid), 50 (red, dotted) and 70 (blue, dashed) GeV/c^2 in an argon detector. Note that at low energies the amplitude is negative.

The first observation is that when considering the annual modulation, there is a characteristic energy below which the phase of the modulation reverses [140]. This can be observed if we assume that the mean inverse speed η can be written as:

$$\eta(E,t) = B + A\cos(\omega(t-t_c)), \tag{7.7}$$

which is true when $v_{\oplus} \ll v_{\odot}$. We can then plot the value of the A parameter versus energy, as is done for germanium in [140].¹ The safer (and more correct) approach is to use the mean inverse speed obtained from Eq. (7.4), and to calculate the value as in:

$$\eta(E(v_{\odot} + v_{\oplus}), t) - \eta(E(v_{\odot})) = B + A\cos(\omega(t - t_c)) - B = A\cos(\omega(t - t_c)), (7.8)$$

since it is the orbital movement of the Earth, that is responsible for creating the annual modulation. The A obtained in this way for argon is plotted in Fig. 7.1 for 3 masses of the WIMP, i.e. 30, 50 and 70 GeV/c². It can be observed, that for low values of recoil energy the amplitude of the cosine-like oscillations is negative. The point at which the A is equal to zero, and hence, reverses will be called the critical crossover energy E_c . If a Dark Matter detector is sensitive to events below

¹However, their Equation (18) does not reproduce their Fig. 2, apparently because of errors in calculating the A(Q) (our A) parameter. I have tried to contact the corresponding author of article [140], but it seems, he no longer works in physics. It would seem that in this article the A(Q) parameter is missing a factor of 1/2 from Eq. (16) and in Eq. (11) the $\sqrt{2/3}$ is probably reversed [141].

this energy, it should observe the annual modulation peaking in December instead of June at energies below E_c .

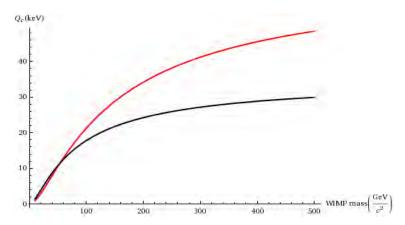


Figure 7.2: The critical crossover energy E_c as a function of WIMP mass for germanium (red) and argon (black).

 E_c depends on both, the mass of the target nucleus and the mass of the WIMP, as was already visible from Fig. 7.1. The full dependence of E_c on the WIMP mass is plotted in Fig. 7.2 for argon and germanium. It can be seen, that the E_c for argon is generally lower, which makes observing the crossover energy harder in argon detectors. Its observation is desirable, because if a detector were to observe both the annual modulation in standard and reversed phase, the obtained crossover energy would allow the determination of the WIMP mass simply using the dependence from Fig. 7.2. This possibility though, obviously depends on the detection threshold of the detector. If E_c happens to be below the lowest energy observable in a detector then only the standard annual modulation can be registered. In this case it is only possible to set an upper limit on the WIMP mass. Incidentally, this leads to a curious situation with the DAMA results, if we assume, that their threshold is 22 keV, as was first declared, using the standard quenching effect. Then their results allow the determination of an upper limit on the WIMP mass (based on the fact that they did not observe modulations in reversed phase). However, as mentioned in Chapter 3, recently the DAMA collaboration has claimed the existence of the channeling effect [93], which results in the lack of nuclear quenching in their detector leading to transforming their energy from keV_{ee} (the ee stands for electron equivalent) to keV. This effect was pursued, because it allowed to lower the energy threshold of DAMA and hence avoid the exclusion claims of other experiments. But, if we take the channeling effect into account, accepting that the low energy threshold of DAMA is of the order of 2 keV then the fact that they did not observe the modulation phase reversal leads to suspect that the WIMP should have a mass of the order of only a few GeV, much lower than all expectations.

In the case of the WArP 100 l detector, the threshold in the inner detector is predicted to be of around 20 keV and in the outer veto of about 30keV (both of these depend on the actual light yield measured in the chamber). The curve in Fig. 7.2 shows that the critical energy doesn't go much higher than 20 keV and only at high WIMP masses at that. It is still possible to calculate the upper mass limit that would be obtained if annual modulation were to be observed in the inner detector of the WArP experiment as well as in the veto. For the inner detector with a threshold of 20 keV the upper mass limit will be $M_{W_{inner}} < 125 \text{ GeV/c}^2$, for the veto detector, where the threshold is expected to be higher, the upper limit on the WIMP mass would be of the order of $M_{W_{veto}} < 510 \text{ GeV/c}^2$. If a very good light yield (of the order of 3 phe/keV) were to be obtained in the inner chamber, an energy threshold of 15 keV might be possible and at this point the sensitivity to WIMP mass would be as low as $M_{W_{15keV}} < 77 \text{ GeV/c}^2$. Let us reiterate that this does not mean that the WArP detector will not be sensible to WIMP masses lower than this, these numbers only represent the limit on the WIMP mass obtainable thanks to observation of an annual modulation effect. It does allow us to say, that the modulation with the phase reversed will not be observed in an argon detector unless the WIMP mass is larger than 125 GeV/c² or measures are taken to lower the energy threshold, i.e. by improving the light yield significantly.

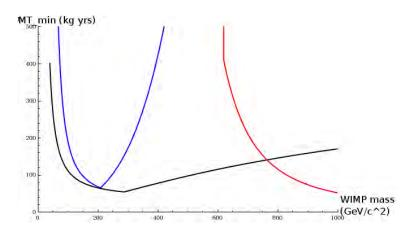


Figure 7.3: The minimum exposure in kg-years required to observe the phase reversal as function of the WIMP mass for the WArP (red), GENIUS-TF (black) and XENON (blue) experiments.

We can still ask the question if an argon detector like WArP could detect the phase reversal, and at what WIMP mass might this be possible. In order to do this the modulation signal must be visible over the total rate observed in the detector. This will require a good enough signal to noise ratio (s/n), where the signal is the modulation and noise the unmodulated WIMP rate. Following [140] we define the signal function as:

$$S(t) = \int_{E_i}^{E_f} \frac{dR}{dE} dE = S_o(E_i, E_f) + S_m(E_i, E_f) + O(S_m^2), \tag{7.9}$$

where S_m is the rate coming from the modulation and S_o is in our case the noise rate. The limits of integration E_i , E_f are the detector threshold and the highest recoil energy expected. The signal to noise ratio, can then be written as:

$$(s/n) = \frac{S_m(E_i, E_f)}{\sqrt{S_o(E_i, E_f)}} \sqrt{MT},$$
 (7.10)

where M is the total detector mass and T is the total exposure time. Note, that we have chosen to calculate S_m explicitly, since using Eq. (21) of [140] leads to a negative signal to noise ratio at low energies. We now require that (s/n) = 2, which results in the modulation signal being 2σ greater than the statistical uncertainty. This allows us to calculate the needed exposure MT in order to observe the annual modulation. However, we need to calculate the signal function in two intervals: (E_i, E_c) and (E_c, E_f) in order to observe both the standard and reversed phase modulation and take the larger of the two as the MT needed to observe a given value of the critical energy E_c . The results of this calculation are plotted in Fig. B, where apart from the predictions for the WArP detector, the expectations for the GENIUS-TF, assuming a threshold of 1 keV, and for XENON, assuming a threshold of 4 keV, are shown for reference. Note that the predictions presented here for GENIUS-TF are substantially higher than those obtained in [140]. This is expected, since we have used a lower value of the cross-section, a slightly different form-factor formula and their η was calculated assuming no escape speed from the halo, i.e. $v_{esc} = \infty$; all this can lead to discrepancies. As expected, because of its high threshold, the WArP detector becomes sensitive to the phase reversal only at high WIMP masses. What is surprising is that at very high masses it is actually better than the GENIUS detector even though WArP has a much higher threshold. This would imply that there are important physics conclusions that can be gained using an argon Dark Matter detector even for higher mass WIMPs. This was not expected before.

7.2.1 The influence of the Sagittarius Stream on the annual modulation expected in an argon detector

The annual modulation signal registered in a detector can become even more complicated if we take into account the fact that the Milky Way is not isolated in the Universe. Galaxy formation simulations and theorems predict that during the course of its life a galaxy undergoes many mergers with neighboring galaxies. Since the Milky Way is not in any way a special case, it is natural to think that such mergers have occurred in its history or that some are even happening currently. These mergers, apart from resulting in the merging of hydrogen gas and other baryonic matter, could in principle create streams of Dark Matter following the baryonic counterparts as tidally stripped tails. This is, naturally, only a hypothesis, but it is interesting to see, what effect these streams might have on the annual modulation signal observed in a Dark Matter detector.

It just so happens that a likely candidate for such a Dark Matter stream exists in the Sagittarius dwarf galaxy, which is being absorbed by the Milky Way [142]. If the baryonic matter is indeed followed by Dark Matter, a cold flow of WIMPs might be registered by the detectors on Earth. The streams of Dark Matter may also result from other astronomical sources and are foreseen by different models of galaxy formation, e.g. the so called late infall model [143]. Here, however, we will limit our study to that of the Sagittarius stream, as it gives a good idea on how the annual modulation might be affected by infalls of Dark Matter not coming from the galactic halo.

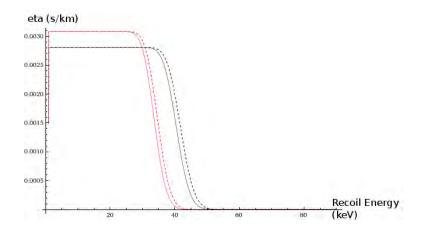


Figure 7.4: The mean inverse speed $\eta(E)$ for the Sagittarius stream, assuming a velocity dispersion $\sigma_v = 25$ km/s for December (black) and June (red) for germanium (dashed line) and argon (solid line). Note, that the mean inverse speed is constant in energy until a certain cutoff, which can result in a rate of events much different from that expected from the Standard Halo Model.

The Sagittarius stream, if it exists in the form of Dark Matter particles, is falling on the galactic disk from the direction of the North Galactic Pole (which is located above the center of the galaxy on the perpendicular axis going through

the disk). It is moving at approximately (300 ± 90) km/s relative to the galactic rest frame and its relative speed towards an observer in the solar system is about 340 km/s. What is important when considering streams is that their velocity dispersion is usually much smaller than that of the galactic halo. If we assume it to be zero, then the mean inverse speed will become a step function until a certain cutoff energy, which in the case of argon was calculated to be 37 keV. If we allow the velocity dispersion to be nonzero, then the general behaviour remains, but the cutoff energy is softened. The mean inverse speeds calculated for the Sagittarius stream in argon and germanium detectors are presented in Fig. 7.4. The $\eta(E,t)$ is calculated for the characteristic time of the Sagittarius stream, which is 0.991 yr (Dec 28) and for half a year afterwards, the velocity distribution is assumed to be $\sigma_v = 25$ km/s. It is worth noting that above the cutoff energy no events will be observed, of course this is relaxed via the velocity dispersion. Also near this energy, it is possible, that in December events would be detected while around June none would be seen. This shows that a yearly signature for a Dark Matter stream can sometimes be very far from a cosine function. Also, because the η is constant in energy, this can lead to disproportionately large effects considering the much smaller density of the stream (in these calculations it is assumed that $\rho_S = 0.05 \rho_{SHM}$) especially near the cutoff energy. In the following plots the energy, at which the curves are plotted is 35 keV, unless stated otherwise.

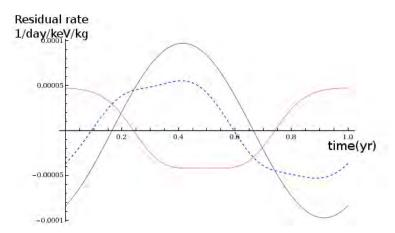


Figure 7.5: The annual modulation rate expected from the Standard Halo Model (black curve), along with the modulation expected from the Sagittarius stream assuming a velocity dispersion $\sigma_v = 25$ km/s (red curve), the WIMP density $\rho_S = 0.05 \ \rho_{SHM}$. Both curves are calculated for the recoil energy of 35 keV. The sum of these two effects is also plotted (blue curve).

In Fig. 7.5 the annual modulation signal for an argon detector is shown for a

recoil energy of 35 keV (just below the cutoff energy, where the effects of the stream are the strongest), together with the signal expected from the Sagittarius stream, as well as the sum of both. A velocity dispersion of $\sigma_v = 25$ km/s was assumed for the stream. Contrary to [94], we have chosen not to plot the expectation for 10 keV since this energy is well below the threshold of the WArP detector. It can be observed that the resulting modulation signal will only roughly resemble a cosine function, expected from a clean modulation effect.

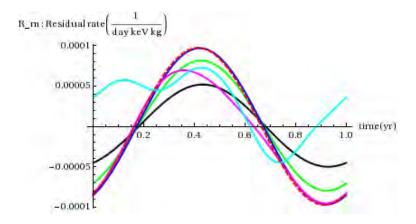


Figure 7.6: The annual signal as expected from the Standard Halo Model together with the addition of the Saggitarius effect at different recoil energies. The black, green, blue, magenta and cyan curves correspond to 17, 22, 27, 32, 37 keV of recoil energy, respectively. The unmodified curve (red) coming from only the halo contribution is also shown for reference.

It is interesting to see, if the effects of the stream in the case of argon are similar to those of a germanium detector. For this reason we will follow the methodology found in [94], and see what happens when some parameters of the Sagittarius stream are varied. We will limit ourselves only to the Sagittarius stream, however. The first thing to understand is how the Sagittarius stream would affect the modulation found in an argon detector at different energies. Such a plot can be found in Fig. 7.6. It is clear that at energies close to the cutoff energy, the effect of the Sagittarius stream becomes dominant.

The next parameter that can vary in a Dark Matter stream is the variance of velocity. The corresponding plots can be found in Fig. 7.7. The results lead to the conclusion that especially at low values of the velocity dispersion, the annual modulation signal has a form that largely deviates from the cosine function. This is understandable, since at small dispersions the η practically becomes a step function and the modulation is replaced by a situation of observing events (December) and not observing events (June).

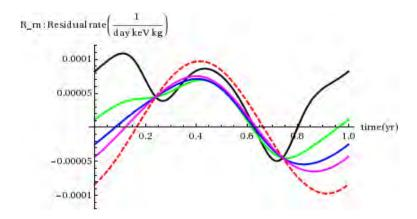


Figure 7.7: The annual signal as expected from the Standard Halo Model together with the addition of the Saggitarius effect at different velocity dispersions of the stream. The black, green, blue and magenta curves correspond to 12.5, 25, 37.5, 50 km/s respectively. The unmodified curve (red) coming from only the halo contribution is also shown for reference.

The next effect that we examine here is the energy binning that would be found in a detector. This effect comes from the actual detector response and means that the energy which is registered is not always the deposited energy. This depends on the energy resolution of the detector. The average recoil rate,

$$\langle R \rangle = \frac{1}{\Delta E} \int_{E_c - \Delta E/2}^{E_c + \Delta E/2} R(E) dE$$
 (7.11)

is shown in Fig. 7.8, for both the Sagittarius stream and the Standard Halo, for the critical energy, the velocity dispersion $\sigma_v = 25$ km/s and for the stream density equal to 0.05 ρ_{halo} . The bins in ΔE shown here are from 1 keV to 9 keV. A large departure from cosine like function is visible already for the 1 keV energy bin and grows with bin width.

The last parameter that we can vary is the stream density. Fig. 7.9 shows the variation of the total annual signal when the Sagittarius stream density is varied from 0.01 to 0.09 of the 0.3 GeV c⁻² cm⁻³ used for the isothermal halo. As expected for the lowest densities the stream effect is almost negligible, but for higher values the function becomes highly asymmetric and the Sagittarius component plays an important part.

As result of this study a few conclusions can be drawn. As in [94], we find it possible that if a Dark Matter stream following the Sagittarius galaxy exists it should be observable in the annual modulation signal, which is not the case in the DAMA results. Specifically, the changes in the annual WIMP rate in a detector

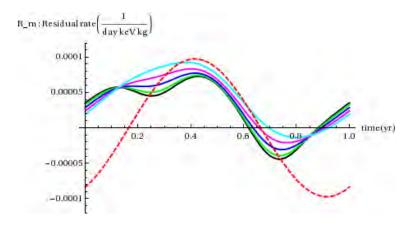


Figure 7.8: The annual signal as expected from the Standard Halo Model together with the addition of the Saggitarius effect at different energy binning in the detector. The black, green, blue, magenta and cyan curves correspond to 1, 3, 5, 7, 9 keV bin widths respectively. The unmodified curve (red) coming from only the halo contribution is also shown for reference.

need not be cosine like, and need not peak at June 2. A very important result of this study is that an argon detector, specifically the WArP 100 liter detector, is fully capable of registering effects coming from the Sagittarius stream and could be used as a tool in future WIMP astronomy studies, provided the WIMP is first detected.

7.3 Mirror Matter

It has been speculated [64], that the Dark Matter riddle could be solved not by the WIMP model, but by the so called Mirror Matter. This idea has gained some momentum in recent years since it is able to explain the discrepancy between the DAMA results and the experiments claiming to rule it out [144]. The concept of Mirror Matter is quite old, and has been proposed to conserve parity as a symmetry of nature, when it was discovered that in the framework of the particles that were known at the time it is broken maximally by weak interactions. It was proposed that for each particle of the Standard Model a mirror particle exists that has identical properties except for opposite parity. Then, as a whole parity would be conserved. The result of this addition is that the mirror particles interact weakly with the known ones, mainly via neutral particle (photon or neutron) [145] which oscillates between its normal and mirror states. There is also speculation that Mirror Matter should have undergone an evolution similar to known matter and so, a mirror nucleosynthesis has occurred and mirror atoms exist. If an asymmetry

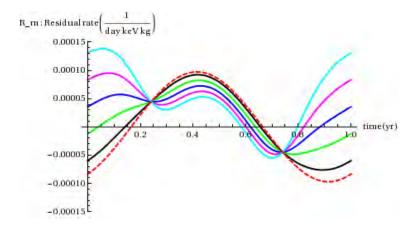


Figure 7.9: The annual signal as expected from the Standard Halo Model together with the addition of the Saggitarius effect at different densities of the stream. The black, green, blue, magenta and cyan curves correspond to 0.01, 0.03, 0.05, 0.07, 0.09 ρ_{SHM} , respectively. The unmodified curve (red) coming from only the halo contribution is also shown for reference.

is assumed in the initial conditions it is possible for mirror matter to play the role of Dark Matter, and the most important particle from the detection point of view should be the mirror oxygen O'. It could explain the interactions in the DAMA experiment, thanks to the higher energy transfer to low mass sodium atoms, while such transfer to, for example, germanium would be much more suppressed [146]. Since low mass of the detector atoms is cited as a positive factor in the searches for Dark Matter, it is possible that an argon detector, with its relatively light mass atoms, might be a good candidate to test the Mirror Matter hypothesis.

For this calculation, we assume that mirror oxygen is indeed the most abundant particle in the mirror halo (apart from mirror helium and mirror hydrogen which would not be detectable due to kinematic considerations), and following [146] we try to calculate the event rate in an argon detector based on the DAMA rate. Following the reasoning in [146] we first calculate the minimal speed of the O' atoms in the halo, that will allow them to overcome the energy threshold of the detector using the equation:

$$v'_{min}(E_R) = sqrt(\frac{(M_A + M_{A'})^2 E_R}{2M_A M_{A'}^2}),$$
 (7.12)

where M_A and $M_{A'}$ are the mass of the detector atom and mirror atom, respectively and E_R is the detector threshold energy. In an argon detector with a threshold of 20 or 30 keV the minimal speed that a mirror oxygen atom should have in order to be registered would be 525 or 643 km/s respectively, so rather high in terms of expected WIMP speeds. It is much higher than the corresponding speeds for the DAMA detector (290 km/s) and even for the CDMS germanium detector (450 km/s), which has higher mass target atoms, but gains a lot due to its lower energy threshold set at 10 keV. However, in the case of mirror atoms the speeds of the particles in the Dark Matter halo are not cut off like for WIMPs. This is caused by the fact, that mirror particles interact among themselves much more often than WIMPs and hence for mirror particles the mean free path in the galactic medium is shorter than the size of the galaxy [146]. For this reason, the mean inverse speed, should be calculated with an upper limit of infinity, and mirror atoms with even very large speeds can be found in the halo. The calculated η is equal to [146]:

$$\eta(E) = \frac{1}{2v_0 y} [\operatorname{erf}(x+y) - \operatorname{erf}(x-y)], \tag{7.13}$$

where v_0 is the most probable speed for a mirror Dark Matter atom, which is different for each atom, and if we assume, that the halo is dominated by mirror helium, as is suggested by mirror BBN arguments [147], then $v_0(A') = v_0(He')\sqrt{M_{He'}/M_{A}}$; where we assume $v_0(He') = 220$ km/s. The interaction rate is calculated similarly as for the WIMP case:

$$\frac{dR}{dE} = \sum_{A'} N_T n_{A'} \frac{\lambda}{E^2} \eta(E), \qquad (7.14)$$

where the λ/E factor is related to the cross-section and λ is equal to:

$$\lambda = \frac{2\pi\epsilon^2 \alpha^2 Z^2 Z'^2}{M_A} F_A^2(qr_A) F_{A'}^2(qr_{A'}). \tag{7.15}$$

In the above equations N_T is the number of atoms in a kg of detector, $n_{A'}$ is the A' mirror atom number density, $\epsilon = 5 \times 10^{-9}$ is the effective charge of the mirror matter coupling [146], α is the fine structure constant, M_A is the detector atom mass and F_A and $F_{A'}$ are the form factors for the detector and halo mirror nucleus, respectively. If we calculate the actual rate that would be seen in an argon detector due to a mirror oxygen dominated halo (again taking into account only atoms heavier than mirror helium), the resulting rate per day, per keV, per kg of detector is plotted in Fig. 7.10. Most events have a recoil energy below 20 keV. Therefore the WArP detector with a threshold of 20 keV will not be sensitive to mirror Dark Matter as the observed rate would be less than 10^{-4} events per day, resulting in less than one event per year. Hence the current null results of the WArP detector are in agreement with the Mirror Matter scenario, but they do not allow to put any limits on its properties, nor will the results from the 100 l detector.

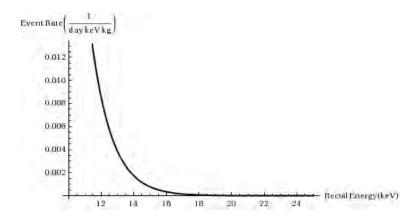


Figure 7.10: The differential event rate in an argon detector due to interactions with mirror oxygen, assuming an O' dominated mirror halo.

Chapter 8

Conclusions

This thesis is a summary of the work done by the author in the framework of the research and development of the WArP experiment (Chapter 5), as well as using the small WArP detector in an actual WIMP search (Chapter 6). As already mentioned, the research and development work was part of the larger programme that led to the construction of the 100 liter detector. Now (April 2009), the 100 liter detector is in its last phase of commissioning and should begin operation within weeks. It should be a big step forward in the searches for Dark Matter particles. This is illustrated in Fig. 8.1 where the predictions for the WArP 100 l detector are shown for 100 days of data taking assuming it will find no events.

One should note, that the WArP 100 l detector can increase the sensitivty, as compared to the currently leading experiments, by about two orders of magnitude in the most interesting region of the WIMP parameters predicted as very probable by theoreticians (see Fig. 8.1). A better understanding of the acquired data will be needed, and so studies of the influence of halo models will be pursued with even more attention. Chapter 7 is an example of such a study. A work to ascertain the absolute event rates depending on halo models has already been started by the author of this thesis.

One can expect that the nearest months will bring some very interesting results in a very interesting field that is Dark Matter searches. This will be both due to the direct detection experiments, like WArP and XENON 100 and to indirect detection experiments like GLAST and PAMELA. One can also hope that the LHC will soon start taking data and provide valuable input.

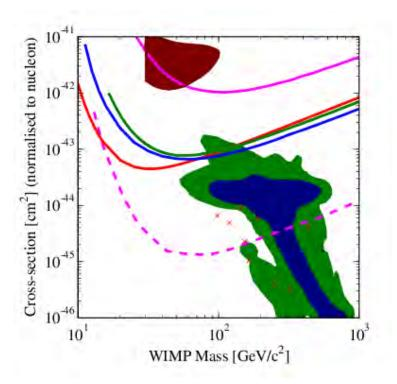


Figure 8.1: The predictions for 100 days of data taking for the WArP 100 liter detector (pink dashed line), assuming no background events are found in the chamber, compared with the current experimental situation for direct detection experiments. The brown area is the WIMP preferred by the DAMA result, the lines present exclusion plots for the CDMS (blue), XENON (red), ZEPLIN(green) and WArP 2.3 l (pink) experiments. The blue and green areas and the red crosses are theoretical predictions. Plot from [84].

Appendix A

Glossary

ADC Analog to Digital Converter

BBN Big Bang Nucleosynthesis

CMB Cosmic Microwave Background

CMSSM Constrained Minimal Supersymmetric Model

DAQ Data Acquisition

ENDF Evaluated Nuclear Data File

FPGA Field-Programmable Gate Array

GUI Graphical User Interface

ΛCDM Lambda Cold Dark Matter

LET Linear Energy Transfer

LKP Lightest Kaluza-Klein Particle

LSP Lightest Supersymmetric Particle

MCA Multi Channel Analyzer

MOND MOdified Newtonian Dynamics

MSSM Minimal Supersymmetric Model

mSUGRA Minimal Super Gravity

 \mathbf{MySQL} Open source database framework using SQL (Structured Query Language)

 ${f PMT}$ Photomultiplier

ppm parts per million

QDC Charge to Digital Converter

 ${\bf SER}\,$ Single Electron Response

VUV Vacuum Ultraviolet, usually below 200 nm wavelength

WArP WIMP Argon Programme

WIMP Weakly Interacting Massive Particle

Appendix B

Errata

While revisiting the calulations that lead to Fig. a numerical error was found which was not found before since it occurred in both elements of a ratio calculated for the plot, so the smooth behaviour of the calculated curves did not signal the error. Once corrected, the plot should look as in Fig. B.1. The optimistic previsions of using argon to determine the WIMP mass based on the annual modulation effect are much less so. However, the observation that argon is better suited to observe this effect at higher masses than xenon remains. Unfortunately, to observe this effect in argon one would need about 10 years of observation with an experiment with a fiducial volume of about 8 tons, as in Fig. B.2. Which means that this effect is probably not observable for the ArDM experiment even if it were able to go down with the energy threshold down to 20 keV. These previsions for argon become much more reasonable if an argon experiment would be able to achieve a lower threshold, for example 15 keV (orange curve). At this point an argon detector can again be competitive in the search for the phase reversal effect, however this would probably mean waiting for the next after generation of experiments.

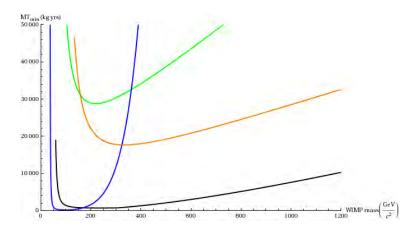


Figure B.1: The corrected minimum exposure in kg-years required to observe the phase reversal as function of the WIMP mass for the WArP (red with a threshold at 20keV, orange with a threshold at 15 keV), CDMS (black - germanium, green - silicon) and XENON (blue) experiments.

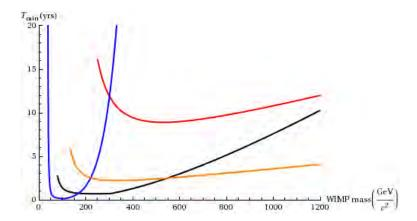


Figure B.2: The minimum exposure in years required to observe the phase reversal as function of the WIMP mass for the next after next generation experiments - an 8 ton argon experiment (red with a threshold at 20keV, orange with a threshold at 15 keV), a 1 ton germanium experiment (black) and a 1 ton xenon (blue) experiment.

Acknowledgements

I would like to thank my supervisor, prof. Agnieszka Zalewska, who has given me the opportunity to work in a great experiment and has supported my thesis all the way up to the final corrections. I would also like to ackowledge her ongoing efforts to promote my work in various circles and thank her for all the help and kind words during the course of my studies.

I wish to thank prof. Carlo Rubbia for allowing me to enter the WArP collaboration and work in the wonderfully interesting field of Dark Matter detection.

I would like to thank the President of the Polish Academy of Sciences Andrzej Legocki and his successor Michal Kleiber for funding and providing the PhD scholarship which I had the honor to receive.

I cordially thank professors Flavio Cavanna and Gianni Piano-Mortari for making it possible for me to spend a year at the University of L'Aquila, dott-ssa Giuliana Fiorillo for allowing me to spend time at the University of Naples and prof. Marco Roncadelli for inviting me to Pavia. These stays allowed me to gain invaluable experience.

I would like to express my gratitude to prof. Flavio Cavanna, prof. Ornella Palamara, prof. Claudio Montanari, prof. Marco Roncadelli, dott-ssa Giuliana Fiorillo and dott. Alfredo Cocco for the advice and help I received during my work in the WArP experiment.

I am grateful to prof. Kacper Zalewski and prof. Flavio Cavanna for reading parts of this thesis and for their helpful suggestions.

I am indebted to Luca Grandi, for his help and discussions during my stay in Italy and while finishing this thesis.

I want to thank my colleagues from the Gran Sasso laboratory for their hospitality and friendship and helping me feel at home in Italy. My special thanks go to Roberto Acciarri, Maddalena Antonello, Nicola Canci, Francesco Di Pompeo, Luciano Pandola, Ettore Segreto, Chiara Vignoli and again, Luca Grandi.

I would also like to thank prof. T. Lesiak and dr hab. A. Horzela who kindly helped me overcome formal problems during the course of my studies.

Last but not least, I would like to thank my mother who believed in me even when I did not and to Zosia whose smile helped me when I needed it the most.

This work was in part supported by MNiSW grants 1P03B04130 and NN202061531.

Bibliography

- [1] L. Bergstrom, A. Goobar, "Cosmology and Particle Physics", Chichester (UK), John Wiley & Sons, (1999).
- [2] E. W. Kolb and M. S. Turner, The Early Universe, Redwood City, CA: Addison-Wesley, (1990).
- [3] J. Lesgourgues, "An overview of Cosmology", Lecture notes for the Summer Students Programme of CERN (2002-2004), arXiv:astro-ph/0409426v1.
- [4] G. Hinshaw et al. Astrophys.J.Suppl.180:225-245,(2009), arXiv:0803.0732v2 [astro-ph].
- [5] http://lambda.gsfc.nasa.gov/product/map/current/m_images.cfm
- [6] W. Hu, "Lecture Notes on CMB Theory: From Nucleosynthesis to Recombination", to appear in XIX Canary Island Winter School of Astrophysics, ed. R. Rebelo and J.A. Rubino-Martin, arXiv:0802.3688v1.
- [7] G Steigman Annu. Rev. Nucl. Part. Sci, 57: 463-491 (2007).
- [8] F. Iocco, G. Mangano, G. Miele, O. Pisanti, PD Serpico, "Primordial Nucleosynthesis: from precision cosmology to fundamental physics", arXiv:0809.0631.
- [9] M.M. Phillips: Astrophys. J. Lett. 413, L105 (1993),
 A. G. Riess, W. H. Press, and R. P. Kirshner. Astrophys. J., 473:1, 88-109 (1996),
 S. Perlmutter, S. Gabi, G. Goldhaber, et al., Astrophys. J., 483, 565 (1997).
- [10] S. Perlmutter et al., B.A.A.S., 29, 5, 1351 (1997), http://supernova.lbl.gov/
- [11] A. G. Riess, et al., AJ, 116, 1009 (1998), arXiv:astro-ph/9805201.
- [12] A. G. Riess et al., Astrophys. J., 659, 1, 98-121 (2007).

- [13] N.W. Boggess et al., Astrophys. J., 397 (2): 420, (1992).
- [14] M. Colless et al., Mon. Not. R. Astron. Soc. 328, 10391063 (2001).
- [15] D.G. York et al., Astron. J. 120, 15791587 (2000).
- [16] W. J. Percival et al., Astrophys.J. 657, 645-663, (2007).
- [17] F. Zwicky, Helv. Phys. Acta, 6, 110, (1933).
- [18] S. Smith, Astrophys. J., 83, 23, (1936).
- [19] F.D. Kahn & L. Woltjer, Astrophys. J.,130, 705, (1959).
- [20] H.W. Babcock, Lick Obs. Bull, 498, 41, (1939).
- [21] J. H. Oort, Astrophys. J., 91, 273, (1940).
- [22] V. C. Rubin, W. K. Ford & N. Thonnard, Astrophys. J. 225, L107, (1978).
 V. C. Rubin, W. K. Ford & N. Thonnard, Astrophys. J. 238, 471, (1980).
- [23] A. Klypin, H. Zhao, R. S. Somerville, Astrophys.J.573:597-613 (2002), arXiv:astro-ph/0110390v1.
- [24] J.P. Ostriker & P.J.E. Peebles, Astrophys. J. 186,467, (1973),
 J.P. Ostriker, P.J.E. Peebles & A. Yahil, Astrophys. J., 193, L1, (1974).
- [25] J. Einasto, A. Kaasik & E. Saar, Nature, 250, 309, (1974).
- [26] R. Cowsik & J. McClelland, Astrophys. J., 180, 7, (1973),
 A. S. Szalay & G. Marx, Astron. Astrophys., 49, 437, (1976),
 M. Rees, in "Evolution of Galaxies and Stellar Populations", ed. B. M. Tinsley & R. B. Larson, New Haven, Yale Univ. Obs., p. 339, (1977).
- [27] A.D.Chernin, Astron. Zh. 58, 25, (1981).
- [28] G. F. Smoot, M. V. Gorenstein, R. A. Muller, Phys. Rev. Let., 39, 898-901, (1977).
- [29] G.R. Blumethal, S.M. Faber, J.R. Primack & M.J. Rees, Nature 311, 517, (1984).
- [30] M. Davis, G. Efstathiou, C.S. Frenk & S.D.M. White, Astrophys. J. 292, 371-394 (1985).
- [31] V. Springel et al., Nature 435, 629-636 (2005).

- [32] M. J. Geller & J. P. Huchra, Science, 246, 897903 (1989).
- [33] V. Springel, C.S. Frenk and S.D.M. White, Nature, 440, 1137-1144 (2006).
- [34] S. Gottloeber, G. Yepes, C. Wagner and R. Sevilla, "The MareNostrum Universe", arXiv:astro-ph/0608289v1,
 S. Gottloeber, G. Yepes, A. Khalatyan, R. Sevilla and V. Turchaninov, AIPConf.Proc.878:3-9, (2006), arXiv:astro-ph/0610622v2.
- [35] J. R. Bond, L. Kofman & D. Pogosyan, Nature, 380, 603 (1996).
- [36] N. Kaiser, Astrophys. J. 388, 272286 (1992).
- [37] J. E. Gunn, Astrophys.J. 150, 737 (1967).
- [38] L. Fu et al., A&A 479, 925 (2008).
- [39] M. Hetterscheidt, et al., A&A 468, 859 (2007),
 H. Hoekstra, K. C. Yee H. and M. D. Gladders, ApJ 577, 595 (2002),
 L. VanWaerbeke, et al., Astroparticle Physics 26, 91 (2006).
- [40] D. Clowe, S. W. Randall, M. Markevitch, Nucl.Phys.Proc.Suppl.173:28-31 (2007) arXiv:astro-ph/0611496v1,
 D. Clowe, A.H. Gonzalez, & M. Markevitch, ApJ, 604, 596 (2004),
 Douglas Clowe et al., Astrophys.J., 648,L109-L113,2006 arXiv:astro-ph/0608407v1.
- [41] http://flamingos.astro.ufl.edu/1e0657/public.html .
- [42] W. J. G. de Blok, S. S. McGaugh, A. Bosma & V. C. Rubin, Astrophys. J. 552, L23L26 (2001).
 E. Hayashi et al., Mon. Not. R. Astron. Soc. 355, 794812 (2004).
- [43] J. S. Bullock, A. V. Kravtsov & D. H. Weinberg, Astrophys. J. 548, 3346 (2001).
- [44] A. J. Benson, C. S. Frenk, C. G. Lacey, C. M. Baugh, & S. Cole, Mon. Not. R. Astron. Soc. 333, 177190 (2002).
- [45] Kochanek, C. S. & Dalal, N. Tests for Substructure in Gravitational Lenses. Astrophys. J. 610, 6979 (2004).
- [46] J. Jalocha, L. Bratek, M. Kutschera, Astrophys.J.,679,373-378 (2008), arXiv:astro-ph/0611113v3.
- [47] M.J. Disney et al., Nature, 455, 7216, 1082-1084 (2008).

- [48] A. Blanchard, M. Douspis, M. Rowan-Robinson, & S. Sarkar, A & A 412, 3544 (2003).
- [49] M. Milgrom, Astrophys. J., 270, 365, (1983),M. Milgrom, Astrophys. J., 270, 371 (1983).
- [50] A. Aguirre, J. Schaye & E. Quataert, Astrophys. J. 561, 550558 (2001),
 R.H. Sanders, Mon. Not. R. Astron. Soc. 342, 901-908, (2003).
- [51] C. Skordis, D. F. Mota, P. G. Ferreira, C. Boehm, Phys.Rev.Lett.96:011301 (2006), arXiv:astro-ph/0505519v2,
 Scott Dodelson, Michele Liguori Phys.Rev.Lett.97:231301 (2006), arXiv:astro-ph/0608602v1,
 F. Bourliot, P. G. Ferreira, D. F. Mota, C. Skordis Phys.Rev.D75:063508 (2007), arXiv:astro-ph/0611255v2.
- [52] J. D. Bekenstein, Physics Letters B202, 497 (1988).
 - J. D. Bekenstein, in Developments in General Relativity, Astrophysics and Quantum Theory, F. I. Cooperstock, L. P. Horwitz and J. Rosen, eds. (IOP Publishing, Bristol 1990), p. 156,
 - J. D. Bekenstein, in Proceedings of the Sixth Marcel Grossman Meeting on General Relativity, H. Sato and T. Nakamura, eds. (World Scientic, Singapore 1992), p. 905.
- [53] J.D. Bekenstein, Phys. Rev. D 70, 083509 (2004).
- [54] G. W. Angus, B. Famaey, HongSheng Zhao, Mon.Not.Roy.Astron.Soc., 371, 138 (2006), arXiv:astro-ph/0606216v1.
- [55] P. D. Mannheim, General Relativity and Gravitation 22, 3, 289 (1990).
- [56] J. W. Moffat, Journal of Cosmology and Astroparticle Physics, 03, 004, (2006).
- [57] S. P. Martin, "A Supersymmetry Primer", arXiv:hep-ph/9709356v5.
- [58] M. Shiozawa et al., Phys. Rev. Lett. 81, 3319 (1998),K. Kobayashi et al., Phys. Rev. D72, 052007 (2005).
- [59] G. Servant & T. M. Tait, Nucl. Phys. B 650, 391 (2003) [arXiv:hep-ph/0206071].
- [60] G. Bertone, D. Hooper, J. Silk, Phys.Rept.405,279-390 (2005), arXiv:hep-ph/0404175v2.

- [61] R. D. Peccei & H. R. Quinn, Phys. Rev. Lett. 38, 1440, (1977).
- [62] L. J. Rosenberg and K. A. van Bibber, Phys. Rept. 325, 1 (2000).
- [63] R. Battesti et al. Lect.NotesPhys.741,199-237 (2008), arXiv:0705.0615v1.
- [64] R. Foot, Int.J.Mod.Phys.D13,2161-2192 (2004), arXiv:astro-ph/0407623v1.
- [65] See, e.g., H. E. Haber and G. L. Kane, Phys. Rept. 117, 75 (1985).
- [66] G.L. Kane, C. Kolda, L. Roszkowski and J.D. Wells, Phys. Rev. D 49, 6173 -6210 (1994).
- [67] See, e.g., H. P. Nilles, Phys. Rept. 110, 1 (1984), A. Brignole, L. E. Ibanez and C. Munoz, Soft supersymmetry breaking terms from supergravity and superstring models, published in Perspectives on Supersymmetry, ed. G. L. Kane, 125, arXiv:hep-ph/9707209v3.
- [68] L. Roszkowski, R. Ruiz de Austri, R. Trotta, JHEP0707, 075 (2007), arXiv:0705.2012v2.
- [69] F. J. Petriello, K.M. Zurek, JHEP0809,047 (2008), arXiv:0806.3989v3.
- [70] A. Bottino, F. Donato, N. Fornengo, S. Scopel, Phys.Rev.D68:043506 (2003), arXiv:hep-ph/0304080v2.
- [71] J. Ellis, K.A. Olive, Y. Santoso, V.C. Spanos, Phys. Lett. B 565, 176-182 (2003).
- [72] J. P. Miller, E. de Rafael & B. L. Roberts, Rept. Prog. Phys. 70, 795 (2007). arXiv:hep-ph/070304,
 - E.A. Baltz, P.Gondolo, Phys. Rev. D 67, 063503 (2003), arXiv:astro-ph/0207673,
 - R. Arnowitt, B. Dutta, B. Hu, plenary talk at Beyond The Desert '03, Castle Ringberg, Germany, June 9, (2003), arXiv:hep-ph/0310103v2.
- [73] H.Baer, A. Mustafayev, E.-K. Park, X. Tata, JHEP0805, 058 (2008),
 arXiv:0802.3384v2 H. Baer, C. Balazs, A. Belyaev, T. Krupovnickas, J. O'Farril, JCAP 0408, 005 (2004), arXiv:hep-ph/0405210v3
- [74] H. Baer, C. Balazs, A. Belyaev, T. Krupovnickas, X. Tata, JHEP 0306, 054 (2003), arXiv:hep-ph/0304303v2
- [75] W. de Boer, C. Sander, V. Zhukov, A.V. Gladyshev, D.I. Kazakov Astron. Astrophys. 444, 51 (2005), arXiv:astro-ph/0508617v1.

- [76] A.W. Strong, I.V. Moskalenko & O. Reimer, Astrophys. J., 537, 763 (2000),[Erratum-ibid. 541, 1109], arXiv:astro-ph/9811296.
- [77] O. Adriani et al., Nature 458, 607-609 (2009), arXiv:0810.4995v1.
- [78] V. Barger, W.-Y. Keung, D. Marfatia, G. Shaughnessy Phys.Lett.B672:141-146 (2009) arXiv:0809.0162v2 [hep-ph], Marco Cirelli, Mario Kadastik, Martti Raidal, Alessandro Strumia, "Model-independent implications of the e+, e-, anti-proton cosmic ray spectra on properties of Dark Matter" IFUP-TH/2008-27, SACLAY-T08/139, arXiv:0809.2409v3 [hep-ph].
- [79] J. Chang et al., Nature 456, 362-365 (2008).
- [80] O. Adriani et al., Phys. Rev. Lett. 102, 051101, (2009), arXiv:0810.4994v1.
- [81] R. Bernabei et al., Eur.Phys.J.C56:333-355 (2008), arXiv:0804.2741v1.
- [82] R. Bernabei et al., Phys. Lett. B480, 23-31, (2000).
- [83] D. S. Akerib et al. [CDMS Collaboration], Phys. Rev. D 68, 082002 (2003), arXiv:hep-ex/0306001,
 - Z. Ahmed et al. [CDMS Collaboration], Phys.Rev.Lett.102:011301 (2009), arXiv:0802.3530 [astro-ph],
 - D. S. Akerib et al. [CDMS Collaboration], Phys. Rev. Lett. 96, 011302 (2006), arXiv:astro-ph/0509259.
- [84] http://dendera.berkeley.edu/plotter/entryform.html
- [85] J. Angle et al., Phys. Rev. Lett. 100, 021303 (2008), arXiv:0706.0039.
- [86] G.J. Alner, Astropart. Phys. 28, 287-302 (2007), arXiv:astro-ph/0701858v2.
- [87] WArP proposal, warp.lngs.infn.it/proposal.pdf
- [88] M. Laffranchi, A. Rubbia, The ArDM project: a Liquid Argon TPC for Dark Matter Detection, arXiv:hep-ph/0702080v1.
- [89] J.A. Nikkel, W. H. Lippincott, D. N. McKinsey, Nuclear Physics B (Proc. Suppl.) 143, 556 (2005).
- [90] S. Cebrin et al., New Journal of Physics 2, 13.1-13.20 (2000).
- [91] The UK Dark Matter Collaboration Phys.Lett.B616:17-24 (2005), arXiv:hep-ex/0504031v1.

- [92] J. Lee, AIP Conference Proceedings, Volume 878, pp. 106-110 (2006),
 S.S. Myung et al., AIP Conference Proceedings, Volume 1078, pp. 533-535 (2008).
- [93] R. Bernabei et al. (DAMA Collaboration), Eur. Phys. J. C. 53, 205 (2008), arXiv:0710.0288 (2007).
- [94] Chris Savage, Katherine Freese, Paolo Gondolo Phys.Rev.D74:043531 (2006), arXiv:astro-ph/0607121v2.
- [95] J. D. Lewin, P. F. Smith, Astroparticle Physics 6, 87-112 (1996).
- [96] A. Hitachi et al. Phys. Rev. B, 27, 5279 (1983), and references therein.
- [97] T. Doke et. al. Nucl. Instr. and Meth. A 269, 1, 291-296 (1988).
- [98] J. A. Nikkel, R. Hasty, W. H. Lippincott, D. N. McKinsey, Astropart.Phys.29:161-166 (2008), arXiv:astro-ph/0612108.
- [99] Icarus Collaboration, ICARUS I: An Optimized Real Time Detector of Solar Neutrinos, Experiment Proposal, LNF-89/005(R), (1989)
 - P. Benetti et al., Nucl. Instr. and Meth. A 332, 395 (1993),
 - P. Cennini et al., Nucl. Instr. and Meth. A 333, 567 (1993),
 - P. Cennini et al., Nucl. Instr. and Meth. A 345, 230 (1994),
 - P. Cennini et al., Nucl. Instr. and Meth. A 432, 240 (1999),
 - F. Arneodo et al., Nucl. Instr. and Meth. A 449 36 (2000),
 - F. Arneodo et al., Nucl. Instr. and Meth. A 449, 42 (2000),
 - F. Arneodo et al., Nucl. Instr. and Meth. A 498, 292 (2002).
- [100] P. Bennetti et al. (A.M. Szelc) Nucl. Instr. and Meth. A, 574, 1, 83-88 (2007).
- [101] P. Benetti et al. (A.M. Szelc), Astropart.Phys.28:495-507 (2008), arXiv:astro-ph/0701286v2.
- [102] The WArP Collaboration, "The WArP Experiment: progress report and current activities.", LNGS status report, Nov. 2008.
- [103] D. Acosta-Kane et al. (A. M. Szelc), Nucl. Instr. and Meth. A 587, 1, 46-51 (2008).
- [104] ENDF interactions database: http://www.nndc.bnl.gov/exfor/endf00.jsp
- [105] H. Wulandari, J. Jochum, W. Rau, F. von Feilitzsch Astropart. Phys. 22, 313-322 (2004), arXiv:hep-ex/0312050v2.

- [106] R. Acciarri et al. (A. M. Szelc) "Effects of Nitrogen contamination in liquid Argon", arXiv:0804.1217v1 [nucl-ex].
- [107] F. Carbonara, A. Cocco, G. Fiorillo, R. Santorelli, "Characterization of ETL D749-750-757 FLA photomultiplier tubes for the WArP experiment", WArP technical note, November 2005.
- [108] A.Ianni, P.Lombardi, G.Ranucci, O.Smirnov, Nucl.Instrum.Meth. A537, 683-697 (2005), arXiv:physics/0406138v1.
- [109] V. Gallo, poster presented at NDIP 08, proceedings to be published in NIM A.
- [110] L. Grandi, talk given at the WArP collaboration meeting, Nov. 2006.
- [111] R. Acciarri et al. (A.M. Szelc), "Oxygen contamination in liquid Argon: combined effects on ionization electron charge and scintillation light", arXiv:0804.1222v1 [nucl-ex].
- [112] G. Bakale et al., J. Phys. Chem. 80, 2556 (1976).
- [113] S. Himi et al., Nucl. Inst. and Meth. 203, 153 (1982).
- [114] E. Gatti, F. De Martini, Nuclear Electronics, vol. 2, 265-276 (1962).
- [115] H.O. Back et al. (Borexino Collaboration), Nucl.Instrum.Meth.A584, 98-113 (2008), arXiv:0705.0239v1 [physics.ins-det].
- [116] M. Moszyski et al. (DEMON Collaboration). Nucl. Instr. and Meth. A,317,262 (1992),
 - J. Bialkowski et al. Nucl.Instr.and Meth.A,275,322 (1989),
 - R.A. Winyard, J.E. Lutkin, G.W. McBeth. Nucl. Instr. and Meth., 95,141 (1971).
- [117] W. H. Lippincott et al., Phys.Rev.C78:035801 (2008), arXiv:0801.1531v4 [nucl-ex].
- [118] L. Pandola, private communication.
- [119] E. Aprile et al., Phys. Rev. D 72, 072006 (2005).
- [120] F. Arneodo et al., Nucl. Instr. Meth. A 449, 147 (2000).
- [121] R. Brunetti et al., New Astron. Rev. 49, 265 (2005).
- [122] M. G. Boulay, A. Hime and J. Lidgard, "Design Constraints for a WIMP Dark Matter and pp Solar Neutrino Liquid Neon Scintillation Detector", arXiv:nuclex/0410025v1.

- [123] D.-M. Mei et al., Astropart. Phys. 30:12-17 (2008), arxiv:0712.2470.
- [124] J. Lindhard, Mat. Fys. Medd. K. Dan. Vidensk. Selsk. 33, 1 (1963).
- [125] A. Mozumder, A. Chatterjee and J.L. Magee, Advances in Chemical Series 81, edited by R.F. Gould (American Chemical Society, Washington DC, 1968), p. 27.
- [126] J. B. Birks, Proc. Phys. Soc. A 64, 511 (1951).
- [127] L. Grandi, L. Pandola, A.M. Szelc, "Preliminary measurement of the neutron quenching in liquid argon", WArP technical memo, Jan. 2008.
- [128] L. Pandola, "Early results from the operation of a 2.3 liters Lar prototype in the Gran Sasso Laboratory", talk at Cryogenic Liquid Detectors for Future Particle Physics LNGS - March 13th-14th, 2006.
- [129] A.M. Szelc, talk at the Epiphany Conference 2006, Krakow, Poland, http://epiphany.ifj.edu.pl/epiphany.2006/pres/Andrzej_Szelc.pdf
- [130] http://wwwasd.web.cern.ch/wwwasd/paw/
- [131] J.Appel et al. (A.M. Szelc), "Warp 2.3: Summary of autumn 2006 WIMP data run", WArP technical note, 05.04.2007.
- [132] A. Cocco et al., "Light yield for nuclear recoils in the 3.2 kg WArP detector", WArP technical note, Jan. 2007.
- [133] L. Pandola, "Pulse shape analysis for the identification of double-interaction events", WArP technical note, Jul. 2006.
- [134] A.M. Szelc, "Preliminary Analysis of the Baffo Region", slides for the presenatation at the WArP collaboration meeting, LNGS 07.2006.
- [135] A.Cocco, F.Di Pompeo, L.Grandi, L.Pandola, A.M.Szelc, "Investigation on the baffo region of WArP 2.3 liter data", WArP technical note, 02.2008.
- [136] J.W.Keto et al., Phys.Rev.Lett., 33, 1365 (1974).
- [137] F. Di Pompeo, N. Ferrari, L. Grandi, C. Montanari L. Pandola, A. Szelc, "Analysis of the neutron calibration on the WArP 2.3 liters detector: preliminary results", WArP technical note, 01.2006.
- [138] K. Freese, J. Frieman, A. Gould, Phys. Rev. D37, 12, 3388 3405 (1988).

- [139] C. Rubbia, WArP Technical Note, 29.05.2006;
 - A. Ianni, "Seasonal Variations in the WArP detector's veto", WArP Technical Note, June 2006;
 - C. Rubbia, F. Pietropaolo, "Searching for a DAMA-like yearly modulation signal with the 8 ton LAr WARP", WArP technical note, 2.11.2008.
- [140] M. J. Lewis, K. Freese Phys.Rev. D70 (2004) 043501, arXiv:astro-ph/0307190v2.
- [141] Chris Savage, private communication.
- [142] B. Yanny et al., Astrophys. J. 588, 824 (2003), [Erratum-ibid. 605, 575 (2004)], arXiv:astro-ph/0301029,
 - H. J. Newberg et al., Astrophys. J. 596, L191 (2003), arXiv:astro-ph/0309162,
 - S. R. Majewski, M. F. Skrutskie, M. D. Weinberg and J. C. Ostheimer, Astrophys. J. 599, 1082 (2003), arXiv:astro-ph/0304198.
- [143] J. E. Gunn and J. R. I. Gott, Astrophys. J. 176, 1, (1972),
 - J. A. Fillmore and P. Goldreich, Astrophys. J. 281, 1 (1984).
- [144] R. Foot, Phys.Rev.D78:043529 (2008), arXiv:0804.4518v2 [hep-ph],
 R. Foot, Mod.Phys.Lett.A19:1841-1846 (2004), arXiv:astro-ph/0405362v1.
- [145] G. Ban et al. Phys. Rev. Lett. 99, 161603 (2007).
- [146] R. Foot, Phys.Rev.D69:036001 (2004), arXiv:hep-ph/0308254v3.
- [147] Z. Berezhiani, D. Comelli and F. L. Villante, Phys. Lett. B503, 362 (2001), arXiv:hep-ph/0008105,
 - A. Yu. Ignatiev and R. R. Volkas, Phys. Rev. D68, 023518 (2003), arXiv:hep-ph/0304260,
 - For pioneering work, see also S. I. Blinnikov and M. Yu. Khlopov, Sov. Astron. 27, 371 (1983).